Lehrstuhl für Theoretische Chemie
Fakultät für Chemie
Technical University of Munich

Capturing Ion Dynamics in Lithium intercalated Graphite

Bridging the Gap between Experiment and Theory through advanced Nuclear Magnetic Resonance and Multiscale Modeling

Cristina Grosu
Lehrstuhl für Theoretische Chemie
Fakultät für Chemie

Dissertation

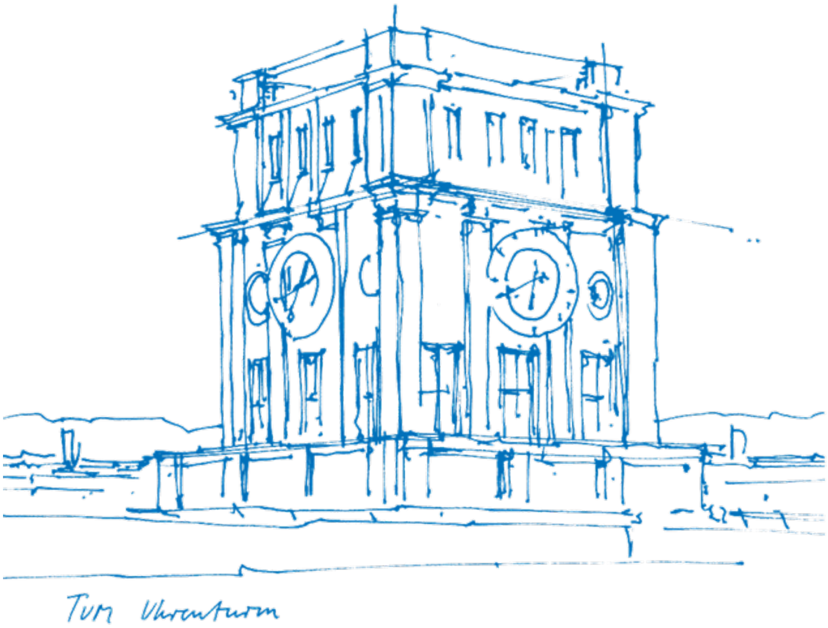

I hereby declare that this thesis is entirely the result of my own work except where otherwise indicated. I have only used the resources given in the list of references.

München, 04.03.2022 Cristina Grosu

Fakultät für Chemie

Capturing Ion Dynamics in Lithium intercalated Graphite

Bridging the Gap between Experiment and Theory through advanced Nuclear Magnetic Resonance and Multiscale Modeling

Cristina Grosu

Vollständiger Abdruck der von der Fakultät für Chemie der Technische Universität München zur Erlangung des akademischen Grades einer
Doktorin der Naturwissenschaften (Dr. rer. nat.)
genehmigten Dissertation.

Vorsitzende(r): Prof. Dr. Hubert A. Gasteiger
Prüfer der Dissertation:

1. Prof. Dr. Karsten Reuter
2. Prof. Dr. Steffen J. Glaser

Die Dissertation wurde am 08.03.2022 bei der Technische Universität München eingereicht und durch die Fakultät für Chemie am 23.03.2022 angenommen.

There is neither happiness nor misery in the world; there is only the comparison of one state with another, nothing more. He who has felt the deepest grief is best able to experience supreme happiness. – The Count of Montecristo – Alexandre Dumas

Preface

The focus of this thesis is on ion dynamics in lithium ion batteries, more specifically on graphite, the most used negative electrode material. This doctoral thesis is not a publication-based dissertation. However, the main work is going to be published in references 1 and 2 (B.5), and is adapted to fit the structure of this manuscript. Additional work that was necessary for the final work was published in reference 3(B.5). It will be described here just from a theoretical point of view overlapping with the results that provided necessary methods/tools for the multi-scale approach.
A parallel project, involving another commercial anode material $Li_4Ti_5O_{12}$ was conducted, however the work done in this case is not described here. All the work presented in this thesis was done between November 2017 and June 2021 in collaboration between the Chair of Theoretical Chemistry of the Technical University of Munich (TUM) and the Institute of Energy and Climate Research (IEK-9) with focus on Fundamental Electrochemistry at the Forschungszentrum Jülich (FZJ). Additionally, several stays as a visiting scientist at the Free University of Berlin have been conducted . Aim of these visits was to complement the work and to profit from the local expertise in the newly developed implementation of charged kinetic Monte Carlo within the `kmos` code.

Abstract

Lithium ion mobility remains one of the crucial parameters for predicting the performance and the life-time of a lithium-ion battery (LIB). In this regard, having a reliable diffusion coefficient associated with the respective lithium diffusion process is necessary and mandatory for understanding the correlation of this property with the failure or with the state of health (SOH) of a LIB over time. However, the scatter of ten orders of magnitude of those atomistic processes within the measured diffusion coefficients raises the question what the main reason behind this uncertainty is.

In this thesis, a reference system for the lithium ion mobility of lithium intercalated in Highly Pyrolityc Ordered Graphite (HOPG) is investigated from a theoretical and experimental point of view. The focus is on the upper boundary of the lithium intercalation such as LiC_6 which is the most studied phase and can be considered as the highest state of charge (SOC) of a LIB. Therefore, it can be considered as perfectly suitable to validate a new method and/or approach.

The right choice and combination of methods is not trivial. The time and length scales (easily) accessible by theory and experiments are typically different. To match those one need to perform more elaborate experiments as well as theory.

Nuclear magnetic resonance (NMR) is known to be able to give access to dynamical properties of the lithium ion, within the solid state diffusion framework. In order to theoretically simulate the ion dynamics at the same time and length scales as NMR a kinetic Monte Carlo (kMC) approach is mandatory in terms of computational cost. In classical kMC, the most displaced particle in a process is often treated as an isolated neutral atom. The electrochemistry of LiBs though motivates the decision to use an implementation of kMC, with an explicit charge treatment framework in combination with input parameters obtained from the first-principles.

A successful combination of the first principle charged kinetic Monte Carlo (1p-ckMC) with an advanced analysis through an inverse Laplace transform (ILT) of ^{7}Li Spin-Alignment-Echo-Nuclear magnetic resonance (SAE-NMR) to assess lithium ion mobility is then presented. The novelty of the approach lies within the combination of those techniques that allow to assess ion mobility independently and the possibility to further use the power of the simulation to predict mobilities and/or to unravel the mechanism behind it.

At the same time, while preparing the reference system using blind conditions (ambient pressure), the formation of superdense patterns was observed. Those were then further investigated through ageing and rationalized with *ab initio* thermodynamics (AITD) and molecular dynamics (MD). The presence of the superdense structures at those conditions reopens then the discussion on the actual highest SOC (LiC_6).

Zusamenfassung

Die Mobilität der Lithium-Ionen bleibt einer der entscheidenden Parameter für die Vorhersage der Leistung und der Lebensdauer einer Lithium-Ionen-Batterie (LIB). In diesem Zusammenhang ist ein zuverlässiger Wert für den Diffusionskoeffizienten erforderlich, der mit dem jeweiligen Prozess verbunden ist, um die Korrelation dieser Größe mit dem Ausfall oder dem Gesundheitszustand (SoH) einer LIB in Zusammenhang zu bringen. Jedoch wirft die beobachtete Streuung, von bis zu zehn Größenordnungen bei der Messung von Diffusionskoeffizienten, die Frage auf, was der Hauptgrund für diese Abweichungen ist. In dieser Arbeit wird Lithium, welches in hochgeordnetem pyrolisierten Graphit (HOPG) interkaliert, als Modellsystem für die Lithiumionenmobilität verwendet. Dieses Modellsystem wird dabei unter theoretischen und experimentellen Gesichtspunkten untersucht. Der Fokus liegt hierbei auf der oberen Grenze der Lithiuminterkalation (LiC_6), da dies die am meisten untersuchte Phase ist und deshalb herforragend geeignet ist zur Validierung einer neuen Methode oder eines neuen Ansatzes. Die richtige Wahl und Kombination der Methoden ist nicht trivial. Die Meso-Zeit- und Längenskala aus Experimenten ist grundsätzlich leicht zugänglich. Auf der anderen Seite sind aus theoretischer Sicht nicht alle Zeit- und Längenskalen direkt geeignet, um mit den Experimenten verglichen zu werden. Daher ist entweder die Zeitentwicklung genau, aber nicht auf der richtigen Längenskala oder umgekehrt. Es ist bekannt, dass die Kernspinresonanz (NMR) -Spektroskopie innerhalb des Festkörperdiffusionsrahmens Zugang zu den dynamischen Eigenschaften des Lithiumions ermöglicht. Theoretisch ist ein kinetischer Monte-Carlo-Ansatz (kMC) günstiger, um der gleichen Größenordnung für die Ionendynamik zu entsprechen. In derartigen Simulationen wird die Ladung oft als isoliertes neutrales Atom behandelt. Dies führte zu der Entscheidung, eine Implementierung von kMC mit explizierter Behandlung von Ladungen zu verwenden. Eine erfogreiche Kombination aus *ab-initio* Rechnungen, kinetischem Monte Carlo (1p-ckMC) mit expliziter Ladungsbeschreibung und von ^{7} Li Spin-Alignment-Echo Nukleare Magnetresonanz (SAE-NMR) dient in dieser Arbeit der Bewertung der Lithiumionenmobilität. Für die Auswertung des Spin-Alignment-Echo kommt eine fortschrittliche Analyse durch eine umgekehrte Laplace-Transformation (ILT) zum Einsatz. Die Neuheit des Ansatzes beruht auf der Kombination von Simulationen und Experimenten, die es ermöglichen, die Ionenmobilität unabhängig zu bewerten. Dies eröffnet die Möglichkeit, die experimentell validierten Simulationsmodelle zur Vorhersage der Ionendynamik zu nutzen und tiefere Einblicke in mechanistische Zusammenhänge zu erhalten. Gleichzeitig wurde bei der Vorbereitung des Referenzsystems unter Verwendung von Blindzustand (atmospherische Druck) die Bildung eines Superdense-Musters beobachtet. Diese wurden dann durch Alterung, *ab-initio* Thermodynamik (AITD) und Molekulardynamik (MD) weiter untersucht.Das Vorhandensein der Superdense-Strukturen unter diesen Bedingungen eröffnet dann die Diskussion über den tatsächlich höchsten erreichbaren Ladezustand (SOC), der bisher mit LiC_6 identifiziert wird.

Nomenclature

$\hbar$	Reduced Planck constant
AITD	ab initio thermodynamics
ckMC	charged kinetic Monte Carlo
D	diffusion coefficient
DFT	density functional theory
DFTB	density functional tight-biding theory
EFG	electric field gradient
EVs	Electricle Vehicles
FID	free induction decay
HOPG	Highly Oriented Pyrolytic Graphite
ILT	inverse Laplace transformation
kMC	kinetic Monte Carlo
kmos	a lattice kinetic Monte-Carlo framework
KS-DFT	Kohn-Sham DFT
LIBs	lithium ion batteries
MD	Molecular Dynamics
NEB	nudged elastic band
NMR	nuclear magnetic resonance
RF	radio-frequency
S/N	signal-to-noise-ratio
SAE	spin-alignment echo
SCF	self consistent field
SEI	solid electrolyte interface
SOC	state of charge
SOH	state of health
SS	solid state
TST	transition state theory
XC	exchange-correlation

List of Figures

1.1 Energy density as a function of the power density 2
1.2 Illustration of a lithium ion battery 3
1.3 Lithium intercalated in graphite LiC_6 4
1.4 Structure of a hexagonal graphite unit cell 6
1.5 Potential profile of the second dis-/charge cycle in a half-cell configuration 9
1.6 Representation of the ^{7}Li static NMR 12

2.1 Schematic representation of different length- and time-scales of a multiscale approach . . 15
2.2 Comparison of the band structure between DFT and DFTB 20
2.3 Repulsion potential landscape 22
2.4 Depiction of Gaussian process regression (GPR) in 1D input space 23
2.5 Example of a coarse-grained molecular dynamics (MD) trajectory 24
2.6 Methods for finding saddle points and transition states 25
2.7 Rate catalog example for the diffusional jump of a random vacancy in a solid matrix 28

3.1 Free spins and spins orientated in a magnetic field 33
3.2 Illustration of the simplest pulse-acquire experiment 35
3.3 The pulse sequence for the classical inversion recovery experiment 37
3.4 The pulse sequence for the spin alignment echo experiment 38
3.5 The pulse sequence of the SAE experiment 40

4.1 Schematic representation of the conducted synthesis 44
4.2 Single-layer representation of superdense LiC_{6-x} 45
4.3 Static ^{7}Li NMR and initial sample in the NMR tube 47
4.4 Evolution of the static ^{7}Li NMR spectrum during ageing of Li-intercalated HOPG 48
4.5 Representation of the sample 49
4.6 Static ^{7}Li NMR spectra taken after the decomposition process and pre- and post-heating . 50
4.7 Summary of the steps to produce the lithium–graphite intercalation compound 53
4.8 Photograph of the fully intercalated sample and the cut out fraction for the in-plane ^{7}Li NMR measurements 54
4.9 Representation of the ^{7}Li static NMR in function of different temperatures 55
4.10 Arrhenius plot of diffusion coefficients at 500, 750 and 1000 K 59
4.11 Selected snapshots in the MD trajectory at 750 K 60

5.1 Schematic representation of possible pathways of the triple-defect diffusion fro Ni in NiAl . 68
5.2 Arrhenius plots of Ni bulk self-diffusion in Ni_xAl_{1-x} single crystal 69
5.3 Arrhenius like plot of ion diffusion in the model system NiAl 69
5.4 Representation of the lithium atom on top of one graphene layer (A) 71
5.5 Representation of the lithium atom on top of one graphene layer (B) 72
5.6 Representation of the lithium atom on top of one graphene layer (C) 73
5.7 Representation of the ^{7}Li static NMR, obtained using the spin alignment echo (SAE) pulse (A) 74
5.8 Representation of the ^{7}Li static NMR, obtained under the spin alignment echo (SAE) pulse (B) 75

5.9 An Arrhenius like behaviour for the temperature dependent SAE-ILT 76
5.10 The diffusion coefficient of the LiC_6 as function of vacancy concentration 78
5.11 Arrhenius like behaviour for the diffusion coefficients for the lithium ion in LiC_6. The black line shows the data extracted from the ^{7}Li ILT-SAE NMR at different temperatures. The red one is the one extracted from cKMC at 0.1 % vacancy concentration. 79

B.1 Convergence test for the lithium diffusion coefficient within the graphite structure 86

List of Tables

4.1 Formation energies of selected LiC$_{6-x}$ intercalation compounds 51
4.2 Diffusion Coefficients from MD 58

5.1 Calculated diffusion coefficients for Li$_2$C$_{216}$ 72
5.2 Calculated diffusion coefficients for LiC$_6$ 73
5.3 Obtained diffusion coefficients from NMR experiment 75
5.4 Diffusion coefficients from cKMC and ILT-SAE 77

Contents

Preface i

Abstract iii

Zusamenfassung v

Nomenclature vii

1 Introduction and Overview 1
- 1.1 Current State of the Art of Li-ion Battery Technology 1
- 1.2 Graphitic and Carbonaceous Anodes 2
  - 1.2.1 Structure and Properties of Graphitic Anodes 4
  - 1.2.2 Lithium Storage in Graphite 6
  - 1.2.3 Ion Mobility within the Graphite Materials: Assessing the Diffusion Coefficient 10
- 1.3 Challenges and Limitations for a fast charge Electrode 10
- 1.4 Motivation 11

2 Theoretical Background of the Multi-Scale Approach 15
- 2.1 Density Functional Theory 16
  - 2.1.1 The Hohenberg-Kohn Theorems 16
  - 2.1.2 The Kohn-Sham System 16
  - 2.1.3 Approximation for the Exchange-Correlation Functional 17
- 2.2 Density Functional Tight Binding Theory 18
  - 2.2.1 General Concepts on DFTB 18
  - 2.2.2 The Electronic Part 19
  - 2.2.3 The Repulsion Potential 21
  - 2.2.4 Energy Barriers and Transition State Theory 23
- 2.3 Kinetic Monte Carlo 25
  - 2.3.1 kMC in a Nutshell 25
  - 2.3.2 Rate Constants in kMC 26
  - 2.3.3 kMC in `kmos` 27
- 2.4 Continuum 28
  - 2.4.1 Fickian Diffusion in a Solid Matrix from a Continuum Perspective 30

3 Theoretical and Experimental Background on the Nuclear Magnetic Resonance (NMR) 31
- 3.1 Nuclear Magnetic Resonance (NMR) 31
  - 3.1.1 Influence of local chemical environment 34
  - 3.1.2 Solid State NMR 35
- 3.2 Dynamics in NMR 36
  - 3.2.1 T_1 and T_2 37
  - 3.2.2 Spin Alignment Echo 39
- 3.3 Inverse Laplace Transformation 41

4 Revisiting the Storage Capacity Limit of Graphite Battery Anodes: Spontaneous Lithium Overintercalation at Ambient Pressure 43
4.1 Introduction . . . 43
4.1.1 What do we know about superdense LiC_2 and LiC_{6-x}? . . . 44
4.2 Materials and Methods . . . 45
4.2.1 Experimental . . . 45
4.2.2 Computational . . . 46
4.3 Results and Discussion . . . 46
4.3.1 Static ^{7}Li Nuclear Magnetic Resonance on Lithium intercalated HOPG . . . 46
4.3.2 Calendar Ageing and Post-ageing Temperature dependent static ^{7}Li NMR of lithium intercalated HOPG . . . 48
4.3.3 Ab initio Thermodynamics and Dynamics of superdense GICs . . . 50
4.3.4 Discussion . . . 51
4.4 Details on the Experimental Section . . . 53
4.4.1 Sample Preparation . . . 53
4.4.2 ^{7}Li Nuclear Magnetic Resonance . . . 53
4.5 Ab initio Thermodynamics . . . 56
4.5.1 General Concept . . . 56
4.5.2 Lithium chemical potential . . . 57
4.5.3 Free Energies of Graphite and Li_xC_y . . . 57
4.6 Ab initio Molecular Dynamics . . . 58
4.6.1 Diffusion Coefficients and Effective Diffusion Barrier . . . 58
4.6.2 Degradation of Clusters from MD Snapshots . . . 59

5 Investigating Diffusion of Lithium intercalated in Graphite by a Combination of charged kinetic Monte Carlo and Spin-alignment Echo Nuclear Magnetic Resonance 61
5.1 Introduction . . . 61
5.1.1 Standard kinetic Monte Carlo . . . 62
5.2 Charged kinetic Monte Carlo (ckMC) . . . 63
5.2.1 Extension for Coulomb Interactions . . . 64
5.2.2 Ewald summation . . . 65
5.3 The ckMC Algorithm and a Practical Guideline for Initializing the Simulation . . . 66
5.3.1 Simple Cubic: Intrinsic NiAl Test Case . . . 67
5.4 More on Diffusivity and Ionic Conductivity of Lithium . . . 70
5.5 Mapping the Hexagonal Graphite onto a Cubic Lattice . . . 71
5.5.1 Modelling Ion Diffusion and Mapping of LiC_6 . . . 72
5.6 ILT-SAE on Lithium intercalated HOPG . . . 74
5.7 Comparison of ILT-SAE and cKMC . . . 77

6 Summary, Conclusions and Outlook 81

A Appendix I 83
A.1 Density Functional Theory . . . 83
A.2 Hartree-Fock . . . 84

B Appendix II 85
B.1 NiAl: Test and Input Parameters . . . 85
B.2 LiC_6: Input Parameters and Analysis . . . 86
B.3 Equations related to the ckMC implementation . . . 87
B.4 Poisson Boltzmann Linearized . . . 88

B.5 Equations related to the ionic conductivity and mobility 89

Bibliography **91**

List of publications **109**

Acknowledgments / Danksagung **111**

1 Introduction and Overview

This thesis is structured in four main parts. First a general introduction on the battery basics and the actual state of the art of the lithium ion battery research is given in chapter 1. The theoretical background for the multi-scale approach, with the focus on the meso-scale level used to bridge to the experimental part in this work and the experimental foundations, as well as the theory for the Nuclear Magnetic Resonance (NMR), are presented as separate chapters 2 and 3, forming the second part of the thesis. The choice and the preparation of the reference system form the third part and are described in chapter 4, with the resulting concept of overintercalation and its role in Lithium Ion Batteries (LIBs). The fourth part brings the focus back on the ion dynamics in lithium intercalated graphite, and describes the results of bridging the gap between experiments and theory at the correct time and length-scale in chapter 5 through the investigation of the diffusion coefficient of lithium ions. A summary and an outlook are given then at the end in chapter 6.

1.1 Current State of the Art of Li-ion Battery Technology

Lithium ion batteries, as described briefly below, can be regarded as one of the key components in order to move towards a fully sustainable society. To pursuit the reduction of the CO_2 emissions, the world requires a complete reevaluation of the transportation sector, such as the replacement of fossil fuel powered vehicles with electric vehicles (EVs). [1] Therefore, a mass-distribution of EVs is mandatory to guarantee the success of a gasoline-free mobility. Among other energy storage technologies, lithium ion batteries (LIBs) are one of the systems with the highest energy densities, and equally high or even higher power densities. An excellent method in order to compare various energy storage devices is the so called Ragone plot, which is shown in Figure 1.1. It illustrates the different performances by comparing the specific energy density with the power density of certain materials or battery devices. Depending on the requirement profile of a specific task, the plot can guide the selection of the electrochemical device depending on the usage EV (high power) or balance (low power). [2] For example for electric trains, usually one would choose ordinary capacities because a high power density is required to allow bridging the short time in which a train might not be connected to the power grid. However, in order to promote a worldwide usage of batteries in every day vehicles like cars, a high power density and a high energy density are required at the same time. [3–7]
LIBs are electrochemical devices that convert chemical energy into electrical energy. The working principle of a LIB will be briefly discussed, before focusing on the component which investigated in this thesis. Due to their capability to store energy, supplied by an external source, they are used as portable electric power devices. Historically, the term "battery" was used to refer to a group of "cells", however nowadays they are used interchangeably, as will be the case also in this work. The term "batteries" will be however preferred here. [9] The working principle of a LIB is based on the lithium ion transport as cationic charge carrier between a negative and a positive electrode, plus the electrolyte in between that helps the transfer of the Li-ions between the electrodes. Other components such as separators and current collectors are present, however those are not within the interest of this work, as well as the cathode and electrolyte that will be just briefly mentioned. To quickly recall the basics: the active material for the cathode (or for convention the positive electrode) should undergo a reversible reaction with the Li-ions, which are de-intercalated during the charge and re-intercalated during the discharge. The lithiation (accompanied with a reduction) of the cathode is as well called discharge while the charge (accompanied with an oxidation) is referred as delithiation, while at the anode the opposite happens. The chemical reaction that summarizes that

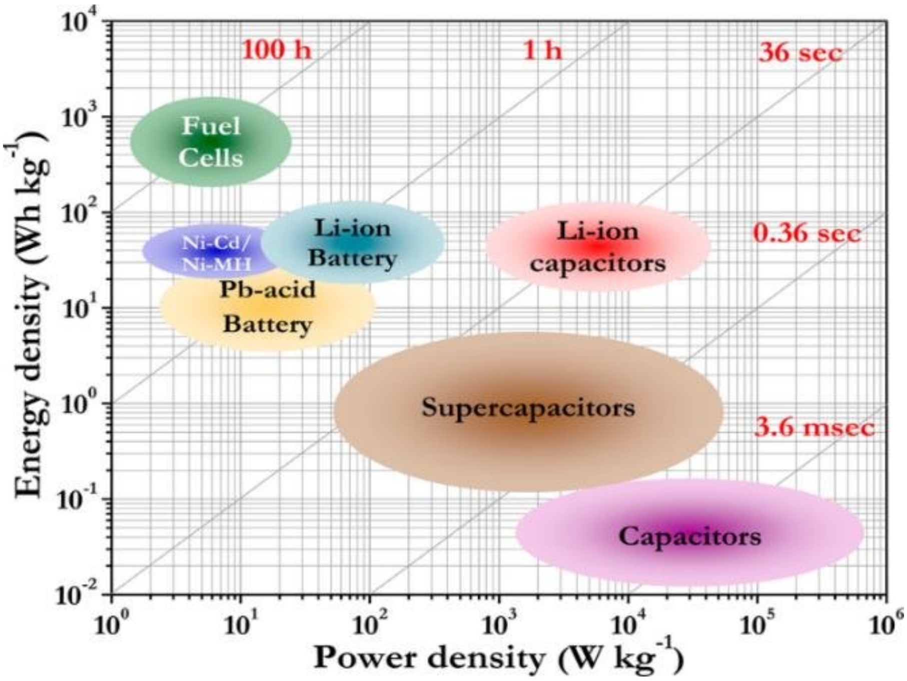

Figure 1.1 Depiction of the energy density as a function of the power density: The so called Ragone Plot from. [8] This type of plot is typically used to characterize different types of energy storage devices. Copyright © 2014 American Chemical Society.

process is shown in Equation 1.1 and a schematic illustration of the operation of a battery while charging and discharging is shown in Figure 1.2

$$xLi^{+} + AM + xe^{-} \underset{charge}{\overset{discharge}{\leftrightarrows}} LixAM \tag{1.1}$$

where AM stands for active material. Equation 1.1 it shows the possibility of unlimited cycles, ideally, if the reaction is fully reversible; however this is not the real case. Hence, the search for a better performance and ideal system to strike closest to a utopian infinite battery is still ongoing. The performance of the cell depends in fact on the nature of all the components: the properties of the electrodes with a prudent selection of the active material, the electrolyte composition and the geometry of the cell assembly. [10] Commercial state of the art of LIBs use $LiTMO_2$ based materials as cathode, where the TM stands for transition metals, with the most common one being a mixture of nickel, cobalt and manganese, in different ratios. As anode material, graphite is by far the most used and as liquid electrolyte a combination of ethyl-carbonate (EC) and dimetyl-carbonate (DMC). Figure 1.2 shows a sketch of a LIB, with a $LiCoO_2$ as cathode, LP50 that corresponds to the EC/DMC mixture and graphite as the anode, here shown in the LiC_6 form. [10–12]

1.2 Graphitic and Carbonaceous Anodes

Graphitic anodes belong to the class of carbonaceous materials, which exhibit a particularly rich structural variety. Carbons investigated for their lithium insertion properties include graphites, cokes, mesophase pitches, carbon fibers and whiskers, glassy and vitreous reticulated carbons, pyrolytic carbons, buckminsterfullerenes, carbon nanotubes, single graphene sheets, disordered carbons, hard carbons, etc.. [12–17] All of these possess appealing features for reversible lithium intercalation and the variety within the struc-

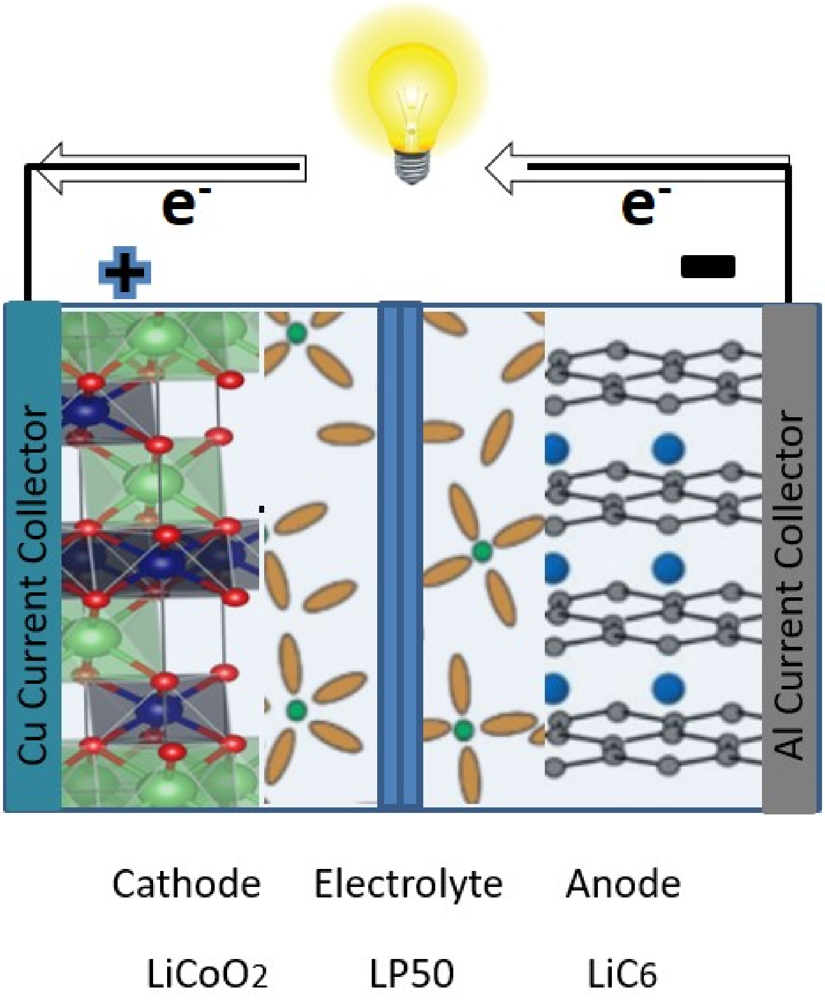

Figure 1.2 Illustration of a lithium ion battery. As cathode material serves $LiCoO_2$, LP50 is the electrolyte which is a ethyl-carbonate/dimetyl-carbonate (EC/DMC) mixture and the graphite is used as an anode material. Specifically, we show the anode intercalated with lithium (LiC_6).

tures offers different functionality. The facile kinetics and the reversible capacity can be raised by improving ideally their degree of crystallinity. [13] On the other hand, the disordered carbons (or carbon with no long-range crystalline ordering) show appealing features for a higher uptake of lithium and excellent cyclability. [13] Despite continuous screening of materials to find a better carbon based anode, graphite is still the most widely used one due to the its excellent synergy of the high-capacity and cyclability over the lifetime of LIBs. [16, 18]

Graphite electrodes are insertion based anode materials that allow lithium ions to be intercalated reversibly within the host material. Graphite is excellent in delivering a high reversible theoretical capacity with 372 mAh/g for the nominal LiC_6 stoichiometry shown in Figure 1.3, commonly identified as 100 % state of charge (SOC) . [14, 15, 19] The ability of the graphitic materials to store lithium is however influenced as well by the processes involved in the pre-preparation and post-preparation of the electrode. This can hinder the interpretation on the atomistic behaviour within the actual raw material. Even though graphite shows very good electrochemical properties, the variation in performance is still not fully understood and it is hard to relate to one aspect or another of the specific material. [14, 15]
Different production processes translate to a wide range of graphite morphologies with the respective changes in performance. [14, 15] Thus, the quality and the quantity of the sites that allow reversible lithium

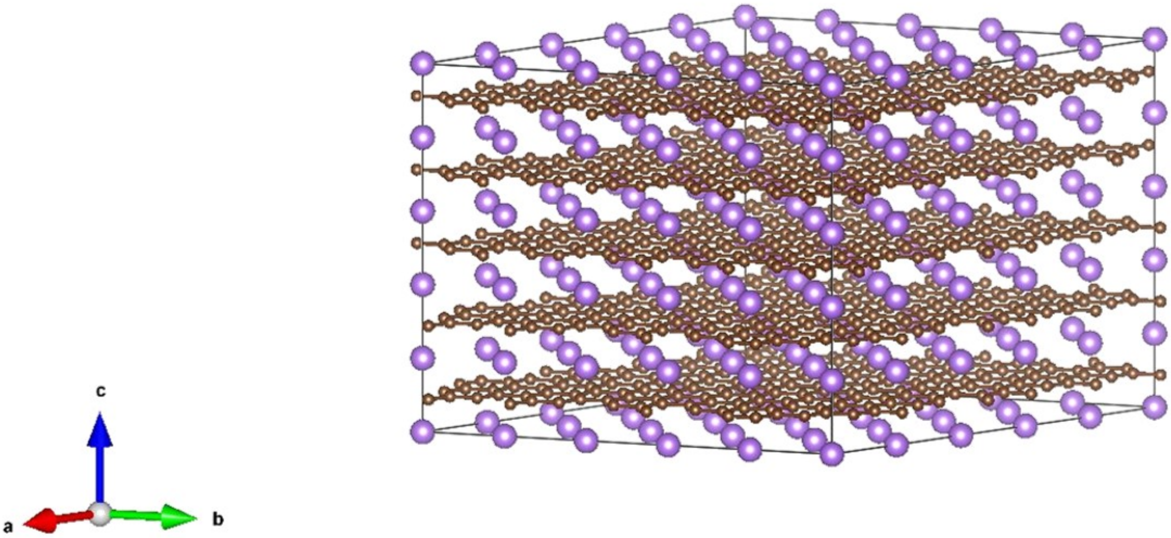

Figure 1.3 Representation of lithium intercalated in graphite LiC_6. The structures shows AA layer stacking and $\alpha\alpha$ ordering of the lithium ions. Lithium ions are depicted in lilac, and the carbon layers within the graphene sheet are colored in brown. The supercell of the structure is indicated by the black lines.

intercalation will determine the current/voltage characteristics of the electrochemical intercalation reaction and also potential side reactions. [20] The suitability of a carbonaceous material as lithium intercalation host depends then strongly on the method of preparation and on its pre-evaluation as material to judge the actual and future performance. [15]

Further building on that and disentangling the elementary influences becomes mandatory for the interpretation within the next steps of production, where particle size and morphologies play a role. This requires a reference system to shed light on the full mechanisms and to include all the considerations while investigating via *in situ* and/or *in operando* techniques to look over a better performance. Within this family of carbonaceous materials the graphitic one is the one currently used in commercial LIBs [14, 15], and is still *the* anode at this level. In this thesis, the focus of our studies is on unravelling pressing questions, especially related to the large uncertainty on diffusion coefficients of the lithium ion within the lithium intercalated graphite (LIGs) while approaching LiC_6, known as the highest state of charge. In the course of this endeavour, we additionally found ourselves questioning if this is truly the highest accessible SOC. A generic graphite structure is shown in Figure 1.4.

1.2.1 Structure and Properties of Graphitic Anodes

Graphite can be classified as natural or synthetic, based on the manufacturing process. Natural single crystals can be found in coal or lead mines, whereas synthetic crystals can be produced with various degrees of perfection available using a range of available methods. [18]

Graphitic layers are composed of sp^2- hybridized carbon atoms, which are arranged in a planar "honeycomb-like" network, like a graphene sheet. Several graphene layers leading to the layered graphitic structure are kept together by van der Waals forces that provide a weak cohesion between the layers. Strictly speaking from a crystallographic point of view, the term graphite should be used for the carbons having just a layered lattice structure with a perfect stacking order of graphene layers, either the AB (hexagonal graphite, 2H-, or α-phase) or the less common ABC (rhombohedral graphite, 3R- or β-phase). However, since perfectly stacked carbons are not achievable, the term "graphite" is used regardless of the stacking order, as will be done in the following here. In fact, the normal graphite stacking consists of hexagonal planes of carbon stacked along the c-axis in a staggered array usually $ABAB...$, where the lateral shift is going from layer A to layer B and is $\Delta AB = (1/3)\mathbf{a}_1 + (2/3)\mathbf{a}_2$, with $|\mathbf{a}_1| = |\mathbf{a}_2| = a_G$.

The primitive cell was identified at first by Bernal *et al.* [21] using X-ray diffraction. They also conclude that the artificial and natural graphite in the so-called raw or pristine material, are identical in structure despite different preparation processes. According to them, the unit cell consists of four atoms, with the respective height 0, $t/2$, $1/2$, $1/2 + t/2$ above the basal plane of the cell, with the fractions referred to the height of the full cell. However, if we consider half of the cell, the atoms must lie in two different planes, the basal one and the one in the middle. In fact, the carbon atoms in graphite lie in planes in which they form the so called nets of hexagons. These nets are then superposed in successive planes, so that half the atoms in one net lie normally above each other. The symmetry of graphite is then identified as hexagonal holohedral, with the space group D^3_{6h}. [21,22] The carbon atoms are linked in a two-dimensional net that will bring the graphite to exhibit in plane cleavage on the sheets.

Simply, the 3D structure of it can be seen then as multiple 2D graphene layers stacked together. The large gap between the carbon atoms between planes can be explained by the virtual extension of the carbon atom along one axis, thus destroying the tetrahedral symmetry that carbons would indeed have in a three-dimensional lattice, *i.e.*, diamond like structure. The stacking of the atoms was discussed for the first time in the early 30s and the final structure is known as AB or Bernal structure. [21]. This is the building block for investigating intercalation compounds. [21,23] Nevertheless, different stackings such as $ABCA...$ or $ABAC...$ are also possible, with the main requirement that a layer has to be followed by another one shifted by ΔAB. In fact, if we think that the planes of carbon atoms are stacked in such a way that half of the carbon atoms (A atoms) are located directly above each other in adjacent planes, while the other half (B atoms) are located above the center of the hexagon in the adjacent plane, this can easily cause a sliding process in the structure. Moreover, due to the small energy for the transformation of ABA (hexagonal graphite, α) into $ABCA$ (rhombohedral graphite, β) and *vice versa*, perfectly stacked and defect-free graphite is not easily available. The ratio between coexisting different stackings can also vary depending, again, on the pre-processing. Mechanical treatments, such as milling or shearing, can move the balance towards the β-phase, while thermal annealing will produce the thermodynamically more stable α-phase. The commonly observed stackings in graphite are a mixture of these discrete stacking alternatives. [18,21,24]

The intercalation process we are going to focus on becomes even more dependent, then, on the actual host morphology. Speaking of the latter, within the powder graphite used for electrode preparation, the structure is less than perfect. The crystal structure, however, made by stacking graphene layers, is kept, until any intercalant is (de)-inserted. The latter process changes the stacking order and the spacing based on the degree of intercalation. Focusing on the lithium ions (de-)intercalation in a battery cell, the shuffling of the ions will have a major effect on the reversible properties of the host material and the electrode properties itself. [18] Among the different sources of synthetic graphite as an alternative to the natural one, the Highly Oriented Pyrolytic Graphite (HOPG) became the reference system to investigate fundamental and basic properties. [14,18] The best available HOPG is well oriented, however the possibility of creation of defects while growing the material, *e.g.* high density or twist defects, cannot be completely ruled out. [18]

The impact of those defects within the ideal stacking by itself will induce variations and intricacies within the processes that one needs to investigate. [14,18,21,24]

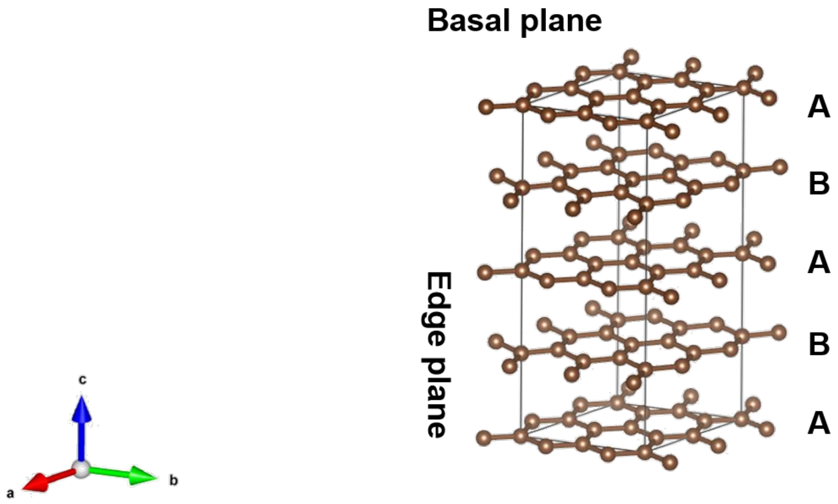

Figure 1.4 The structure of the hexagonal graphite unit cell with the $ABAB$ stacking – space group P63/mmc. Carbon atoms are depicted in brown.

1.2.2 Lithium Storage in Graphite

The layers of the lamellar structure of graphite offer a perfect accommodation for different intecalants, not only for alkali atoms such as lithium or potassium, but also for a variety of organic molecules. Despite happening in the same host material, the intercalation chemistry will strongly depend on the intercalant and on the insertion process. [16, 18]

A general feature of intercalation into graphite described in literature for alkali as the guest species is the formation of a periodic array of unoccupied layers (galleries) from high to low concentration of guest species, called stage formation. [16, 18] These are a periodic alternation of the host and guest layers, with n layers of the host separating neighboring guest layers in a stage n intercalation compound. The staging is commonly regarded as a quasi-one-dimensional ordering phenomenon and it is characteristic of a large number of graphite intercalation compounds (GICs).

The stages are indexed "s" which is equal to the number of graphene layers between two nearest guest layers. The staging phenomenon needs to take different contributions to the energetics of the formation of the structure into account. Staging is a thermodynamic phenomenon related with the energy that is required to formally open the van der Waals gap between two graphene layers, and allow the guest to enter the host.

The main contributions to this energetics will come from: I) the charge transfer between the guest and the host species, II) the elastic effects associated with the distortion of the host by the guest with the related issue of the cohesion between the layers, and III) the interaction between the guest atoms in the same layer, as well as with the adjacent host layers, if filled. In this thesis, the case of lithium as guest will be addressed. Despite the apparent simplicity of the involved elements, there is still room for debate regarding the complete details of the lithium ion intercalation mechanism. The staging is only one of the proposed models, and perhaps an overly simplified one. This simple model can be considered complementary with the so-called domain model as a function of the inserted amount of lithium. [14, 16, 18, 25]

The stage model of the lithium intercalated graphite was first proposed by Rüdorff and Hofmann in 1938. [12, 26–29] According to the staging nomenclature LiC_6 is stage I, with the conventional assumption that this is the maximum possible concentration of lithium to be inserted. The other binary phases with lower lithium content are then named as stage, IV, III, IIL and II. The splitting of the II into s=II (x =0.5 in $LixC_6$) and s=IIL (x =0.33 in LixC_6) is due to the different lithium packing densities. The IIL is also seen as a liquid stage, which ideally has no in-plane ordering. [10, 14, 16, 18] The stacking of the LiC_6 will change from $ABABA$ to $AAAAA$ upon intercalation, and will strongly depend on the total lithium inserted. The staging phenomena are more complicated though, if we think of the intermediate staging. The repulsive Coulombic interactions between the guests are less relevant then those of the guests with the graphene sheets, however not to be neglected. As a consequence of this combination of effects, highly occupied van der Waals gaps are energetically favored over a random distribution of guests. Those phenomena and the degree of intercalation can be easily observed during the electrochemical reduction of carbons in Li^+ containing electrolytes as medium to shuffle the ions.

The domain model on the other side was proposed for the first time by Daumas and Herold [25], while investigating the transition mechanism for staging. Within the domain model, the lithium ions will occupy the interlayer space between the two graphene planes (galleries) as islands. [25, 30, 31] The existence of islands or finite domains of intercalant presents the possibility of disorder in the staging sequence, in particular when the layers are of finite extent. The islands can be present adjacent to each other within the same gallery while maintaining the so called "stage" overall. Obviously, the debate whether the staging or the domain model is the more accurate one is not fully clarified and the combination of the two might be the right answer.

Neither of the two hypotheses alone suffices to explain the full transition mechanism from the empty graphite to the full intercalated one. Within the early studies, it was shown that the entropy gain of the rearrangement of finite size layers in intercalation compounds can lead to stage disorder without atomic vacancies. [30,32] Phase diagrams to describe phase transitions via staging normally show the stage (and in plane stoichiometry) as a function of intercalant, concentration, temperature, and/or pressure. To calculate these phase diagrams, the statistical thermodynamics of staging must be understood. The kinetics should not be neglected completely and focusing on one step after another may help to elucidate as much as possible. [32]. The relationship between the changes in the in-plane density and re-staging transitions induced by either changes in the pressure or temperature was described by Di Vincenzo *et al.* [33, 34] It was reported that the diluted stage-II of Li-intercalated graphite showed the same phase transformation at high T and finite P as at low T and P=0. Li GICs according to Safran *et al.* [32] in fact show a process driven by the local elastic distortions. Low-T mixture of stoichiometric LiC_6 and LiC_{12} transform upon heating through the Safran restaging boundary $T_s(x)$ to nonstoichiometric LixC_6, an ordered pure stage-I compound with the same in-plane $\sqrt{3} \times \sqrt{3}$ superlattice as its low-T precursors. The new phases therefore contain new sites through the otherwise long-range ordered Li layers. At higher T the long-range order disappears in a 3D melting process, the details of which vary with vacancy concentration. The Safran model neglects long-range order and thus does not account directly for the melting transition.

According to Fischer [32], the concentrated stage-I exhibits novel melting behaviour associated with the presence of Li vacancies in the low-T ordered phase. A random vacancy distribution would be expected to depress melting temperature T_m without changing the nature of the transition. An alternative scenario consists of in-plane phase separation into maximally dense islands surrounded by empty canals, in which case the transition will be smeared out since the lithium on the shorelines will melt first (analogous to current ideas on dislocation mediated melting in 2D systems). Increasing the vacancy concentration [V] (or decreasing x) decreases T_m, but smears the transition significantly. The first-order step found for x= 1.00 and 0.99 disappears for [V] > 2 $\%$ but the continuous melting fits a power law exponent up to [V] = 5 $\%$. The samples with x=0.99 and 1.00 have the same T_m but the precursor is steeper in the latter. The exponent was interpreted in terms of tri-critical behavior in the 3D–state Potts model: since the symmetry class is unaffected by vacancies, this interpretation should be investigated in more detail. [32] Before going into the description of the electrochemical storage, that is based on similar intercalation concepts as for the mechanical intercalated lithium in graphite mechanism, a few words on the nature of the bond present within the LIGs compounds are mandatory.

Hofmann *et al.* [27] proposed in the early 30s that the bond in GICs is of electrostatic nature. Based on that, the ionic model was developed, where the lithium is stored in cationic form in graphite, where the graphitic host is taking over the corresponding negative charge. This concept is largely used in the description of lithium ion batteries and is also supported by the electroconductivity increase for the GICs with respect to pure graphite. The ionic state of lithium in GICs was indeed confirmed by ^{7}Li NMR spectroscopy, as well as quantum mechanical calculations, however the debate and the criticism on this pure ionic model is still present and valid. In particular in LiC_6 the bond seems to be partially metallic (or covalent). Additionally, the AA stacking that is present, makes the Li-Li distance along the c-axis smaller then the in-plane Li-Li distance. On the other side, the increase of the volume due to the lithium intercalation is better explained with the ionic form of the lithium. For the LiC_6 a neutral character was also attributed to lithium atoms, however there is still a potential gap between the metallic lithium and the LiC_6, that indicates the lithium should be partly ionic. [16, 35] The window potential where the lithium is stored between the LiC_6 and the lithium metal, although pretty close to the metallic state, has to have an ionic character. In fact, the nature of the bonds and the regular in-plane order of guest atoms in LiC_6 can be better explained if the lithium exhibits some ionic charge, which is providing repulsive Coulombic interaction with the near lithium neighbors.

Electrochemical Lithium Storage

In the battery community, there is widespread consensus that a maximum lithium content of one Li guest atom per 6 carbon host atoms, as mentioned above, can be reached for lithium insertion into graphite powder, HOPG, or any graphitic carbon at ambient pressure, while performing an electrochemical intercalation. The potential profile of the natural graphite while the lithium is intercalated electrochemically has a stepwise shape, due to the formation of different stages and transitions according to Dahn *et al.* [36,37]. Based on electrochemical experiments, a phase diagram for the lithium intercalation compounds was derived as well, with following research that confirmed or raised new questions on the mechanism. Nevertheless, the mechanism proposed and still widely used is the staging mechanism with the coexistence of two binary phases, and following staging until the stage IV, passing through III, IIL, and II. The IIL is the subdivision of the II stage and the "liquid-like" one, due to the different packing of lithium, where the "liquid-like" does not have order in plane. The coexistence of the two stages during a first-order transition appears as a potential plateau in the charging curve, as shown in Figure 1.5. [15]

In the context of electrochemical Li storage, it has been widely investigated over the past decades whether the reduction of the number of constituent "graphene" layers of graphitic carbon to a few leads to any difference with respect to the storage mechanism and content of the inserted lithium, down to the single layer graphene (SLG) limit. However the results are still contradictory. In the case of graphenic carbon having very few layers, but well-ordered and nearly pristine, graphene layers, intercalation of Li does take place in the interlayer spaces and in the bulk graphite. In addition the surface(s) and also exposed "stepped" edges of each layer also contribute to a relatively greater extent toward the Li-storage. The role of the graphene edge sites on Li-storage indeed shows the possibility of accumulation of Li close to the edges of a single graphene layer and the “stepped edges” of a graphene nanoribbon (GNR) compromising more than one graphene layers (in addition to the Li "stored" on the surface of the topmost graphene layer). The Li atoms added on the edges shows a tendency to move inside the GNR. The Li storage contribution from the surface gives an increment of the storage capacity on top of the maximum lithium intercalation, with respect to the graphene sheets. [38, 39]

Lithium Storage in Non-Graphitic Carbons

Next to the graphitic carbons used for anode material, the non graphitic ones – those where the structure disorder takes over the crystalline part – were taken into account for their ability to store a larger amount of lithium.

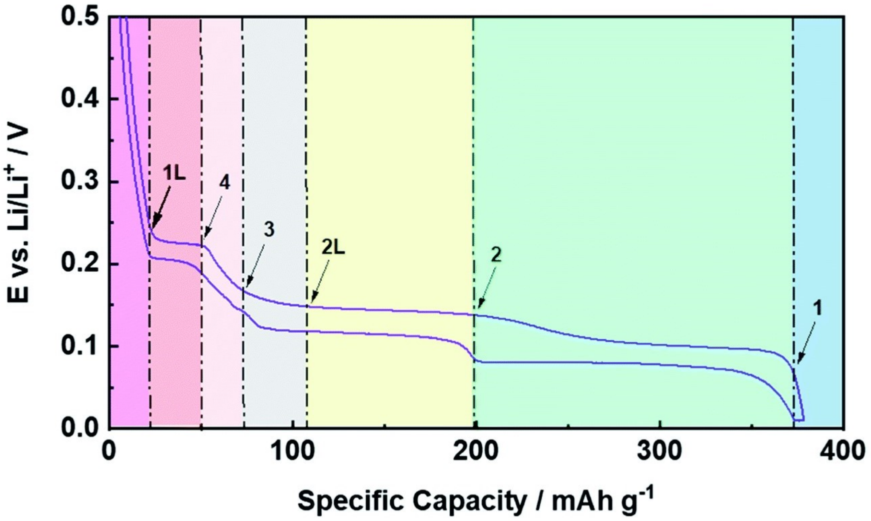

Figure 1.5 An example for the potential profile of the second dis-/charge cycle in a half-cell configuration with metallic lithium as counter electrode. [15]. The stages for the electrochemical de-/intercalation were adapted and redrawn from Assenbauer *et al.* [15].

In fact high lithium storage capacity, compared to the theoretical limit accepted for graphite, with a predominantly planar insertion, was identified within the hexagonal networks of carbons that lack extended crystallographic order. It is worth noticing, that apart from the increase in disorder pyrolytic carbons have also been known to retain up to 30 at.% of residual hydrogen. [40–42] The high lithium storage content can be related to disorder [43, 44] and also to the hydrogen content [40, 45, 46]. The absence of long-range order frustrates attempts at understanding the relationship between the structure and the reversible lithium insertion properties of disordered carbons. Indeed, despite their large insertion capacities, the applicability of these carbons in practical cells is hampered by large irreversible capacities, and polarization between charge and discharge (hysteresis). Usually the irreversible capacity loss is associated to those effects. Some extra mass to compensate for the capacity loss compared with the cathode materials can be accommodated. However, since the hysteresis is associated with the lowering of the Coulombic efficiency and a poor cycling performance, the practical energy efficiency overall is compromised. [13, 16]
Another problem with disordered carbons is the variety of them and the association with multiple mechanisms for the storage. The relevance of mentioning those will be clear in the interpretation of the actual mechanical intercalation of the lithium in a reference system used in this thesis.

A brief overview other the concept of the so-called “superdense” phases that are then associated with a higher lithium storage capacity will be reported here. Despite the fact that these are known, they were never reported under normal conditions for lithium intercalation within bulk graphitic carbon, but only within bilayer graphene or non-graphitic carbons. [47,48] Lithium storage higher than LiC_6 was shown to proceed with different carbons such as polyacenic semiconductors up to LiC_2 and Ishikawa *et al.* showed that Li_2 could indeed exist. Additionally it was shown that lithium atoms could occupy both edge and interstitial sites up to LiC_3 composition. [46] All these arguments on the "superdense" structures strenghten the actual convention that the lithium storage capacity of graphite is limited by the lithium accommodation of one "ion" site for every six sp^2 hexagonal carbons (LiC_6), as mentioned above.
Lithium intake up to 4765 mAh/g for porogen treated pyrolithyc carbons was reported. However the high irreversible capacities and continued loss in capacity with cycling hamper their exploitation in high-energy lithium ion-batteries. [49] Sato *et al.* used the Li_2 covalent molecule capacities to explain the high capacity up to 1116 mAh/g [41]. Another option to explain the high capacity would be the usage of the

defects present within the graphene sheets or the existence of nanovoids, created while milling or during the process of the matrix preparation. However, even the Li storage mechanism (or the storage locations) in graphene is still up for debate both experimentally and theoretically. [17, 50–53] It has been proposed that Li atoms cannot adsorb on monolayer graphene, but it only intercalates between at least two layers. To understand and resolve this problem is rather essential for the incorporation of graphene materials in LIBs. [17] In fact, as mentioned before, to gain deep insights into the Li-intercalation behavior, bilayer graphene was used as a model to break down extended graphite into a simple system. [47, 54] Even without the long distance z-axis diffusion of Li^+ ions in graphite and the possible influence from the neighboring layers, bilayer graphene still exhibits the same Li-storage processes as graphite, indicating that the Daumas-Herold domain model should be more suitable for describing the z-axis Li-storage behavior in graphite. Moreover, the planar distribution of these staged Li atoms may indicate that any incoming Li^+ ions can enter the centroid of three adjacent Li atoms in the former phase without disturbing their initial locations too much. [25, 55] Additionally, for the graphite-based LIBs, it is as well known that the insertion/deinsertion potential of Li^+ ions is always below 0.3 V (vs Li^+/Li), a range that contributes to the overwhelming capacity of graphite. [54] Clearly, there are more intrinsic and quasi-reversible processes than the ones expected within this range of the potential. This further raised even more questions, on the irreversible capacity that is hard to retrieve back from those structures.

1.2.3 Ion Mobility within the Graphite Materials: Assessing the Diffusion Coefficient

An atom moving through a solid can be seen as performing jumps between minima in a potential landscape of the crystalline matrix. This sounds relatively easy, however before reaching and investigating the jump or the movement of those, we have to bring one system into the other.

The transfer of matter is a complex phenomenon, in particular for the lithium intercalation into graphite. Herold [56] suggested within the early stages of the investigation the concept of "isostage" and "polystage" reactions with two main mechanisms that need to be looked into – diffusion and sliding – when intercalating a compound within the graphite matrix. The isostage reactions are those where the so called stages remain unchanged and the polystage ones, as the word says, will lead to an increase or a decrease in stage within the system. A combination of both, obviously, can not be excluded. Diffusion, which depends on a gradient in concentration, is a slow phenomenon which governs the kinetics of isostage exchange reactions. Sliding, which depends on the free enthalpy of the reaction, and on the intercalate cohesion, can be very fast and often plays the main role in polystage transformations. Hence, changes in stage during intercalation or de-intercalation correspond to an association of a slow interfacial process and a faster reorganisation of the intercalate by sliding. Intercalation consists of an "invasion" of the graphite interspaces by external ions within the layers, implying a movement of pleats (dislocation loops) in the graphene sheets. This is then a matter transfer process, which is closer to a hydrodynamical than to a diffusion one, and can be called a "sliding" process. [56]

A clear distinction, however, between a sliding or diffusion process with the lithium that intercalates in graphite can not be made. This might be one of the reasons that the definition and the measurement of the diffusion coefficient are hard to disentangle and to agree upon. Moreover, sliding and diffusion are not the only mechanisms that can occur, while shuffling lithium atoms in a full working LIB cell.

1.3 Challenges and Limitations for a fast charge Electrode

As mentioned in Section 1.1, the performance of a LIB is determined by each single component and by the design of the cell. Hence, the challenges to improve the performance of a battery are closely linked to the performance of cathode, anode and the used electrolyte. [15, 17] However, as the main focus of this work lies on graphite as anode material, the following section will focus on the limitations of this specific material.

To have a performant anode material, a high efficiency is required and no drastic change in the surface is preferred in order to not promote the electrolyte decomposition reaction. Additionally, the used material should also provide high safety. To ensure a high-energy density the electrode needs to operate close to the potential of the metallic lithium and to not forget, it should be lightweight and cheap. [17]

Despite considerable effort in order to find alternatives to graphite, the latter still remains the most widely used in commercial applications. Alternatives like lithium silicon alloys, antimony and lithium titanate $Li_4Ti_50_{12}$ still fall behind the performance of a standard graphite anode. [11, 14, 15] Nevertheless, graphite anodes are affected by a rather high capacity loss during the first few charge cycles. This occurs due to the formation of a so called solid electrolyte interface (SEI), also known as ageing process of the electrode. Despite being the cause of capacity loss, it serves as a protective layer on the graphite anode which prevents the continuous reduction of the electrolyte on the electrode side. [17, 57]

Despite this loss in the first cycles, graphite continued to be used without many problems in commercial applications. In fact, until a few years ago, the limiting factor for the loss in the capacity and energy density of the LIB was still the cathode materials. [58, 59] However, with the development and the usage of high-energy cathode materials in EVs, the drawbacks of the graphite anode were brought back into attention, such as the limiting factors within the cycle life time and the failure of describing consistently the lithium ion mobility within the material itself. In fact, despite decades of investigation of the mechanism of lithium intercalation, the ion mobility and the underlying microscopic processes are still not fully understood and there is still a huge variation of several orders of magnitude in the exact determination of lithium diffusion coefficients in the literature `i.e` $10^{-12.5} - 10^{-6.5} cm^2 s^{-1}$. [15, 44, 60–92]

These discrepancies clearly demonstrate that there is still a lack of fundamental understanding of the details behind the relevant diffusion processes. This becomes even more critical as lithium ion mobility is nowadays used to predict the performance and life time of a battery cell. [14, 15, 17, 20]

1.4 Motivation

This thesis is designed as part of a multi-disciplinary approach. Tackling all relevant characteristics of a full working battery requires transversal thinking. The final product relies on the design and the engineering which will define the final performance of the battery cell. [3, 93] Since LIBS are used in all electronic devices the optimization of the performance and the prediction of the performance reliability are a must. In that context, the cell design is pretty well established, whereas the chemical materials are pushed towards the extreme edge limits of their capabilities in order to achieve the highest performances. This is often done without a full atomistic understanding of the underlying processes within all of the components. A critical issue such as the overall performance of a battery still relies on the intrinsic properties of the materials, for example its theoretical capacity. [3] Therefore, the key to understand the limiting factors of certain materials lies within the knowledge of the fundamental mechanisms that are behind the working cell. There are different ways to gain insight into which process is hindering the performance, shortening the life-time of a battery, as well as giving *a priori* a prediction of it. Most of them are experiments to measure directly the ion mobility, however there are also observables that are not yet accessible with experiments or that cannot unambiguously be measured, such as diffusivities.

On the other hand, theory is another way to investigate and identify the properties that are not experimentally accessible. Within this context, the idea was then to combine and have a synergistic exchange between experiment and theory. As mentioned before, one of the properties that was not yet assigned unquestionably is the lithium ion mobility. Lithium atoms that are shuffled through the anode, cathode, electrolyte and through the interface, can undergo different transport mechanisms within the same working cell. Lithium mobility is therefore fundamental for understanding the limiting factors and sources of failure of LIB in general. [3] Once all the components and materials are combined within the working cell, it is hard to identify the responsible component for the following failure. It has been proposed that there is a substantial lack of theoretical knowledge within the meso-scale regime, which is indeed the one un-

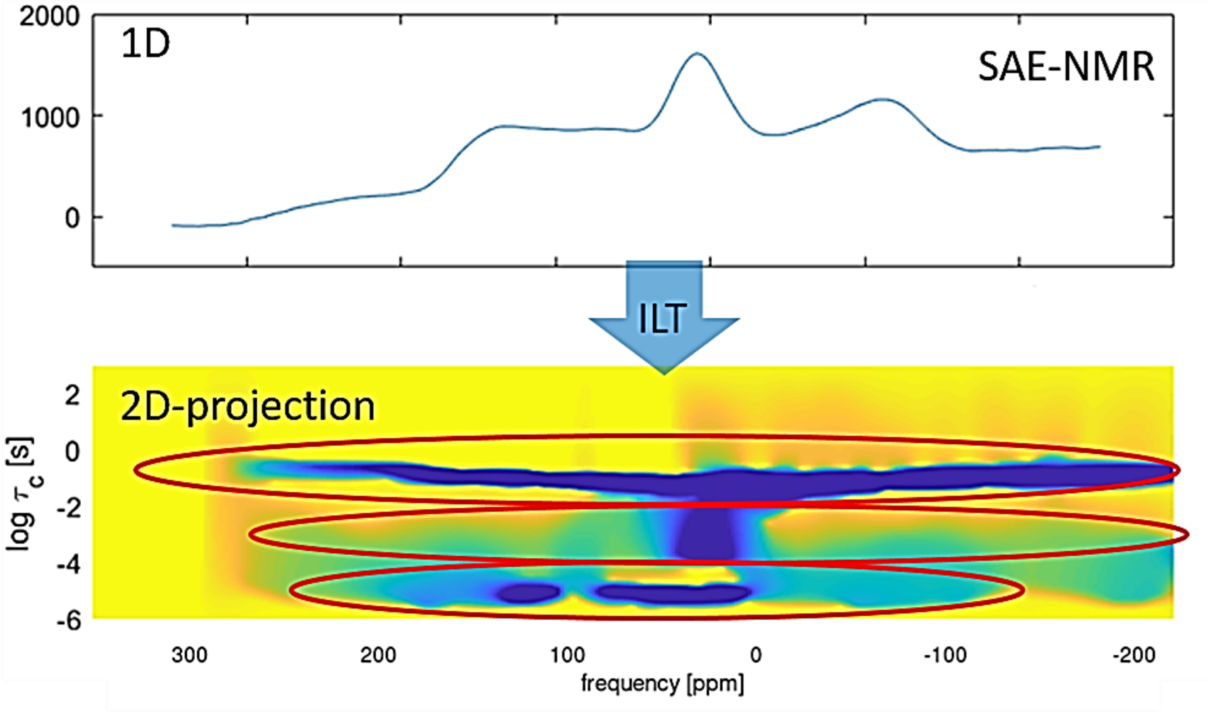

Figure 1.6 Upper panel: the representation of the ^{7}Li static NMR, obtained under a spin alignment echo (SAE) pulse. Lower panel: The inversion of ^{7}Li SAE spectra recorded at room temperature for the mechanical intercalated LiC_6 within graphite powder. Different regions are showing various mobility, however the spectra is to complex to correlate directly the processes with the mobility.

derrepresented. [94] The uncertainties described above are particularly apparent with graphite anodes. Literature values regarding the lithium ion mobility show quite a scatter over a large range, *i.e.*, ten orders of magnitude if looking at the lithium diffusion within the graphite material. [15, 60–67]
A question that arises naturally is the reliability of diffusion coefficients, however it is not trivial to assess them unambiguously, considering the complexity of the preparation of the materials, the underlying structure and the design of the cell. We identify experimentally within the Nuclear Magnetic Resonance (NMR) the Spin Alignment Echo (SAE) as a good non-destructive technique that allows to investigate mobility in the meso-scale regime directly on the raw material, which can be extended to *in operando* cells. From the theoretical point of view, kinetic Monte Carlo (kMC) is then the method of choice within the multi-scale framework to access the scale of interest. The challenge is to build a reference system that allows to assess a reliable observable, to be studied both by theory and experiment and at all the necessary time and length scales.

As a good candidate for a reference system we identified at first the *post-mortem* electrochemically intercalated LiC_6, however the influence of the electrolyte and the actual charging protocol or condition will still complicate the system. Thus, the mechanically intercalated lithium in graphite within the LiC_6 phase was then taken into account as well. However, the variation in preparation and grinding procedures once again makes the system a challenging reference as shown in the Figure 1.6 post data analysis. Finally the mechanically intercalated lithium in the highly oriented pyrolithyc graphite (HOPG) was chosen. This apparently simple system actually exhibits a surprisingly rich chemistry, pushing the challenge from a methodological point of view and unravels more aspects on the materials, which were previously overlooked. A more advanced data analysis namely the inverse Laplace transformation (ILT) on the SAE-NMR was used, replacing standard fitting of relaxation spectra. The choice on the technique allows us to asses a distribution of different relaxation times, thus offering more insight into the processes directly from the simple spectra. Furthermore, the diffusivities extracted from NMR can be directly compared with the results of kinetic Monte Carlo (kMC) simulations. For the latter, the in house `kmos` code was used, with a new feature for the charge treatment, taking a step forward from the standard approaches to model lithium intercalation in graphite, where the ions are treated as neutral particles.

This thesis discusses the short journey from well established techniques to newly developed methods to unleash the synergies of the combination of experiments and theory to lead us to new insight into Li GICs.

2 Theoretical Background of the Multi-Scale Approach

This chapter will describe in a nutshell all the theoretical levels below the kinetic Monte Carlo (kMC) and the reader will be introduced to an idea of how a multi-scale approach works. Figure 2.1 shows a schematic representation of the different length and timescale with the standard applied methods.

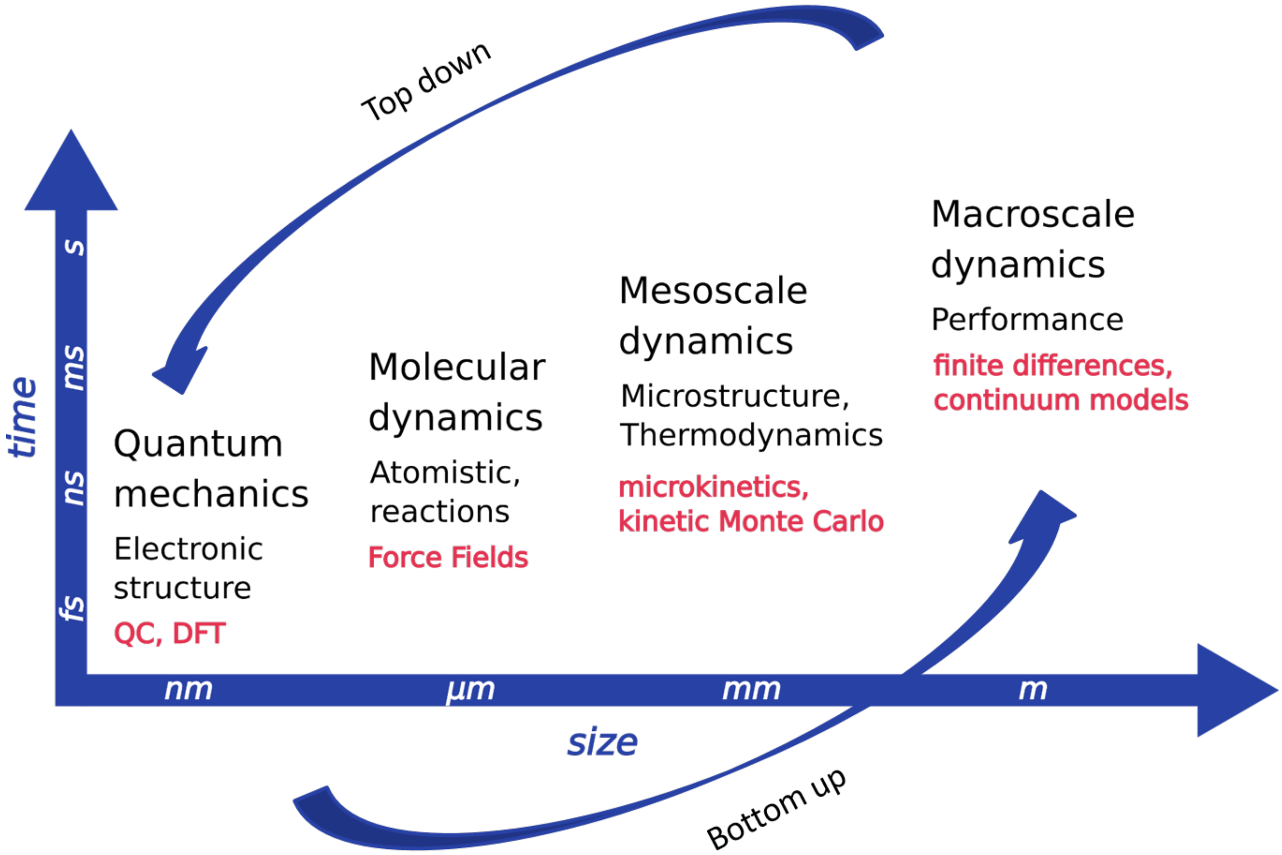
Top down
time
s
ms
ns
fs
Quantum mechanics
Electronic structure
QC, DFT
Molecular dynamics
Atomistic, reactions
Force Fields
Mesoscale dynamics
Microstructure, Thermodynamics
microkinetics, kinetic Monte Carlo
Macroscale dynamics
Performance
finite differences, continuum models
nm
µm
mm
m
size
Bottom up

Figure 2.1 Schematic representation of different length- and time-scales for different theoretical methods. This representation can also be seen as an overview of how a multi-scale modelling approach would look like. Beginning with the atomistic modelling approach on a quantum mechanical level more and more coarse grained methods are used. Typically, the more coarse grained models use input parameters obtained from the less coarse grained approaches.

In this thesis, the theoretical focus will be on the kMC and the meso-scale domain. However, having a brief description of the necessary formalism to approach a system from first principles might help to understand the full picture. Density Functional Theory (DFT), will be described shortly at first, followed by the semi-empirical approach of Density-functional Tight Binding (DFTB) theory. From DFTB the next level, passing through the Transition State Theory (TST), is represented by the kinetic Monte Carlo. The continuum part from the multi-scale approach is discussed just briefly to complete the picture; even though not used in this thesis, it is the next and last level to be taken into account. This is a description of a so called "bottom up" approach, building from the lower scale into the upper. The complementary one will be the "top down". While such approaches can be extremely powerful and efficient, they have a slightly different focus then the one in this work.

2.1 Density Functional Theory

This section aims to introduce the reader to the basic concepts of electronic structure theory. In particular the focus lies on density functional theory (DFT). For more details the reader is referred to "A Chemist's Guide to Density Functional Theory" by Koch and Holthausen. [95]

2.1.1 The Hohenberg-Kohn Theorems

Modern DFT is based on the first and second Hohenberg-Kohn theorem. The first theorem establishes a one to one mapping between the ground state electron density of a system and its Hamiltonian. It states that, the ground state density is in principle sufficient to obtain any property of interest of a system. [96] In other words, the full many-particle ground state is a unique functional of the ground state density. It is then the second Hohenberg-Kohn theorem which provides a practical tool set on how one can obtain the ground state density by introducing a variational formulation for the total energy,

$$E_0 \leq E[\rho] = T[\rho] + E_{Ne}[\rho] + E_{ee}[\rho] \quad . \tag{2.1}$$

Briefly, Equation 2.1 is the variational principle in the context of the HK theorem. This basic equation states that any given trial density $E[\rho]$ will always yield energies which are above the true ground state energy E_0 of the system unless the density is the ground state density itself. In other words, the true ground state energy can be obtained in an iterative fashion by minimizing the energy of the total energy density functional,

$$E_0 = \min_{\rho \rightarrow N} \left(F[\rho] + \int \rho(\vec{r}) V_{Ne} d\vec{r} \right) \quad . \tag{2.2}$$

In Equation 2.2, $F[\rho]$ contains the individual contributions of the kinetic energy $T[\rho(\vec{r})]$, the classical Coulomb interaction $J[\rho(\vec{r})]$ and the non classical interactions (ncl) like exchange (x) and electron-correlation (c) effects, Equation 2.3:

$$F[\rho(\vec{r})] = T[\rho(\vec{r})] + J[\rho(\vec{r})] + E_{ncl}[\rho(\vec{r})] \quad . \tag{2.3}$$

Only $J[\rho(\vec{r})]$ is known. The kinetic energy and all non-classical contribution still need to be determined at this point.

To summarize, the HK theorems are the foundations of DFT. However, they only state that the ground-state density contains all the information about a system and that the true ground state density will minimize the energy. Yet, formally, one still needs to obtain the ground state wave function first in order to determine the ground state density. However, as the wave function is a multidimensional problem of 3N complexity nothing is gained so far. It is the Kohn-Sham approach which allows to circumvent this problem by introducing an auxiliary system of non-interacting particles which will be discussed in the next section.

2.1.2 The Kohn-Sham System

While the HK theorems establish the foundation of DFT, it is the Kohn-Sham approach which gives a recipe on how one can obtain the ground state density without evaluation of the ground state wavefunction. The idea behind the Kohn-Sham approach is to introduce an auxiliary system of non-interacting electrons. However, these electrons are subject to an effective potential which is designed in such a way so that the density of the non-interacting auxiliary system exactly matches the ground state density of the true interacting system. The total energy within the Kohn-Sham formalism is then given by

$$E^{KS} = T_s^{KS}[\rho(\vec{r})] + \int d\vec{r} \quad V_{ext}(\vec{r})\ \rho(\vec{r}) + J[\rho(\vec{r})] + E_{XC}[\rho(\vec{r})] \quad . \tag{2.4}$$

Here, T_s^{KS} is the kinetic energy of the non-interacting system which is a quantity which can be easily calculated in contrast to the kinetic energy of the fully interacting system. Again, J is the classical Coulomb interaction of a charge density and V_{ext} is the external potential due to the nuclei. E_{XC} is the so called exchange-correlation contribution which contains all non-classical interactions like exchange and correlation. In other words, E_{XC} contains all the missing information of the non-interacting system which is not captured by the other terms. In general, one can describe the Kohn-Sham approach as mapping an interacting particle system onto a non-interacting system. Thus the Kohn-Sham approach give rise to the so called Kohn-Sham equations which define the electron orbitals ψ_i,

$$\left[-\frac{\nabla^2}{2} + V_{ext} + V_J + V_{XC} \right] \psi_i = \epsilon_i \psi_i \quad . \tag{2.5}$$

This set of equations define single particle orbitals also called Kohn-Sham states. The density of the interacting electrons is then given by

$$\rho_0 = \sum_i |\psi_i\,(r)\,|^2 \quad . \tag{2.6}$$

In principle the Kohn-Sham orbitals do not have any physical meaning at all, as they are the orbitals of the non-interacting electron system. Their only job is to yield the ground state density, however, in many practical cases the orbitals provide a very good qualitative picture. So far no approximations have been introduced and the Kohn-Sham formulation is in principle an exact theory. However, as the exact exchange-correlation functional is not know, this part is usually constructed under some specific assumption. Thus, Kohn-Sham DFT is in practice only an approximate solution to the many body problem. One particular challenge for constructing a suitable exchange-correlation description is the requirement that it has to account for the self-interaction error (SIE). J describes the classical Coulomb interaction of charge densities (sometimes V_J is also described as V_H, the Hartree potential). Unfortunately J also gives a contribution if there is only one electron present in the system. As a consequence, the electron will interact with itself which yields an over-delocalization of the electron cloud. Many qualitative failures of DFT such as the band gap problem can be attributed to the SIE. [97] For a one electron system, it is quite trivial to account for the self-interaction as it is equal to $J - J$, *i.e.*, it should be zero. For a many electron system the exact amount of self-interaction is however generally not known. Of course other challenges to the construction of V_{XC} is the correct modeling of exchange and correlation in terms of the density.

2.1.3 Approximation for the Exchange-Correlation Functional

The exchange-correlation functional E_{XC} is the part which contains all the "unknown" contributions to the electronic energy. The "unknown" parts are the non-classical portion of the electron-electron interaction as well as the correction for the self-interaction. On top the part of kinetic energy that is not covered by the non-interacting reference system is also contained in there. Unfortunately, the exact form of the exchange-correlation functional is not known and approximations are necessary. The latter ultimately determine the quality of the DFT treatment. Despite decades of research, finding new and better approximations is still an active field of research as the exact form still remains a mystery. [96,98]

In general different approximations to E_{XC} can be grouped according to the so called Jacob's Ladder. Different rungs of this ladder represent different levels of approximation while the lowest rung represents the least sophisticated ones. With increasing rung one usually obtains more and more accurate approximations, however, the computational effort will increase concomitantly. [99] Functionals which are based on the local density approximation (LDA) are classed on the lowest rung of the ladder. Here, the exchange-correlation functional is derived form the homogeneous electron gas model and it only depends on the local value of the density. Not, surprisingly this type of functionals work already quite well for systems with an almost uniform density distribution such as metals. However, it will fail for systems with strong varying density such as molecules. An improvement can be obtained by also taking into account the gradient of the density. This leads to the so called generalized gradient approximation (GGA) functionals which form the second rung of the ladder. The most prominent example is the parametrization after Perdew, Burke, and Ernzerhof (PBE) [100] which showed great success in describing metals, semiconductors and equilibrium geometries. Further, by inclusion of the Laplacian and the orbital kinetic energy density one obtains the so called meta-GGA functionals which form the next rung. [101] Rung four consists of hybrid functionals. The term hybrid comes from the fact that these functionals contain a part of exact exchange coming from Hartree-Fock theory. The idea is quite simple as within Hartee-Fock theory the spurious self-interaction is completely canceled out by the corresponding exact exchange term. However, this comes with a cost, as the evaluation of the exact-exchange contribution involves the calculation of four-center two-electron integrals which is computationally rather demanding. Nevertheless, hybrid functionals usually yield good results for molecules [102] and semiconductors, especially if the semiconductor shows significantly covalent bonding character, like TiO_2 or $Li_4Ti_5O_{12}$. [97, 103]

2.2 Density Functional Tight Binding Theory

In this section the basics of the tight binding theory are presented. An overview on the parameterization specifically for the lithium intercalated graphite system used in this thesis is described. This methodological part is required for the next step within the multi-level approach. One of the reason that the methodology and results are overlapping within this section.

2.2.1 General Concepts on DFTB

Despite modern computer power, tractable system sizes with DFT are in the order of up to several hundred atoms maximum. If one is interested in larger systems one would treat the atoms in a classical way with a force field (FF) or other related techniques. [94, 104–106]. However, the description with force fields might not be good enough for systems which are characterized by subtle balances between van der Waals and electrostatic interactions, like lithium intercalated graphite. [107] In that case density functional tight binding theory (DFTB) is a good alternative. [108–110] In general, DFTB can be regarded as a second-order approximation to DFT with a semiempirical tight binding simplification. [111] With DFTB the same system sizes as with a force field description are easily accessible. Computational cost as well as computational time are usually also comparable. However, with DFTB one still has access to the electronic structure of the system [106, 110]. The disadvantage though is the necessity of parametrization and most of the time new parameters are necessary if one wants to treat a new system, but using force fields one is confronted with similar challenges. [111] Hence, DFTB is not a fully *ab initio* method, and its performance will largely depend on a good parametrization. In general the parametrization is obtained using DFT reference data. Once a suitable parameter set is obtained, reparametrization for a chemically similar system is expected to be relatively easy, *e.g.* the carbon parameters for the intercalation of Li can be easily adapted to describe the intercalation process of Na and K. The starting point for the DFTB approximation is the second order expansion of the DFT ground state energy around a fictitious non-interacting auxiliary system with density ρ_0, which can be conceptually divided into three terms:

$$\begin{aligned} E[\delta\rho, \rho_0] =& \Big\{ \sum_a f_a \langle \psi_a | -\frac{1}{2}\nabla^2 + V_{ext} + V_H[\rho_0] + V_{XC}[\rho_0] | \psi_a \rangle \Big\} + \\ & \Big\{ \frac{1}{2} \iint \left(\frac{\partial^2 E_{XC}[\rho_0]}{\partial\rho\partial\rho'} + \frac{1}{||\vec{r} - \vec{r}^{\prime}||} \right) \partial\rho\partial\rho^{\prime} d\vec{r} d\vec{r}^{\prime} \Big\} + \\ & - \Big\{ \int V_H[\rho_0](\vec{r})\rho_0 \vec{r} d\vec{r} - E_{XC}[\rho_0] + \int V_{XC}[\rho_0](\vec{r})\rho_0 \vec{r} d\vec{r} - V_{NN} \Big\} = \\ & = E_{BS} + E_C + E_{REP} \quad . \end{aligned} \tag{2.7}$$

Within this formulation, E_{BS} corresponds to the band structure energy of the system, E_C is the Coulomb energy that accounts for the electrostatics interactions, and E_{REP} gives the repulsive energy that contains all the other contributions. [110, 111] This last one can be considered analogous to the exchange-correlation energy in DFT which was previously discussed in Section 2.1.3, as it contains (part of) the corresponding contributions (and others), but most importantly as its form is not *a priori* known. To make it even simpler, we can regroup those different parts into two main contributions: the electronic part, accounting for both the band structure and the Coulombic term, and repulsive part, which will be discussed separately below. Exploiting tight-binding approximations, these contributions can be cast into simple expressions which only depend on a handful of atomic parameters and pre-tabulated integrals. As such, the quality of DFTB will essentially depend on the quality of its parametrization. The parameters for the lithium and graphite are described in the paper by Panosetti *et al.* [112] For the electronic part an approach proposed by Chou *et al.* [113] was used, based on the particle swarm optimization algorithm [114]. For the repulsive part, a machine learning (ML) [115] algorithm based on Gaussian Process Regression (GPR) implemented in *GPrep* package was used [110, 112].

2.2.2 The Electronic Part

The so called "electronic part" of the total energy consists of the first two terms, the E_{BS} and the E_C of Equation 2.7. The band structure energy E_{BS} contains the contribution of all the total energy for the non interacting auxiliary-system, such as all the single-atom-contribution and the valence electrons effects. E_C is the Coulombic contribution to the electrostatic interaction, that also includes some exchange-correlation effects that comes from the coupling of mobile charge fluctuations. Then, to parameterize all the electronic part becomes non trivial, despite its simplified expression; however it is still largely non-empirical. The parameters needed for this contribution are essentially individual single-atom properties (the diagonal element ϵ of the non-interacting Hamiltonian, the Hubbard-U parameter), which can be in principle calculated directly *ab initio*, and the confinement potential to mimic the “compression” of atomic densities in a chemical environment. Each aspect will be an individual parameter for any chemical species in the system. The ϵ, as non-interacting energy values and the U, based on the chemical "hardness" of an atom have more physical meaning, whereas the confinement potential is a truly arbitrary parameter with a cutoff that can be defined for the diffuse tails of the basis orbitals. For this parametrization the Woods Saxon potential was used, that assures a smoother transition to zero in the orbital tails. [116]

$$V_{conf} = \frac{W}{1 + \exp(-a(r - r_a))} \tag{2.8}$$

with W that is the height, r_a the location of the midpoint and the a the slope of the potential [116, 117].

To determine the best combination for the above parameters a particle swarm optimization (PSO) algorithm was used. PSO draws its inspiration from a natural phenomenon, such as a bird swarm searching for food. [113, 114] The candidate solutions to the global optimization problem are represented by “particles”

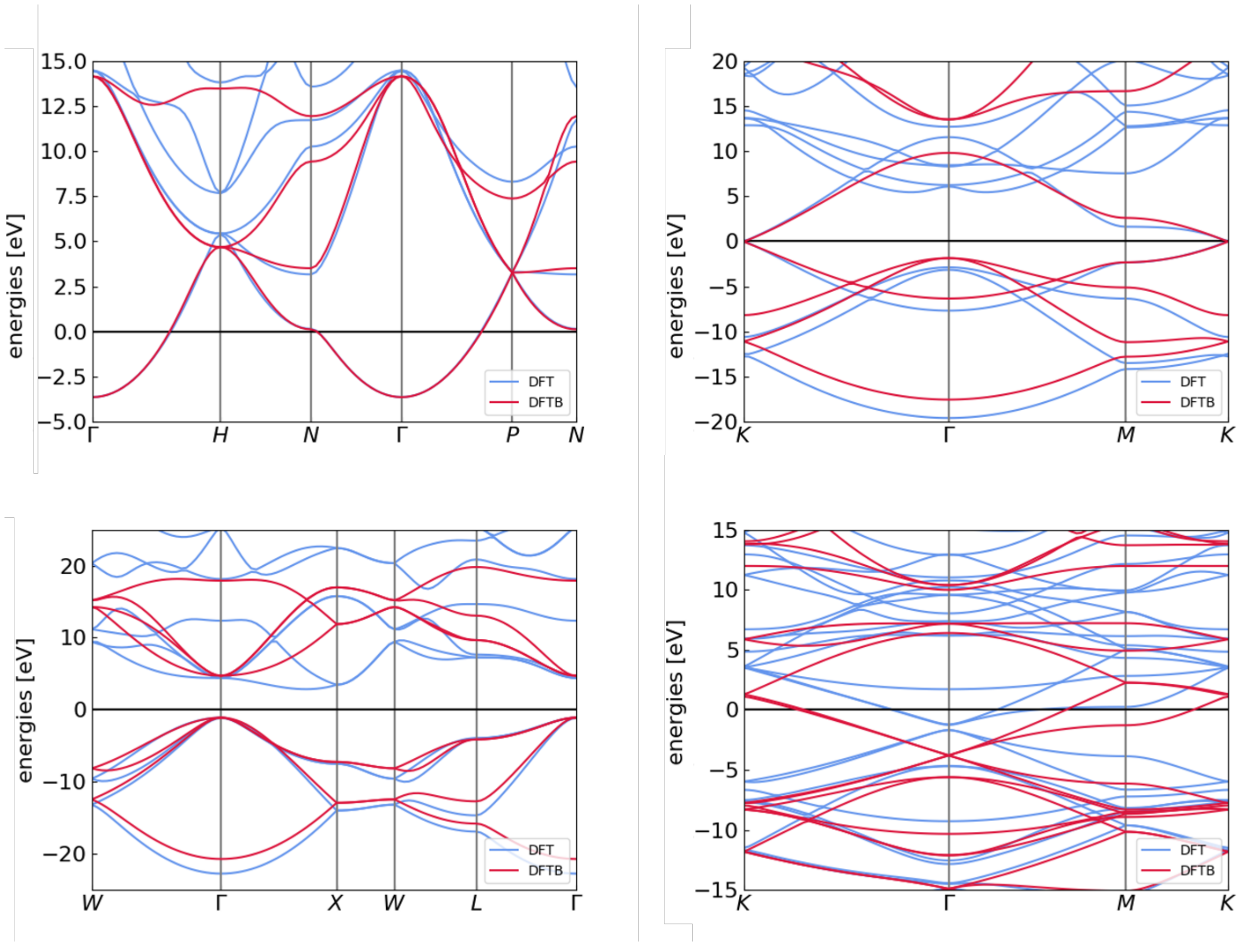

Figure 2.2 Comparison of the band structure between DFT (blue lines) calculated with the Perdew-Burke-Ernzerhof(PBE) [100] functional and our DFTB (red lines). In detail the plots show metallic lithium (upper left), graphene (upper right), diamond (lower left) and LiC_6(lower right) [112]. As one can clearly see, all important features of the DFT band structure are reproduced by DFTB with good accuracy.

which are moving through a search space like a swarm, guided by a combination of local and global criteria. Hereby, this is used to identify the best parameters for the electronic part. [111, 113] Each particle has a position in this space, that will correspond to a trial set of parameters p_i with coordinates corresponding to its individual components. [111, 117, 118] In a more specific way here, in the PSO the particle will represent a set of parameters (ϵ,U and the confinement constants), with which the electronic part of the DFTB is constructed and used to calculate one or more target properties. The deviation between the predicted and the corresponding properties calculated with DFT is the target function to minimize.

By means of a careful choice of properties to include in the cost function, i.e., only properties that do not depend on repulsion, one can conveniently separate the electronic parametrization from the parametrization of repulsion, which is generally much more complicated. The latter is then described in Section 2.2.3 For the electronic part, the targets were the band structures of the individual elements: metallic lithium, graphene and diamond, and the results were validated with respect to the mixed system LiC_6. Figure 2.2 shows the resulting band structures. [112] The mismatch is some parts is given by the intrinsic oversimplification of DFTB which uses a minimal (valence only) basis set.

2.2.3 The Repulsion Potential

The last but not least part from Equation 2.7 is the so called repulsive contribution E_{REP} to the energy. This part consists of the all terms that are not included in the electronic contribution. The repulsion potential in DFTB plays a similar role as the exchange-correlation in DFT. It covers underneath all the non-classical many-body effects. As such, the term "repulsive" is somewhat of a misnomer, as the interaction may just as well display attractive regions especially around equilibrium distances. It can be shown that E_{REP}, defined as the deviation between the "true" DFT energy and the "repulsion-less" DFTB energy, is adequately approximated as a sum of pairwise terms, as simple as:

$$E_{REP} := E_{DFT} - E_{BS} - E_C = \frac{1}{2}\sum_I \sum_{J \neq I} V_{REP}(R_{IJ}) \tag{2.9}$$

where $R_{IJ} = |R_I - R_J|$ is the distance between the chemical species that we account for within the sum. In this case the short-range pairwise potential V_{REP} depends only on the interatomic distance, which must be defined for each combination of elements. To enforce the short range-character one is using a cutoff radius. [110]

As in the quest for the exchange-correlation, there are different ways of approaching this problem and different fitting procedures. The problem of parametrizing a repulsive potential appears not only in DFTB but in any other tight binding approaches. [109] A common approach is to either choose a functional form *a priori* or represent the pairwise potentials with splines. In either case, the functional form has to be flexible enough to correctly represent the subtleties of the repulsive interactions. Practically, this means that the number of coefficients to fit per atomic species pair is rather large. Additionally, if one is targeting a parameter set for N atomic species, the parametrization of the pairwise potential is an N^2 effort. It is quite evident at this point that this is the most cumbersome part of the parametrizazion procedure, as well as dominating its entire cost. To avoid this and other shortcomings, here we rather adopt a machine learning approach to replace the classical fitting procedure.

To this end, V_{REP} was reformulated in the group by Panosetti *et al.* within the Bayesian machine learning framework of Gaussian Process Regression (GPR). [110] In the GPR setting it is important to sample a large set of training data points to cover all the interatomic distance ranges and chemical environments in order to have a good representation of the system studied. The parameterization used in this work was done for the repulsive potentials for C-C and Li-C only, the Li-Li repulsive is available as well now, however, in this thesis all the models that were prepared for the `kmos` application, involved the energy barriers from the DFTB parameterization without the Li-Li repulsion. [112, 119]

Gaussian Process Regresson

A general Gaussian process is a multivariate Gaussian distribution that can be applied for any random variable. In this context, random variables represent a target function value f_* at a certain input x_*. In GPR, V_{REP} is modeled as a linear combination of covariance (kernel) functions

$$V_{REP}(R) = \sum_{I,J \in X} \alpha_{IJ} k(R, R_{IJ}) \tag{2.10}$$

where the sum is over all N_{pairs} of I, J, in the set of reference structures $\boldsymbol{X}$, with regression coefficients α_{IJ} and the Kernel function $k(R, R_{IJ})$. Without going into more details, the ML-based approach used to fit repulsive potentials in DFTB, named as `GPrep`, is essentially a simplified version of the Gaussian Approximation Potential (GAP) approach of Bartók *et al.* [110, 120], with the main difference consisting in the use of a pairwise descriptor (the interatomic distance) rather than the many-body smooth overlap of atomic positions (SOAP). Both GAP and `GPrep` allow to train on energies or forces or both. Here, we only trained on forces.

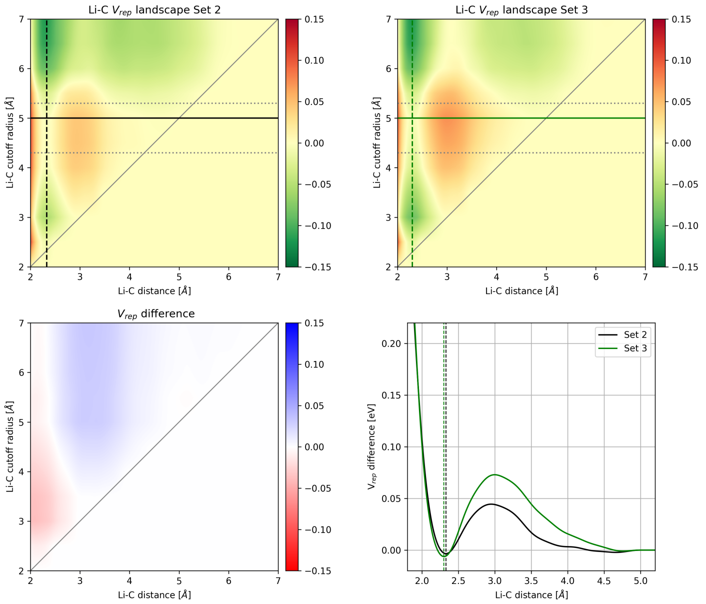

Figure 2.3 Upper left and right: 2D repulsion potential landscape (energy is given in eV, expressed by the color bar) depending on the chosen Li-C cutoff radius (y-axis) for different sets, used in the parameterization. The black and green dashed lines represent the next-neighbor Li-C distance for the respectively sets. The diagonal line are the cutoff radii, at which the potential is set to zero. The plateaus are highlighted between thin dotted lines. Bottom left : influence of the inclusion of MBD vs LJ force residues in the training data on the repulsion potential (energy is given in eV, expresed by the color bar). Bottom right: the detailed repulsion potentials at $R_{cut}^{LiC_6} = 5.0$ Ångstrom [112].

A Gaussian, or squared exponential (SE) kernel was employed, of the form

$$k_{SE}(\vec{x}_1, \vec{x}_2) = \delta^2 \exp\left(\frac{-(\vec{x}_1 - \vec{x}_2)^2}{2\theta^2}\right) \tag{2.11}$$

where θ is a length scale, within the target value and can be seen as a measure of smoothness. δ^2 is the target variance from the prior distribution. The σ_n as one of the hyperparameters will prevent over-fitting and the posterior mean only depends on the quotient σ_n/δ.

Van der Waals Interaction

Van der Waals (vdW) forces are weak attractive intermolecular forces. Usually they are decaying with an order of R^{-6} with respect to the distance between the interacting particles. They are important for the so called dilute systems or low state of charge, if referring to the world of layered battery materials such as lithium-graphite. Tackling the domain model within the structure of the anode requires as well to take into account even more the interactions between the graphite layers. Hence, the origin of those interactions are mainly induced by van der Waals forces. PBE-DFT, commonly used as the reference for the DFTB parametrization, does not include the van der Waals interactions. These usually are added then in a post-processing step. Different approaches are available with variable accuracy and computational costs, from the cheapest dispersion correction Lennard Jones (LJ), passing through the semi-empirical approximation by Grimme [121] and the Tkatchenko-Scheffler (TS) [122, 123] scheme based on the electron density, where van der Waals interactions are derived from the ground state electron density and free atom references. Among the available vdW methods, the Many-Body dispersion (MBD) correction, which is density-based like TS, showed satisfactory results for lithium intercalated graphite, however its cost when integrated into the DFTB will make the method more expensive, despite still cheaper than DFT. [122, 123] Most importantly, we observed that the description of higher states of charge is already sufficient at the

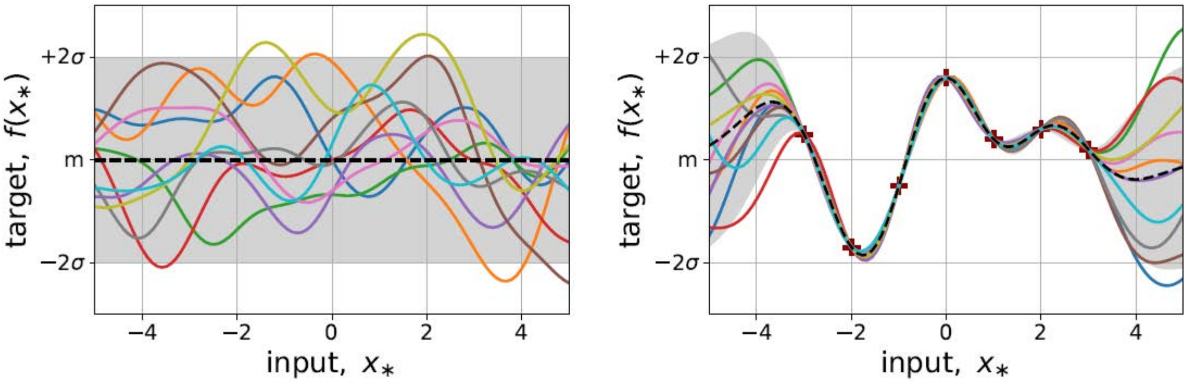

Figure 2.4 Depiction of Gaussian process regression (GPR) in 1D input space. The figures represent a finite subset of 100 equidistant random variables according to Engelmann *et al.* [115] within the given range. The black dashed line marks the mean of the distribution. The gray shaed region shows twice the standard deviation of the target variables. The colored lines are random target vectors f_*, from the corresponding probability distribution. Left: The representation of a Prior distribution of a Gaussian process. Right: Conditioned the prior distribution on the training data (red crosses) is obtained the posterior distribution used to train or (machine learn) in the context of the GPR. The figure has been reproduced from Engelmann *et al.* [115] on courtesy from the author.

PBE level, while at the same time MBD suffers increasingly more from numerical issues as the content of lithium increases. In other words, there is no approach that performs equally well across the entire range of states of charge. The idea is then to exploit the Machine-learning approach to encode the deviation between MBD (in the reference data) and LJ (which is readily computable with DFTB) for the dilute Li-graphite systems directly in the repulsive potential. In this way, with a careful choice of the training set, including both PBE (for high states of charge) and PBD+MBD (for low state of charge) forces, we teach the repulsive potential the correct behaviour at any state of charge. The detailed parametrization procedure is described in the paper by Panosetti *et al.*. [112]

2.2.4 Energy Barriers and Transition State Theory

Energy barriers are required when it is necessary to describe a diffusion process or any processes that involve a non static reaction. Those can be obtained theoretically with different methods and accuracy. The most used one though is Transition State Theory (TST). Transition State Theory (TST) can provide rate constants required as input for our next level, the kinetic Monte-Carlo (kMC). [124–126] TST is valid under the assumption that in a process that goes from state A to state B will not come back. Hence, one can write the expression for the transition from $A \longrightarrow B$ known as Eyring-Polanyi

$$k^{TST}(A \rightarrow B) = \frac{q_{TS}^{vib} k_B T}{h q_A^{vib}} \exp\left(\frac{-\Delta E_{(A\rightarrow B)}}{k_B T}\right) \tag{2.12}$$

where T is the temperature, h is Planck's constant q_{TS}^{vib} and q_A^{vib} are vibrational partition functions at the transition state and at the reactant respectively, $\Delta E_{(A\rightarrow B)}$ is then the activation barrier of the process. The latter is directly available from the PES information, based on first-principles calculations. [126] In other words, TST will estimate the velocity of the transition from one state to another (rate constant) passing through a high energy region on the PES. The resulting expression of the TST is formally equivalent to the empirical Arrhenius relation;

$$k = A \exp\left(-\frac{E_a}{k_B T}\right) \tag{2.13}$$

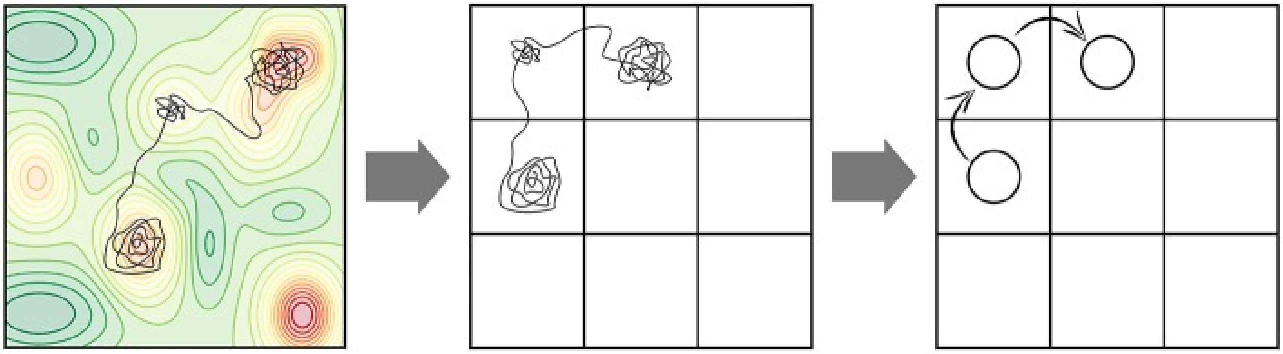

Figure 2.5 Example of a coarse-grained molecular dynamics (MD) trajectory into a Markov chain. Left: Potential energy surface (PES) of a system with the lower-energy basins in red. The MD(black line) is the trajectory that is coarsed-grained. The time spent in these PES basins are vibrationl motion around the minima, followed by the escape route at a certain time. As one can see from the behaviour, the system spends quite a significant time in those minima. Center: The translation of the PES minima into position on a suitable defined lattice. Right: The final representation of the continuous MD trajectory into a Markov chain as hops between different positions on the lattice. The figure has been reproduced from Anderson *et al.* [127] on courtesy from the author.

where A is the pre-exponential factor, related to the frequency of the successful collisions and depending on the order of the reaction. The entropic effects are also incorporated within the pre-exponential factor. In solid state systems TST is also known under the Harmonic Transition State Theory (HTST). [124] This assumes in more detail that the harmonic approximation can be used for the local minima on the PES and the transition states. In fact the transition states on the PES can be seen as saddle points of first order, and the lowest is taken as the activation barrier of the relevant reaction/process.

In the presence of any other alteration on the transition process, *i.e.* electrostatic potentials acting on the actual process, thus the energy barrier (E_A) will be shifted or altered. This can be used in the kMC subsequently, by adapting the raw simple activation energy barrier accordingly. Thus, the starting point is based on first principles with the activation barriers extracted from DFTB through the Nudged Elastic Band (NEB) approach. [110, 112] NEB is just a selected computational method that gives access to transition states. There are several different computational methods with more detailed and complex approximations, but that will go beyond this work. [128] The Nudged Elastic Band (NEB) method is part of the chain-of state class of methods, that involves a chain of images optimized simultaneously until they converge them to the minimum energy path (MEP). Moreover, that will estimate directly the path between the initial state (IS) and the final state (FS) without using the second derivative energy for the calculation, making it cheap. The starting point is the construction of the IS and FS, preferably with sensible guesses. Those are optimized individually, and then when possible linear interpolation or a more complex scheme between them is used to identify some replicas between IS and FS. The replica images are connected with springs, which will give the name to the so called simplified elastic band (EB) concept. The images are then optimized simultaneously in order to match the MEP, using the spring forces for keeping the images together. However, the EB is not performing well and has problems such as corner cutting and down-sliding. To correct those, the EB is "nudged", that is, the forces are projected in such a way that the gradient forces only act perpendicularly to the chain, while spring forces only act parallel to the chain. The resulting Nudged Elastic Band (NEB) method can be used in combination with the so-called "climbing image" (CI). The idea of the CI is to change the forces affecting one of the NEB-image so it would converge to the TS. The highest one in energy is chosen as the climbing image. This image is not affected by the spring forces and the true force is applied with inverted parallel component. As a result, the energy of the climbing image is maximized and it reaches an accurate value of the TS, with the same computational cost as for the classical NEB. A representation of the search is in Figure 2.6. For all the energetics the parameterization of the DFTB described in Panosetti *et al.* was used. [110] In the following work of

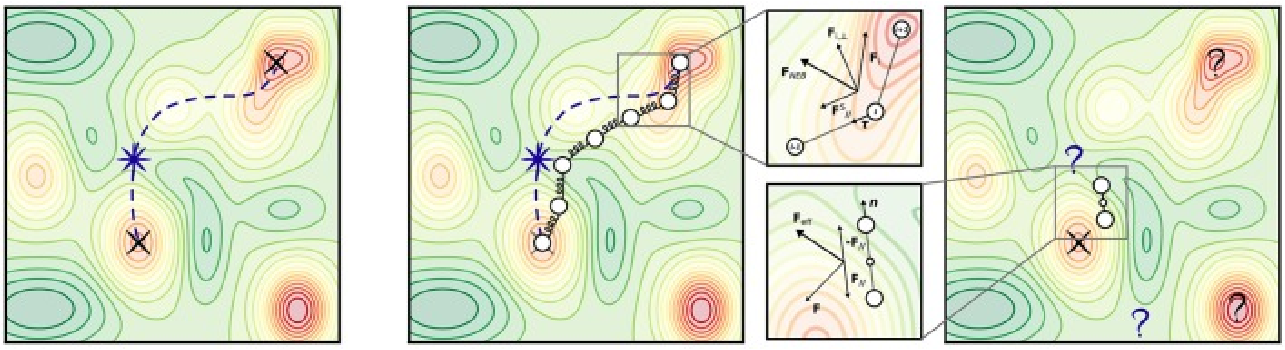

Figure 2.6 Representations of different methods for the search of transitions states. Left: Initial state, Final state and Transition sate. Center: The Nudge elastic band (NEB) method. Here, spring forces are added along a band between the images. This determines the NEB force acting on an image i at a certain optimization step. Right: The dimer method. The magnified panel shows the composition of forces which determines the effective force acting on a dimer at a certain optimization step, after the constrained minimization with respect to orientation. The figure has been reproduced from Anderson *et al.* [127] on courtesy from the author.

Anniés *et al.* [119] the DFTB parameterization was adapted to account for the lithium-lithium repulsive intra/inter-layer contribution, however, here all the models involved were built on the previous one without Li-Li repulsion. For further details, the reader is referred to the work of Panosetti *et al.*. The used diffusion barriers which are included within the `kmos` model can also be found there. [112]

As activation barrier for the $\mathrm{LiC_6}$ as stage I 503 meV was identified and then the subsequent next level was pursued. [112] Ideally we want to reduce the usage of low length and time scales to a minimum. Therefore, we obtain the initial activation barrier from DFTB and then move forward. To effectively connect to experimental studies, a theoretical framework for simulating large-scale and long-duration non equilibrium processes in the graphite anode, based on kinetic Monte Carlo simulations is required. [112, 127]

2.3 Kinetic Monte Carlo

kMC models can be applied to describe different processes in materials from diffusion to different kinds of catalysis. In this work, however all the focus will be put on the diffusion properties applied within the field of LIBs, in particular diffusion coefficients of the lithium ions within the ideal host system of the HOPG. Within this chapter, the standard kinetic Monte Carlo approach will be introduced together with the `kmos` code. [129]

2.3.1 kMC in a Nutshell

Describing dynamical properties of chemical or physical processes from an atomistic point of view can be challenging depending on the actual time and lengths scale that we are looking for. The variation of the lengths and time scale in the laboratory frameworks, such as micrometers to centimeters from one side and seconds from the other side, promoted the usage of kMC. In fact, kinetics are generally studied on meso- or macroscopic scale. kMC is an evolution of the classic Monte Carlo, where the kinetics can be interpreted as a temporal evolution of the system. [124] To describe the dynamics of a process, i.e., that evolves from state to state, kinetic Monte Carlo is one of the suitable algorithms. Despite the fact that the algorithm appeared within the 60s, the terminology got settled to kMC in the early 90s and took over a range of applications since then. It keeps being used as a common tool for studying materials from catalysis, to any kind of ultra material storage, passing through irradiation, surface adsorption, diffusion and crystal growth. [124, 125] Ideally, kMC can give the exact dynamical evolution of a system, however, in practice a full dynamical evolution is challenging. The aim is simulating the dynamical evolution of systems of atoms cheaply and within a certain accuracy for a specific property, *i.e.*, in our case, diffusion. kMC exploits the fact that the long-time dynamics of the specific system typically consists of activated diffusive jumps from state to state. The key assumption is that the jumps are Markovian. Markovian processes are "memoryless", meaning that the transition probabilities are constant over the trajectory and the state transition probability during each time step solely depends on the previous state. Hence, within the Markovian approximation, the evolution of the system will depend on the transition probabilities of individual elementary jumps, that can be calculated based on the current configuration of the state-to-state dynamics. This evolution will be time dependent and is generally described by a differential equation of first order, the Master Equation 2.14 [130].

$$\frac{dp(x,t)}{dt} = \sum_y k(y \to x)p(y,t) - \sum_y k(x \to y)p(x,t), \tag{2.14}$$

where $k(y \to x)$ is the transition rate for the transition from state y to state x and can be identified with the rate constants from Section 2.2.4. In the context of ion diffusion of only one type of cations, it is convenient to consider the state x as filled with zeros and ones, where $x_i = 1$ means that an ion is occupying the i-th site and $x_i = 0$ indicates that the i-th site is empty. For the later discussion, it is convenient to group the transitions $x \to y$ into processes ξ

$$\xi : \quad x \to x + d_\xi \tag{2.15}$$

where d_ξ is the change in the state due to execution of the processes ξ and independent of the current realisation x. Since each rare event will only affect a few sites in the near vicinity to each other, the vector d_ξ will be sparse, i.e. zero in all entries except those corresponding to the affected sites, and the number of process will scale linearly in the number of sites. We can then rewrite the master equation as

$$\frac{dp(x,t)}{dt} = \sum_\xi r_\xi(x - d_\xi)p(x - d_\xi, t) - \sum_\xi r_\xi(x)p(x,t), \tag{2.16}$$

where $r_\xi(x)$ is the rate function of the process ξ and is formally given by

$$r_\xi(x) = k(x \to x + d_\xi) \tag{2.17}$$

As one can deduce, Master equation is at the base of all kMC simulations and solving the Master Equation is mainly working on the rates necessary for the propagation of the system.

2.3.2 Rate Constants in kMC

Knowing the rate constants that corresponds to the processes that one needs to describe within kMC allows as well to reproduce longer time scales, on the orders of seconds or well beyond within a reasonable computational time. [124, 125] The simplest way of approximating the rate constant for escape from one state to another is by the equilibrium flux through a dividing surface separating the two states, and is given by the TST (see Figure 2.6 and Section 2.2.4) proposed first in 1915 by Marcelin. [131] Looking in detail at each trajectory in the ensemble, it will be necessary to count the number of forward crossing through the dividing surface per unit time and divide this by the number of trajectories, on average, that are in state i at any time, we obtain the TST rate constant, k_{ij}^{TST}. Since the TST is an equilibrium theory, we can calculate k_{ij}^{TST} without even looking at dynamical trajectories. For a thermal ensemble, k_{ij}^{TST} is simply proportional to the Boltzmann probability of being at the dividing surface relative to the probability of being anywhere in state i. In a computer implementation this can be realized with an array of partials sums. The array element sj represents the lengths of all the objects up to and including object j. With $s(j)$ being

$$s(j) = \sum_q^i k_{iq} \quad . \tag{2.18}$$

One then draws a random number r, distributed on (0,1), multiplies it by k_{tot}, and iterates element-wise through s, the first element for which $s(j) > rk_{tot}$ is the selected pathway.

As mentioned before, the models are sensitive to the predefined rates. On top, if an external force in one of the directions is applied to a system with charged particles, a concentration gradient is expected as well. This gradient induces a flux of charged particles in a certain direction. Furthermore the flux is influenced by the electrostatic interaction between the jumping charge carriers. To investigate the effect of the electrostatic interaction on the particle flux, an adjusted formulation of kMC, which is driven by an external potential, is required. That will be discussed in the chapter 5. The *on the fly* concept arises from the fact that keeping the rate catalog on the lattice processes can still mislead or bring bias within the generation of the paths. Keeping the system on lattice precludes certain types of diffusive events, considering that the rate catalogs are based on intuition and most of the time pre-conditioned by the system knowledge. On top the real dynamics are more complicated then expected. [124]

2.3.3 kMC in `kmos`

The code which was used for carrying out all the relevant kmc calculations is the open source package `kmos`. For more details the reader is referred to the documentation of the code *http://kmos.readthedocs.io* . [129, 132] The `kmos` package was developed previously in the group [129, 132] with the main application on the heterogeneous catalysis. [127, 133]. This allows to obtain mesoscopic averages of quantities such as turn over frequencies from the first principles, that ultimately are required for simulation of the reactor level kinetics or the optimal conditions of operation to maximize the performance. [104, 127] The quality of the latter, breaks down to the quality of the input data again. Thus, it is important to get reliable inputs.

$$d\rho_i(t)/dt = \sum_j (k_{ij}\rho_j(t)) - \sum_j (k_{ji}\rho_i(t)) = \sum_j (k_{ij}\rho_j(t)) - \rho_j(t)\sum_j (k_{ji}) \quad . \tag{2.19}$$

To be able to use the implementation from `kmos`, it is required to map the problem onto a lattice, and to identify the elementary processes with the respective rate constants. [129, 134]

In order to run the kMC model in `kmos` and other on-lattice kMC implementations [124] one needs to prefill the lattice sites with some particles. Starting the simulation with a completely empty lattice, would directly bring to a deadlock where no processes are possible. [124, 129] The atoms in the system are mapped onto a lattice. An event may move one atom or many atoms, perhaps in a complicated way, but in the final state, each atom will again be mapped onto a unique lattice point. The rates are as described above, and each process requires a unique rate through TST. In principle, calculating the rate for any distinct process requires that the system should be relaxed to find the minimum energy at the starting point and frequencies at the minimum. After relaxation, the atoms will in general no longer be positioned on the lattice points, especially for atoms near defects. However, if the atomic positions do not change much during the relaxation, then each atom is sufficiently close to a lattice point and it is safe to map the system onto a lattice in this way to simplify the KMC and the generation of the rate constants. Lattice mapping also makes it easy to exploit locality in determining rates. We assume that only the atoms near a defect affect the rate constant for any change or migration of that defect. The example in Figure 2.7 is representing these ideas.

The jump of a lattice vacancy, will be affected locally by the environment, the labeled sites (1-10) can be either occupied or vacant and will influence the transition of the moving atom. This will be reflected on the rate constant. As one can imagine based on that, the possible rates, ignoring the symmetry, can grow quickly and will be explicitly dependent on the number of sites and the number of the possible atom types that can sit on those sites: [124]

$$n_{rate} = (n_{type} + 1)^{n_{site}} \tag{2.20}$$

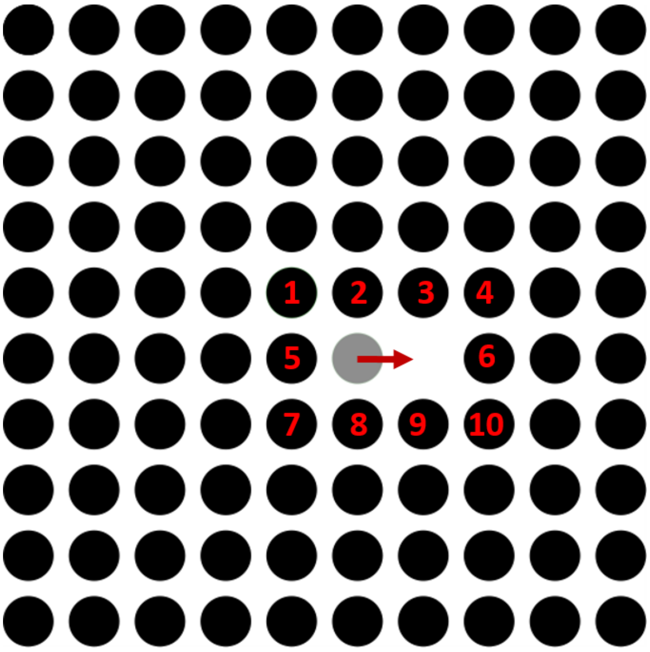

Figure 2.7 Schematic representation of a rate catalog example for the diffusional jump of a random vacancy in a solid matrix. The sites which are labelled from 1-10 can affect the rate constant of the so called representative atom depicted in grey. This influence will be assessed within the kMC simulation and will enter into the description of the rate constant for the next jump in any direction of the environment. Figure adapted from Voter *et al.*. [124]

where n_{site} is the number of sites explicitly considered (n_{site} = 10) and n_{type} is the number of possible atom types that can be each of those sites. This is a simplistic view; as soon as we go to a realistic chemical system, that can get quickly complicated, as some pathways might include multiple vacancies and a variety of atoms. Additionally, if it is sufficient to consider just the so called nearest neighbours, this is still feasible; however if going to second or third, the number of rates to be computed increases very rapidly, complicating the compilation of the "rate catalog". This can be addressed and reduced by splitting the neighborhood into two sets of sites, but, in some cases, it can become advantageous to compute the barriers on the fly instead. The latter approach consists in calculating the rate catalog as the kMC simulation proceeds, so that the rate constants are computed only for those environments encountered during the kMC. [135–137] That allows us to approximate the rate constant of a random process *on-the-fly* within the `kmos`, based on the consideration of the nearest neighbors. That calculates the processes during each MC step, allowing to save computational costs. Large scale atomistic simulations typically pursue force field approaches, well described within the upper end of the SOC, however, those approaches are limited when it comes to the entire range of different SOC. [127, 129] In our case we will be dealing with hopping diffusion, that normally does not involve particularly sensitive or overall rate-limiting elementary processes. [138] When kMC is correctly replicating the microkinetic events of a system, the overall behavior of a collection of free-wandering particles must coincide with the analytical solutions of Fick's laws at the continuum level 2.4. [94].

2.4 Continuum

The final descriptive level of a multiscale approach is the continuum level. Although not performed in this work, the full approach it is described briefly below for completeness. Ideally in this part, once the diffusion coefficient was assessed and associated to a process, ideally from the first principles, the quality of these parameters will reflect in the prediction of the performance of the material. With that said, it is not trivial how the final performance of the full cell within the electric device will be affected by all the other components of the lithium ion battery. The problem becomes quickly a multidimensional and a multi-physics system. In the context of battery materials modelling, the influence of the liquid electrolyte on the solid phase of the electrodes, as well as the electrochemical-thermal phenomena are then taken into account on this scale. The Li ion transport within the solid will be as well influenced by these processes, as well as the other way around. This makes the predictability quite hard to address. [28,139,140] There are different mathematical models to address this complexity; however, the fundamental principle within all of these electrochemical models was established by Newman and co-workers. [141–144] The so-called Newman model is based on the Maxwell-Stefan equation, that allows to describe the transport of the ions within the liquid electrolytes and the porous electrode in a homogeneous way. Due to its simplicity it is still the main workhorse for theoretical modeling. The principles of irreversible thermodynamics state that the flux of one species is inherently coupled to the fluxes of all other species present, as set forth in Stefan-Maxwell equations:

$$c_i \varDelta \mu_i = \sum_j \frac{c_i c_j}{c_T D_{ij}} (v_j - v_i) \quad . \tag{2.21}$$

Here, c_i is the concentration, D_{ij} are the diffusion coefficients, v the velocity, i and j the species indices and C_t is the total molar concentration. In the simplest version, the Newman model takes the form of the Planck-Nernst equation representing the competition between the transport (drift) of charged particles due to an electric field and their diffusion. Here, the ionic fluxes are taking into account the diffusion and electromigration in a mean electric field, which is described self-consistently from the mean ionic charge density via Poisson's equation.

Those methods developed to include more and more complexity, to be able to integrate further advancements in battery systems. The model addresses the electrolyte concentration, electrolyte potential, solid-state potential, solid-state concentration of the ions within the porous electrodes and the electrolyte concentration and potential within the separator. This model includes the principles of the transport phenomena, electrochemistry, and thermodynamics within nonlinear partial differential equations (PDEs) space, velocity and time. However, by incorporating so many variables one disadvantage is that disentangling the limiting factors is quite a difficult task. [139,145] As mentioned, each of those will influence the performance and the reliability of the predictive models. Each of those is challenging in its own complexity. However, the solid state diffusion within the electrode material, as well as at the interface, remains one of the key parameters. There are many models build on that, and to recall a few of them Singht, Ceder and Bazant introduced the idea of using Cahn-Hilliard model to account for phase transformations that occur in solid state particles during intercalation. [145,146]

$$N_{c,i} = c_i v_i \quad . \tag{2.22}$$

where c_i is the concentration of the species and v_i is the velocity of the medium.

$$N_m = -z_i u_i F c_i \varDelta \varPhi \quad . \tag{2.23}$$

with N_m, with z_i is the charge of the species i, u_i the mobility, F the Faraday constant, c_i the concentration of the species i and $\varDelta\varPhi$ the so called voltage if in continuum. Diffusion is also given by

$$D_i = u_i RT \quad . \tag{2.24}$$

and combining the equations 2.23 and 2.24 gives

$$N_m = -z_i \frac{D_i}{RT} F c_i \varDelta \varPhi \quad . \tag{2.25}$$

The latter will be used later to help in bridging the gap between the mesoscale and the continuum.

2.4.1 Fickian Diffusion in a Solid Matrix from a Continuum Perspective

The classical way of calculating the diffusion is through Fick's law.

$$\boldsymbol{N_s} = -\boldsymbol{D_s}\boldsymbol{\nabla}\boldsymbol{c_s} \quad . \tag{2.26}$$

$$\frac{\partial \boldsymbol{c_s}}{\partial \boldsymbol{t}} = -\boldsymbol{\nabla}\boldsymbol{N_s} \quad . \tag{2.27}$$

To describe the connection of kMC with Fick's law we can take a simple scenario: an infinite one-dimensional slab of intercalation material, having an initial uniform occupation degree x_0 occupying a portion of size *l* in the center of the slab, equation:

$$\frac{\delta x(r,t)}{\delta t} = -D(\frac{\delta^2 x(r,t)}{\delta r^2}) \quad . \tag{2.28}$$

where the occupation at t = 0 is

$$x(r,0) = \{x_0 if |r| \leq l/20 if |r| > l/2 \quad . \tag{2.29}$$

Once again to connect this with kMC simulations, let us consider the diffusion of non interacting particles, where we have the following relationships:

$$D = \mathit{\Gamma}(x)\lambda^2 \quad , \tag{2.30}$$

and

$$\mathit{\Gamma}(x) = \mathit{\Gamma}(0)(1-x) \quad . \tag{2.31}$$

$$N_M = \frac{D}{D_{eff}} \quad . \tag{2.32}$$

at the end the $D_{eff} = (1/N_M)D = \epsilon_l^{1.5} D$

The Poisson equation gives the connection between the charge density and the potential and can be used to bridge the scale from the mesoscale to the continuum:

$$\nabla\nabla\varphi = -\frac{4\pi\rho}{\varepsilon} \quad . \tag{2.33}$$

3 Theoretical and Experimental Background on the Nuclear Magnetic Resonance (NMR)

This chapter presents the theoretical and experimental background to understand the basic concepts of the Nuclear Magnetic Resonance (NMR) spectroscopy. NMR is known to be able to provide information about the local electronic structure and dynamics directly from the nuclei that are investigated. A brief description on the ^{7}Li nucleus, and its characteristics within the NMR context will be given. Additionally, a quick description on how atomistic dynamics are assessed with NMR techniques at different time and length scales.

The spin alignment echo (SAE) and the inverse Laplace transform (ILT) will be introduced to describe the techniques relevant for the purpose of this thesis. The focus will be on how to extract correlation times from the (ILT)-SAE-NMR that can consequently be related to a diffusion process.

3.1 Nuclear Magnetic Resonance (NMR)

NMR spectroscopy allows to investigate nuclear spin energy levels. Every nucleus has an intrinsic angular momentum (Equation 3.1). Thus energy levels of the nuclear spins are intrinsically present in any element. The origin is the presence of spin within the respective nucleus, those the presence of nuclear μ_n as well as electron angular momentum **L**. [147–149] The angular momentum $\boldsymbol{L}$, from the magnetic nuclei, is proportional to the spin $\boldsymbol{I}$, where the proportionality constant is given by the Planck's constant h, with $\boldsymbol{L}$ and $\boldsymbol{I}$ being quantum mechanical operators. In more details, the eigenvalue of $\boldsymbol{I^2}$ is $I(I+1)$, with the spin quantum number I that can have is integer and half integer values. The absolute value of the spin angular momentum is defined as:

$$|\boldsymbol{L}| = \hbar\sqrt{I(I+1)} \quad . \tag{3.1}$$

Where I is the spin quantum number of the nuclear spin I, which is the result of the combination of the individual proton and neutron spins in the nucleus. To be able to use magnetic resonance spectroscopy there are some specific requirements: i) I has to have half-integer spin for odd mass number i.e. ^{1}H, ^{13}C, and ^{31}P are spin $-1/2$ nuclei with $I = 1/2$, ii) I is integer with an even mass number and odd proton numbers,^{2}H, ^{6}Li are spin -1 nuclei with $I = 1$. For the other immeasurable nuclei with spin 0 i.e. ^{12}C,^{16}0, an enrichment with measurable isotopes can be used i.e.^{13}C,^{17}O, etc. Just to avoid confusion spin quantum number and spin are often used interchangeably. In the following the basics will be discussed for the most common nucleus, ^{1}H. If needed the discussion will be extended to the ^{7}Li nuclei, that is the one which is investigated in this thesis. In the case of lithium, the ^{7}Li, with spin $-3/2$ nuclei and with $I = 3/2$ will be treated.

The external magnetic field is defined along the z-direction, hence the component in the direction of the applied field is:

$$|L_z| = I_z\hbar = m\hbar \quad . \tag{3.2}$$

The magnetic quantum number is I_z or *m*. A nucleus with spin I has *2I+1* eigenstates:

$$I_z \equiv m = -I, -I+1, ..., I-1, I \quad . \tag{3.3}$$

The angular momentum and thus the spin is proportional to the nuclear magnetic field μ of the respective nuclei. Once again, the intrinsic magnetic moment of nuclei is due to the fact that an atomic nuclei carries an electric charge. In nuclei with spin, rotation then creates a circular current which produces a magnetic moment $\boldsymbol{\mu}$. The nuclear moment μ then starts to precess in B (torque) in one of its eigenstates.

$$\boldsymbol{T} = \boldsymbol{\mu} \times \boldsymbol{B} \quad . \tag{3.4}$$

The energy of the torque motion of the nuclear spin in B is naturally proportional to B and L and depends on the type of nuclei species which is defined by γ, the gyromagnetic ratio.

In the following and since the notations are following the reference from Ernst [147], the magnetic induction $\boldsymbol{B}$ will be used to characterize the magnetic field instead of the magnetic field strength $\boldsymbol{H}$. The total magnetization $\boldsymbol{M}$ is the sum of the magnetic dipole moments $\boldsymbol{\mu}$ per unit volume. The gyromagnetic (or magnetogyric) ratio γ, due to the rotation of the electrically charged particle, is fundamental for the magnetic resonance and is defined by

$$\boldsymbol{\mu} = \gamma \boldsymbol{L} \quad . \tag{3.5}$$

In order to address the nuclear spin states experimentally, the degeneracy of the eigenstates has to be lifted.

$$E = -\boldsymbol{\mu} \cdot \boldsymbol{B} \quad . \tag{3.6}$$

As mentioned above we need the z component of the nuclear magnetic moment

$$\mu_z = \gamma L_z = \gamma I_z \hbar \equiv \gamma m \hbar \quad . \tag{3.7}$$

The energy levels of a nucleus of nuclear spin *I* are thereby split under the influence of an external field in the z-direction $\boldsymbol{B_0}$. One obtains $2I + 1$, the so called Zeeman levels. The energy difference compared to the state without the magnetic field is:

$$E_m = -\mu_z B_0 - \gamma m \hbar B_0 \quad . \tag{3.8}$$

The interaction between the nuclear spin I and the external magnetic field B is given by the Zeeman interaction

$$\boldsymbol{H_Z} = -\hbar \gamma \boldsymbol{I_z} B_0 \quad . \tag{3.9}$$

Here γ_I is the gyromagnetic ratio of the nucleus I, $\hbar$ is the reduced Planck constant h divided by 2π and B_0 is the static magnetic field along the z-direction. The z index is used to indicate the direction of the magnetic field. For the sake of simplicity but without loss of generality, this index is sometimes omitted in the description, however most of the time it is implicitly included. The splitting of the energy levels is then a consequence of the interaction of the magnetic moments with the applied magnetic field. Those energy levels E_m are described as the eigenvalues of the Hamiltonian operator, where m is the *magnetic quantum number*. The magnetic quantum number can have integer values between $-I$ and $+I$. By this the nuclear spin with a quantum number can assume one of $2I + 1$ stable positions in the magnetic field, creating an energy splitting. The simplest case is the nucleus with $I = 1/2$ which will give rise to two eigenstates, one with spin up and one spin down orientation. Depending on the z-component of the magnetic moment, these orientations are either parallel or antiparallel to the magnetic field. A simple sketch for this situation can be seen in Figure 3.1.

In the case of ^{7}Li, the $I = 3/2$ will give rise to four eigenstates. In presence of an magnetic field, this will result in four different energy levels (Figure 3.1). In general, NMR is probing the nuclear spin states by inducing transitions between the different spin states and measuring the energy difference ΔE. The energy difference for transitions between different spin states (absorption, emission), if it reorients and moves from one energy level to the next, will determine the NMR frequency μ_0

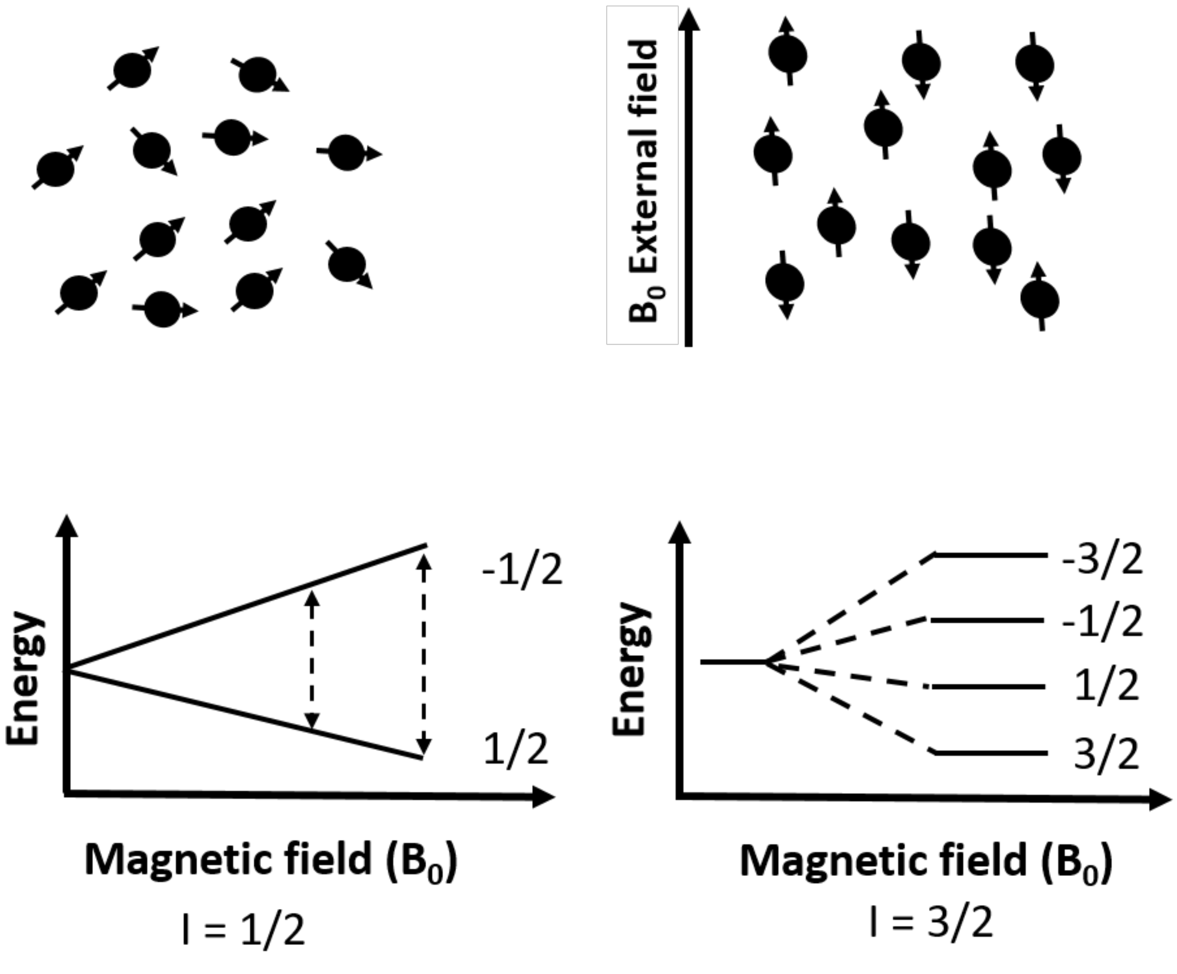
B_0 External field
Energy
-1/2
1/2
Magnetic field (B_0)
I = 1/2
Energy
-3/2
-1/2
1/2
3/2
Magnetic field (B_0)
I = 3/2

Figure 3.1 (Upper left) Free spins with random orientation. (Upper right) Reordering of the spins under the influence of an external magnetic field which is applied in z-direction (B_0). (Lower left) Zeeman splitting for a nucleus with spin-1/2. (Lower right) Zeeman splitting for a nucleus with spin-3/2.

$$\Delta E = |E_m - E_{m-1}| = \hbar\gamma B_0 = -\hbar\omega_0 = -\hbar\mu_0 \quad . \tag{3.10}$$

The above equation then defines the position of μ_0 of the Zeeman signal in the NMR spectrum.

After we know what the origin of the signal position in the spectrum is, we further need to define the role of its intensity. The polarization is the sum of all the components of the nuclear magnetic moments parallel to the applied field.

The thermodynamic equilibrium of all magnetic moments are found in one of the energy eigenstates E_m with having one of the $2I+1$ allowed projections along the z-axis. Thus the nuclear magnetic polarization is determined by the differences in population of the energy levels. The relative numbers n_{m-1}/n_m of the spin states are given by the Boltzmann distribution:

$$n_{m-1}/n_m = \exp(-\hbar\omega_0/k_B T) \quad . \tag{3.11}$$

Subsequently the population difference Δn = n_{m-1}-n_m can be calculated and one can identify how many spins are under investigation.

$$\Delta n = n_{m-1} - n_m \approx N_0\hbar\omega_0/(2k_B T) \quad . \tag{3.12}$$

In other words the NMR signal gives quantitative information about the number of spins. This can be exploited in an NMR experiment. In a simple ^{1}H experiment of ethanol (CH_3CH_2OH) the integrals of the obtained signals have the ratio of 3:2:1. Note that the ^{1}H on CH_3 are chemically equivalent. This also holds true for the ^{1}H nuclei on CH_2.

3.1.1 Influence of local chemical environment

In fact, the more complex the nuclei, the more complexity will be present in the spectra. The equilibrium magnetization of the system $\boldsymbol{M_0}$ is given by the sum of the projection of all nuclear magnetic moments along the axis of the external magnetic field B_0. The macroscopic magnetization, which under the sole influence of an external field aligns itself in the same direction as M_0 that equals to $\chi_0 H_0$ and again equal to $\chi_0 B_0/\mu_0$. To describe the correlation between the magnetic moments of the spins and the static magnetic field B_0, the Zeeman interaction is necessary. In general, this will also depend on the angle θ between this natural dipole moment and the field.

The energy can be described as

$$E = -MB_0 = -|\boldsymbol{M}||\boldsymbol{B_0}|\cos\theta = M_z B_0 \quad . \tag{3.13}$$

The orientation of the field $\boldsymbol{B_0}$ will define the z-axis of the coordinate framework as reference. Here, $M_z = |\boldsymbol{M}| cos\theta$ is the projection of the magnetization vector onto the direction of the magnetic field.

The intensity of the NMR signal (the area integral) depends on Δn or subsequently N_0m. As previously mentioned, this makes NMR a method which also gives us information on the relative number of spins under investigation. Additionally, the NMR signal provides qualitative information about the elemental species of the nucleus and quantitative information about the relative concentration of the nuclei. Nuclei of the same element will however resonate at different frequencies as a function of the magnetic field. Additionally, the local magnetic field experienced by a nucleus is slightly different from that of other similar nuclei due to the local magnetic field that each element/isotope i.e Li experience. If a molecule, which contains the nucleus of interest, is put in a magnetic field B_0, simple electromagnetic theory indicates that the B_0 field induces electron currents in the electron density of the molecule in the plane perpendicular to the applied magnetic field. These will then produce a small magnetic field opposed to the applied field that acts to partially cancel the applied field, thus shielding the nucleus. In general the induced opposing field

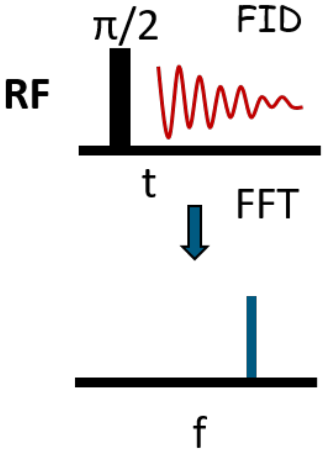

Figure 3.2 Illustration of the simplest pulse-acquire experiment and the conversion into the spectrum. The $\pi/2$ pulse is applied by a radio frequency (RF) signal. The pulse rotates rotates the magnetization through $\pi/2$. The signal is detected in form of the so called free induction decay (FID). The FID is the result of loosing spin polarization over the time. Here, the loss of spin polarization follows an exponential decay. The transformation of from time domain (t) (the FID) into frequency domain (f, or the spectrum) is achieved by the Fast Fourier transform (FFT).

is about a million times smaller than the applied field. Consequently, the magnetic field perceived by the nucleus will be slightly altered from the applied field so the resonance condition will need to be modified.

$$\nu = \gamma/2\pi B_{local} = \gamma B_0/2\pi(1-\sigma) \quad . \tag{3.14}$$

Here, sigma is a non dimensional screening or shielding constant. The frequency clearly depends on the shielding which reflects the electronic environment of the nucleus. Although we cannot easily determine absolute radio frequencies to an accuracy of ±1 Hz, we can determine the relative positions of two signals in the NMR spectrum with even greater accuracy. Consequently, a reference signal is chosen, and the difference between the position of the signal of interest and that of the reference is termed the chemical shift:

$$\delta = \frac{\nu_{ref} - \nu_{sample}}{(\nu_{sample} * 10^6)} \quad . \tag{3.15}$$

or

$$\delta = \frac{(\nu_{observed} - \nu_{reference})}{\nu_{spectrometer}} \quad . \tag{3.16}$$

3.1.2 Solid State NMR

Classical NMR developed into a well-established standard tool for probing virtually any closed-shell molecule. ESR provides a similar method for open-shell systems such as radicals. However, the solid state NMR brings still challenges and even more on an electron conductive solid. Since in a condensed matter environment each nucleus feels the influence of the other nuclei, this will modify the local magnetic field. Additionally, they are exposed to electric fields gradients and to the coupling of the surroundings or the lattice. That raises a complication, since each coupling separately, similar to the external magnetic field B_0, will affect a specific shift of the energy levels. The observable being the differences between the energy levels, they will be given by the eigenvalues of total Hamiltonian operator H_{NMRtotal}. The total Hamiltonian that governs the analysis involves a solid sum of different Hamiltonians is:

$$H_{NMR_{total}} = H_Z + H_Q + H_C + H_{RF} + H_{CSA} + H_J \quad . \tag{3.17}$$

where H_Z is the Zeeman effect or Zeeman interaction, H_Q quadrupolar moment, H_C dipolar interaction between nuclei, H_{RF} radio frequency effect, H_{CSA} chemical shift anisotropy and H_J coupling constant where $||H_Z|| > ||H_Q|| > ||H_C|| > ||H_{CSA}||$. [150] The magnetic shielding interaction H_σ is also referred to as chemical shift δ and provides unique information about the chemical environment in most of the cases. In metallic samples, this can be more complicated and less specific. The determination of the H_σ is then the aim in the solid-state NMR spectroscopy from the standard static spectrum. The Zeeman NMR signal discussed above does not provide information on the different environments on nuclei of the same kind. So only this interaction is not practically useful for the application, but describes the basic concept of NMR and is of fundamental importance in terms of absolute standard for theoretical calculations of the magnetic shielding. [151] The chemical shift is the prime observable in NMR experiments. The second important source of information from an NMR spectrum, i.e., nuclear spin-spin coupling effects is related to the interaction of a spin at one nucleus with the electronic currents brought about by a second magnetic nucleus., i.e., the interaction of two nuclear magnetic moments mediated by the electronic spin density. On the other hand if it is not a nuclear spin, but the spin of an unpaired electron that interacts with the magnetic field induced currents we enter the domain of electron spin resonance (ESR, also known as electron paramagnetic resonance, EPR). Here, the main observable is the so-called *g - tensor*, which resembles the NMR chemical shifts as it describes differences in the interaction due to the chemical environment and the hyperfine coupling constants which probe the amount of unpaired spin density at the nuclear position.

3.2 Dynamics in NMR

NMR spectroscopy is widely used to determine atomistic structure, atomistic/ionic order and mobility. The time scale accessible by NMR is limited by the actual hardware and the pulse that is applied to excite the nuclei. Regarding the intrinsic limit of the material, which is on one end limited by the fast motional cutoff of the spectral densities for unrestricted segmental motion and on the other end by the length of the spin-lattice relaxation time. The molecular dynamics, up to now, can be investigated within a range of $10^{-12}\ s$ to some 100 s. High resolution NMR is often used to analyse fast molecular motion. For the slow molecular motion the so call wide-line NMR is used. Wide-line spectra can provide detailed information about the type and the time scale of a slow molecular motion. However, due to the angular dependence of the resonance frequency the information is restricted to re-orientational processes. Molecular translation can not yet be sensed by NMR on molecular distance scale, but on a larger scale in the range of 0.1 μ up to about 10 μ by measuring atomistic diffusion in magnetic field gradients. [149] Nevertheless, dynamical processes that take place on or below the time scale of the NMR measurement will influence the recorded spectrum and are thus observable.

Molecular motions appear incoherent and are described by a stochastic process $n(t)$. One important quantity to characterize stationary stochastic processes is the auto-correlation function $a(\sigma)$,

$$a(\sigma) = \lim_{T \to \inf} \frac{1}{2T} \iint_t T n(t) n(t - \sigma) dt \propto \exp(-\sigma/\tau_c) \quad . \tag{3.18}$$

In many cases the auto-correlation function is an exponential function with a time constant τ_c, which is called the *correlation time* of the process. In polymer materials one often obtains distributions of correlation times for molecular motions. Such a distribution can be interpreted in two ways. Either different atoms that exhibit different correlation times during the time of observation (heterogeneous distribution) or a single atom exhibits different correlation times in different observation intervals (homogeneous distribution).

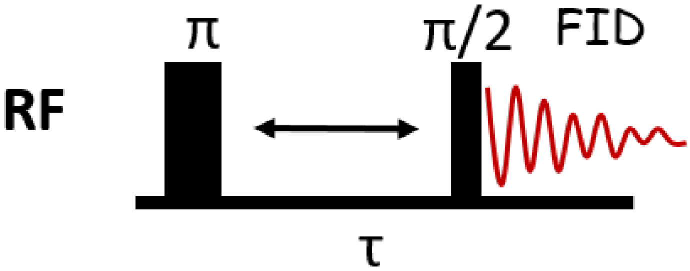

Figure 3.3 The pulse sequence for the classical inversion recovery experiment to measure T_1 or longitudinal relaxation.

3.2.1 T$_1$ and T$_2$

After being perturbed, the spins tend to restore the initial state of the thermodynamic equilibrium through a process called relaxation. They are two elementary kinds of relaxation that identify in the NMR world two different times the so called T_1 and T_2. [147] Energy relaxation or spin-lattice relaxation or longitudinal relaxation is known as T_1. It characterizes the time needed to establish longitudinal thermodynamic equilibrium magnetization after the sample was perturbed. To describe this, the energy should exchange between the nuclear spin and the lattice according to:

$$M_z(t) = M_0 + (M_z(0) - M_0)\exp(-\frac{t}{T_1}) \tag{3.19}$$

where $M_z(t)$ is solution or the differential equation of a magnetic system in contact with its environment. Here, one assumes a first order kinetic for its thermal equilibration. T_1 is related then to the longitudinal relaxation of the spins and corresponds to an exponential decay with this characteristic time constant. In a T_1 measurement, the recovery of the z-magnetization after an initial perturbation is measured as a function of time. The perturbation can be selective or non-selective. To get a full characterization one would need to perform different selective perturbations. To address that, saturation recovery methods are used. The recovery is analogous to the inversion recovery except for a loss of a factor two in dynamics range:

$$M_x(\tau) = M_0[1 - \exp -\frac{\tau}{T_1}]\sin(\beta) \tag{3.20}$$

Normally, the relaxation time T_1 can be determined by a two- or three-parameter fit. However, that can hinder other contributions to the relaxation time. This is one of the reasons one also has to apply and proceed with more advanced data analysis, such as Inversion Laplace transformation (ILT). [152, 153]

Another important contribution is the transverse relaxation time T_2 . This is as a consequence of non vanishing relaxation from the transverse components:

$$M_x(t) = M_x(0)\cos(\omega_0 t)\exp(-\frac{t}{T_2}) \tag{3.21}$$

$$M_y(t) = M_x(0)\sin(\omega_0 t)\exp(-\frac{t}{T_2}) \tag{3.22}$$

T_2 can be extracted as well from the classical spectra by measuring the full line-width at half height in units of Hz.

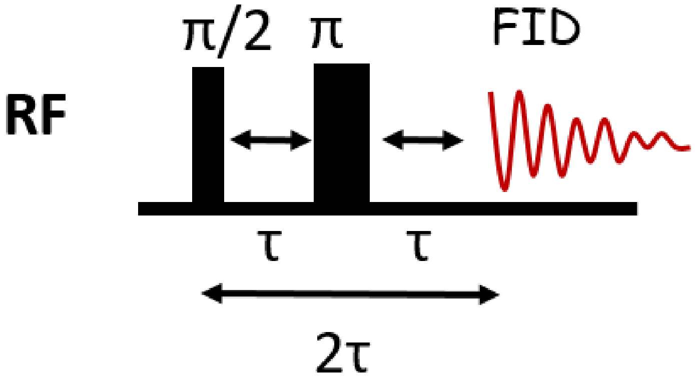

Figure 3.4 The pulse sequence for the spin alignment echo experiment.

$$\Delta\mu = \frac{\Delta\omega}{2\pi} = \frac{1}{\pi T_2^*} = \frac{1}{\pi}[\frac{1}{T_2} + \frac{1}{T_2^+}] \quad . \tag{3.23}$$

The effective decay rate $1/T_2^*$ is the sum of the natural relaxation rate $1/T_2$ and the inhomogeneous broadening contribution $1/T_2^+$. If the latter is negligible or can be measured from a reference line that is known to have a negligible homogeneous line-width contribution $1/T_2$, the natural T_2 can be obtained. Relaxation theory is describing the processes for achieving relaxations. Here, the rotational and translational molecular motions will lead to the fluctuation of the local field at the sites of the nuclei, and the origin is directly present in the spin interaction part of the material. This is also the one that allows us to be able to perform a stimulated-echo experiment. Crucial aspects that play an important role and need to be mentioned are the dipole-dipole interaction, the quadrupole interaction and the anisotropy of the chemical shift. All those can happen at different time scales, hence the importance of analyzing the relaxation times. The molecular motions are defined mainly by the resonance frequency, zero frequency and twice the resonance frequency, but can also be correlated to the amplitude of an applied rf field, the rotation frequency in magic angle spinning experiments or the cycle time in multi pulse experiments. In general a condition exists whereby transitions induced by H, which tend to upset the thermal equilibrium of spins, are in competition with processes of emission due to lattice perturbations which tend to restore equilibrium. Spin relaxation phenomena which are measured in terms of the relaxation times T_2 and T_1 (spin-lattice), must be distinguished simultaneously from effects due to the influence of the rf absorption. Consequently the study of resonance absorption line shapes, intensities and transients must carefully take into account the intensity of ^{1}H and the manner in which resonance is obtained. In practice, resonance takes place over a range of frequencies determined by the inhomogeneity throughout the sample. For resonance concerning nuclei in liquids it is generally found that the natural line width given by $1/T_2$ on a frequency scale is much narrower than the spread in Larmor frequencies caused by external field inhomogeneities, whereas the opposite is true in solids. Therefore steady state resonance lines due to nuclei in liquids are artificially broadened: transient signals are modified in shape and have decay times which are shorter than if they would otherwise be determined by T_1 and T_2.

There are several ways to address diffusion within the field of NMR. One of the most used for molecular transport and diffusion is the NMR pulsed magnetic field gradient (PFG). It has been developed over time together with the strength of the gradients and allows us to measure self diffusion and apparent diffusion coefficients more and more accurately. [154–156] The PFG allows to measure either the true diffusion coefficient, i.e. the isotope under observation has the same mass as the atoms of the crystal, like the ^{7}Li in pure ^{7}Li metal, or impurity diffusion where the solute species such as ^{7}Li diffuses in a ^6Li matrix. This leads to the diffusion coefficients in a simple and straightforward way without any *a priori* knowledge of the diffusion mechanism. However, often PFG gives still a diffusion coefficient that is defined via Fick's first law (see Section 2.4) and hard to disentangle from the self-diffusion. Furthermore, the non trivial extracted diffusion can be altered by the influence of the external field gradients especially in a conductive sample, where the formation of eddy currents can be a problem. [154, 156] Another set of techniques that allow us to determine macroscopic self-diffusion coefficients D^{SD} via NMR are exploit by NMR spin-lattice relaxation times, where the ^{7}Li relaxation [157–161] is investigated or even where possible, the β-NMR method relaxation [162]. The β-NMR method is studying the β-active ^8Li nuclei relaxation time, instead of the ^{7}Li nuclei. The signal for the ^8Li radioactive nucleus is detected through the β decay of a the respective isotope. [163]. The self-diffusion coefficient for isotropic diffusion is given by the modified Einstein equation:

$$D^{SD} = \frac{f < r^2 >}{6\tau} \quad . \tag{3.24}$$

Here, the f is the spatial correlation factor, $< r^2 >$ and $1/\tau$ are the mean square jump distance and jump rate of an Li ion, respectively. The spatial correlation factor f on top can be extracted by combining these with the D^{SD}. [63, 154] This equation is analogous to the one used by Langer *et al.* to extract activation barriers through correlation times, according to the jumps of the lithiums. In fact, if such a jump consists of an exchange jump of a Li ion with an adjacent monovacancy, they have $1/\tau = c_v(1/\tau_v)$, with c_v and $1/\tau_v$ where the concentration and hopping rate can be determined for those. [63]

3.2.2 Spin Alignment Echo

Ionic motions in the ultra-slow time-scale with jump rates in the kHz and sub-Hz are hardly accessible by recording line shapes or spin-spin relaxation times, as the ultraslow motions do not or only marginally affect the line shape as explained above. Ultra-slow Li hopping processes could be detected directly via a stimulated echo technique in a time range up to four orders of magnitude. [150] In fact, solid state echo NMR spectra allow us to study dynamics for the nuclei with $I \geq 1$. In solids the diffusion, chemical exchange and chemical reaction rates can be investigated in fact through the generation of the quadrupolar stimulated echo interaction. The SAE-NMR spectroscopy was developed first for deuterons and probes diffusion by labelling the ions via their quadrupole frequency. This is the relevant part which is used within the context of the lithium mobility, to investigate the interaction between the nuclear quadrupole moment and a non-vanishing electric field gradient (EFG) at the nuclei.

$$H_Q = \frac{e^2qQ}{4I(2I-1)\hbar}(3I_z^2 - I(I+1)) + \frac{\eta}{2}(I_+^2 + (I_-^2) \quad . \tag{3.25}$$

Here Q represents the quadrupole moment and when multiplied by e that is the elementary charge is commonly known as electric quadrupole moment of the nucleus "eQ". η is the electric field gradient (EFG) asymmetry parameter. To make it simpler, the quadrupolar interaction is described by the quadrupolar coupling constant C_Q $[Hz]$ and the quadrupolar frequency ω_Q $[rad/s]$. That helps in rewriting the 3.25 as

$$H_Q = \frac{\omega_Q}{6}(3I_z^2 - I(I+1)) + \frac{\eta}{2}(I_+^2 + (I_-^2) \quad . \tag{3.26}$$

where $\omega_Q = \frac{3e^2qQ}{2I(2I-1)\hbar} = \frac{3(2\pi)C_Q}{2I(2I-1)}$ with $C_Q = \frac{e^2qQ}{h}$.

The quadrupole interaction will alter then the Zeeman frequency ωL/2π according to $\omega_L \pm \omega_Q$. Hence, provided that electrically inequivalent sites are visited within a given diffusion pathway by the jumping ion, the information about the dynamic process is coded in terms of a change in the quadrupole frequency ω_Q. The SAE experiment monitors the quadrupolar frequency ω Q of the addressed nuclei before and after t_m. If the probed nucleus experiences a change in its quadrupolar frequency Q during t_m, the quadrupolar

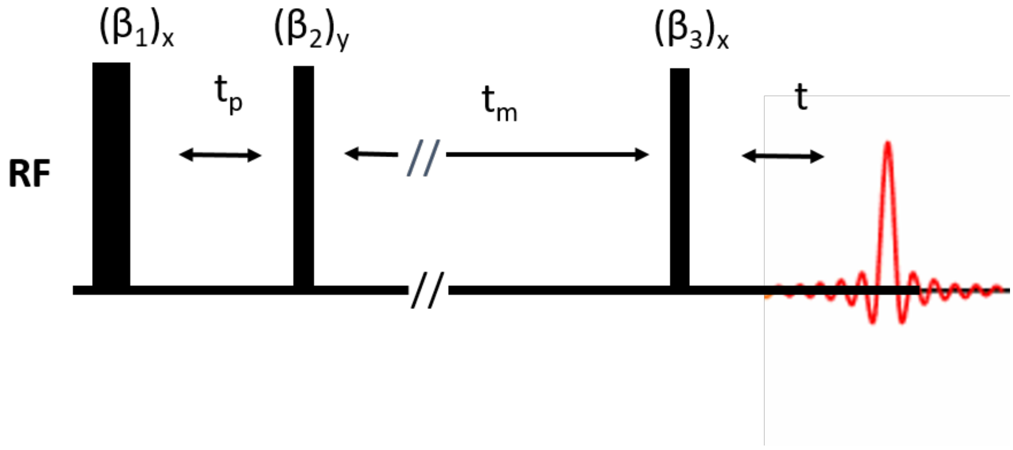

Figure 3.5 The pulse sequence of the SAE experiment. The SAE sequence generates quadrupole alignment within the first part of the sequence, that decays in the second part during the mixing time t_m. The remaining quardupolar order is transferred during the last pulse to the observable magnetization of coherence order and after a time t equal to t_p, an echo can be recorded.

alignment T_{20} is reduced and the echo at $t = t_p$ is diminished. A modification of Q is indicative for a change in the nuclear local environment, e.g. a jump of the nucleus to a site with a different electronic structure. Therefore, atomic or ionic motions can be investigated by scanning t_m and studying the decay of the echo at $t = t_p$ caused by nuclear jumps during t_m. The echo decay is defined by the correlation time t_c, which can be interpreted as the correlation time of the hopping process. The experimentally accessible time scale of dynamical processes by SAE is limited by experimental restrictions and the inverse of the quadrupolar interaction (lower bound 10^{-5} s) as well as by the quadrupolar spin lattice relaxation time T_1 (upper bound), which relaxes the quadrupolar coherence to longitudinal z magnetization T_{10} during t_m.

The investigation of the ionic motion through quadrupolar order interaction by stimulated echoes has its origin with the Jeener Broekaert sequence (JBS). The original JBS was conceived to create dipolar order and was used to detect its decay in different spin systems. [150, 164, 165] JBS can be used for different effective spins *i.e.* $I = 1$, [151], $I = 3/2$ [166].

In the experiment the signal amplitude generated by the JBS can decrease as a function of the mixing time either because i) the ultra-slow motional processes take place on a time scale τ_Q ($> 0.1ms$) which change ω_Q during t_m or ii) because the quadrupolar spin-alignment order can decay due to the spin-relaxation effects that occur on the scale set by Larmor frequency ω_Z. The decay constant of the latter process is usually called T_{1Q} and marks the long-time limit accessible in the ultra-slow motion regime. The relaxation of T_{1Q} to the spectral densities characterizing the motional processes is well known and it is of the same order of magnitude as the Zeeman spin-lattice relaxation time or T_1. [150] For mobile ions in crystals and glasses, the EFG at the probe site is dominated by the fixed charges in its environment. Under this condition the $S_2^Q(t_p, t_m, t)$ represents a single spin-spin correlation function. Nevertheless, $S^{Q_2}(t_p, t_m, t)$ and $S_2^D(t_p, t_m, t)$ are governed by closely related ionic motions, and the associated time constants τ_Q and τ_D may be expected to be quite similar as well. Ideally one should be able to distinguish these time constants, which have to be independent of the Larmor frequency, from T_{1Q} and T_{1D} which in slow-motion regime depend on the strength of the magnetic field. Generically dipolar and quadrupolar orders are created simultaneously by the JBS. Those contributions can however be separated by choosing a suitable evolution time t_p. JB is a sequnce of two rf pulses, out of phase by $\pi/2$ with one another and separated by a time of the order of T_2. It is possible to transfer Zeeman order into dipolar order by the use of a pair of phase-shifted rf pulses. [164]

SAE NMR uses the Jeener-Broekaert pulse sequence in $\beta_1 - t_p - \beta_2 - t_m - \beta_3 - t_d$. Here β represents radio frequency pulses, t_p is the evolution time, t_m the mixing time and t_d the detection transient. [164]

The result is an echo with an intensity relative to the correlation between the quadrupolar precession frequency ω_Q during the evolution time and during the detection transient at time t_m later. The Jenner-Broekaert echo is stimulated with three pulses 3.5. The second and the third pulse are each a 45°-pulse, whereby the phase of the second pulse is shifted against that of the first pulse by 90 °.

3.3 Inverse Laplace Transformation

To retrieve relaxation time constants from experimental spectroscopic data, different numerical methods are used, involving fitting procedures. Knowing *a priori* the number of relaxation processes, a mono- or multi-exponential decays the common least-squares fitting procedure can be used. Most of the time, however, the processes are not known, hence it is hard for the fitting procedure to disentangle the relaxations time constants with different components. To address this problem, inversion algorithms can be used, since they do not require making assumptions on the number of parameters. The inversion provides a density function of the underlying relaxation distribution. In fact, inversion algorithms are used as a better tool to analyze NMR data of complex systems [152, 167]. The drawbacks of this kind of algorithms is that the inversion can be ill-conditioned [152], and some *a priori* knowledge is still necessary. In this case, the number of processes is not required, whereas assumption that the data are smooth or can be made smooth *via* normalization is enough. A common method of regularization is the Tikhonov algorithm. [152, 167] To prevent oscillating solutions due to noise or different signs in the function, further constraints are applied, such as the so called non-negativity constraint (NNC). This assumes that all the relaxation components have a positive sign and the negative ones will be suppressed by the algorithm. Despite that, the inversion might show artificial features and the NNC does not guarantee the perfect fit. To overcome that, a uniform penalty (UP) was introduced and showed to be reliable in one-dimensional and n-dimensional data sets. Different implementations exists in particular to investigate and understand dynamics of complex systems, where a parameter such as time constant in the relaxation matrix can be linked to a different state of a system. [152]

In NMR, recording multidimensional relaxation or diffusion maps, in combination with two-dimensional (2D) ILT proved successful in recovering the relaxation maps from contribution that in a standard way were overlapping. The multidimensional experimental NMR data are related to an underlying joined distribution function such as Fredholm integral of the first kind:

$$s_r(t_1, ..., t_R) = \int_0^\infty ... \int_0^\infty k_1(t_1, \tau_1)...k_R(t_R, \tau_R) \times \mathcal{G}(\tau_1, ..., \tau_R) d\tau_1, ..., d\tau_R + \varepsilon(t_1, ..., t_R) \quad , \tag{3.27}$$

where, $s_R(t_1, ..., t_R)$ is the signal, with different evolution times, G is the underlying distribution function of $t_1, ..., t_R$ as variable. The kernels k_r are continuous functions and the following $\varepsilon(t_1, ..., t_R)$ are additive noise contribution assumed to be independent and identically distributed (iid) Gaussian white noise with zero mean and variance σ^2. [152]. The signal can be scaled without loss of generality by a factor σ^{-1} to obtain a unit variance. Non-iid noise can be accounted for by scaling the signal and the kernels with the inverse of the noise variance. [152] Solving the Fredholm integrals with smooth kernels, i.e., estimating $\mathcal{G}(\tau_1, ..., \tau_R)$ from $s_r(t_1, ..., t_R)$, is an ill-conditioned problem. However, to simplify the formulation a vector matrix notation can be used with the signal vector:

$$\boldsymbol{s} = \boldsymbol{K}\boldsymbol{g} + \boldsymbol{e} \quad , \tag{3.28}$$

where $\boldsymbol{s}$ is the vectorization of S_R, $\boldsymbol{g}$ the vectorization of G, $\boldsymbol{K}$ the kernel and $\boldsymbol{e}$ is the vectorization of the error matrix previously called noise.

A regularization has to be implemented with a penalty term to deal with the ill-condition problem, since a stable solution cannot be obtained directly by the inversion. The minimization of the function in the Equation 3.28 with the following penalty term can be written as

$$\hat{\boldsymbol{g}} = \operatorname{argmin} \left\{ \|\boldsymbol{K}\boldsymbol{g} - \boldsymbol{s}\|_2^2 + \lambda^2 \|\mathit{\Lambda}\boldsymbol{g}\|_2^2 \right\} \quad . \tag{3.29}$$

where $\mathit{\Lambda}$ is the regularization matrix and λ a global scaling factor. To avoid the non-negativity constraint, the algorithm was adapted to employ a uniform penalty regularization [152] to avoid oscillations or unnecessary sing changed of the relaxation time distribution. The functional that has to be minimized can be written as:

$$\hat{\boldsymbol{g}} = \operatorname{argmin} \left\{ \boldsymbol{g^T K^T g} - 2\boldsymbol{s^T K g} + \boldsymbol{s^T s} + \lambda^2 \boldsymbol{g^T} \mathit{\Lambda}^T \mathit{\Lambda} \boldsymbol{g} \right\} \quad . \tag{3.30}$$

To solve equation 3.30 the inversion algorithm uses Tikhonov regularization. For all details of the inversion and the parameter decision we refer to the implementation by Granwehr *et al.* [152]

This more advanced algorithm can be used to analyze and interpret T_1 and SAE data. [152,153,168,169] Applying the ILT to the experimental data yields a distribution of correlation times τ_c. Additionally, the ILT approach provides the NMR spectral information for each point in the τ_c distribution which also contains the ωq of the position where the jumping nucleus is originated from. The experimentally accessible time scale of dynamical processes by SAE is limited by upper and lower boundary to the intrinsic property or dynamics of the material. [152, 153, 168–170]

4 Revisiting the Storage Capacity Limit of Graphite Battery Anodes: Spontaneous Lithium Overintercalation at Ambient Pressure

This chapter is closely following the paper on arXiv.org(2021) (arXiv:2107.11137v2) which is Reprinted under the terms of Creative Commons Attribution 4.0 International License. The parts were just adapted to follow the structure of this thesis, however the format was kept the same. Cristina Grosu performed the measurements and Chiara Panosetti performed the DFT calculations. Peter Jakes and Steffen Merz contributed valuable discussions and advice concerning the spectra acquisitions and sample preparation. Data evaluation and the manuscript preparation was done by Cristina Grosu and Chiara Panosetti in consultation with all the authors. Sebastian Matera contributed to the discussion on the data analysis. Josef Granwehr and Christoph Scheurer designed the work.

4.1 Introduction

For a reduction in greenhouse gas emission to tackle global warming, mass market penetration of electric vehicles (EVs) is a key element for a nearly CO_2-free transportation sector [1]. Powerful, durable and safe lithium-ion batteries (LIBs) are crucial for consumer acceptance of electromobility on a larger scale. In particular, the fast-charging capability is regarded as a pivotal selling point. The necessity of fast-charging batteries brought some intrinsic limitations of the materials back into the spotlight, which historically did not matter in commonplace applications of LIBs, such as portable electronics. Primarily for the negative electrode, notable issues are still largely unaddressed to this day, including increasing the active site density, earlier detection of dendrite formation, or a quantitative description of mass and charge transport [3–6]. Extensive amount of work is ongoing to identify alternatives to the carbon-based anode materials. Even within the class of carbonaceous materials, different options were screened for usage as negative electrodes, from soft to hard carbon, carbon foam, carbon nanotubes, graphene sheets, artificial graphite, or mesocarbon microbeads graphite (MCMB) [15].

Nonetheless, with its intrinsic capacity and wide availability, graphite is still the most employed anode material. Its working principle is based on the intercalation of lithium ions. Upon lithium intercalation during charging, graphite reaches its maximum reversible Li storage capacity at a lithium-to-carbon ratio of 1:6 (LiC_6). Theoretically this compound yields a capacity of 372 mAh/g, commonly defining 100% state of charge (SOC) [14, 15, 40]. However, the highest geometrically accessible composition – not considering lithium carbide (Li_2C_2) but only the family of graphite intercalation compounds (GICs) – is not LiC_6, but LiC_2, with a capacity three times higher. Nevertheless, the latter is metastable at ambient conditions and its non-electrochemical preparation was only reported under high pressure, with superdense decomposition products, LiC_{6-x} with $x > 0$, stable over an extended time period [171, 172].

Despite extensive experimental efforts, in-depth understanding of *in operando* battery processes is still sparse [173–176]. One major problem is that the interconnection of many relevant electrochemical processes renders the analysis of experimental data difficult and complicates the understanding of actual limits and causes of battery cell failure [3]. Furthermore, theoretical investigations over large compositional Li/C ratios, and on time scales relevant for Li dynamics in graphite without unrealistic simplifications have only become possible recently. Therefore, concomitant theoretical and experimental research is scarce.

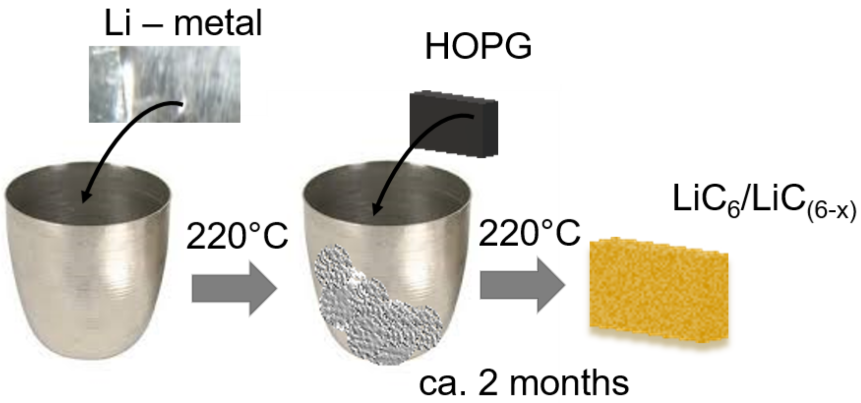

Figure 4.1 Schematic representation of the conducted synthesis. First, metallic lithium was melted and kept at 220 °C. Subsequently, a HOPG sample with dimensions of 10.0x(4.9)x2.0 mm was added. Tweezers were used to keep the HOPG in contact with molten lithium for a few minutes to start the intercalation. The system was then held for *ca.* ten weeks at constant conditions to ensure full intercalation into the HOPG.

Here, we use HOPG as a model system to investigate lithium ion intercalation, providing nuclear magnetic resonance (NMR) reference data from a system as well-defined as possible for further *in operando* studies of LIBs. To exclude any external influence on the intercalation process, we opted for an infiltration technique under ambient pressure [177–179]. Figure 4.1 shows a sketch of the synthesis workflow, using lithium metal and HOPG as precursors. More details on the preparation are provided in Section 4.4. Using this slow intercalation route, we obtained a sample that, repeatedly analysed in detail, showed spectroscopic evidence of superdense structures. We assessed the plausibility of such an assignment of spectral features by *ab initio* calculations. Eventually, we analysed the long-term evolution of the sample over several months, concluded by heating it up to 60 °C.

4.1.1 What do we know about superdense LiC_2 and LiC_{6-x}?

Superdense realisations of lithium GICs were reported at high pressure and temperature conditions since the 1980s [171, 180–186]. Figure 4.2 schematically shows possible high-symmetry structures for some intermediate stoichiometries between LiC_6 and LiC_2.

The occurrence of LiC_2 was excluded *a priori* from any working battery for a long time. Since its non-electrochemical synthesis was always performed at high pressure and temperature, it is considered unlikely to be found in secondary batteries [172, 181, 187]. Alternatively to high-pressure synthesis, ball-milling also allows LiC_2 to be prepared using artificial graphite, MCMB, and carbon foam [185, 187, 188]. However, one may argue that ball-milling produces high pressure and temperature locally [189]. Once the pressure is released, the LiC_2 composition becomes unstable and approaches $LiC_{2.2-2.7,3.4}$ [181, 190]. Nevertheless, $LiC_{2.7}$ and $LiC_{3.4}$ as decomposition products of LiC_2 were reported to be stable enough to allow measurements at ambient conditions [182, 183]. Bindra *et al.* stabilised superdense GICs using boron doping, in an attempt to enable higher capacity electrode materials, yet they still used high-pressure synthesis [182].

For electrochemical intercalation, Conard *et al.* reported that the electric field actuates only as far as the gallery entrance, and therefore is not sufficiently attractive to drive the intercalation up to LiC_2 [191]. Notwithstanding, superdense phases were observed for electrochemical systems using different carbon-based matrices, leading to the concept of overcharged LIBs [192–194]. In the latter works, lithium ions appeared to continue intercalating after LiC_6 was formally reached, yet before being plated as lithium metal. Unfortunately, such overcharged anodes show irreversible capacity loss after the first deinterca-

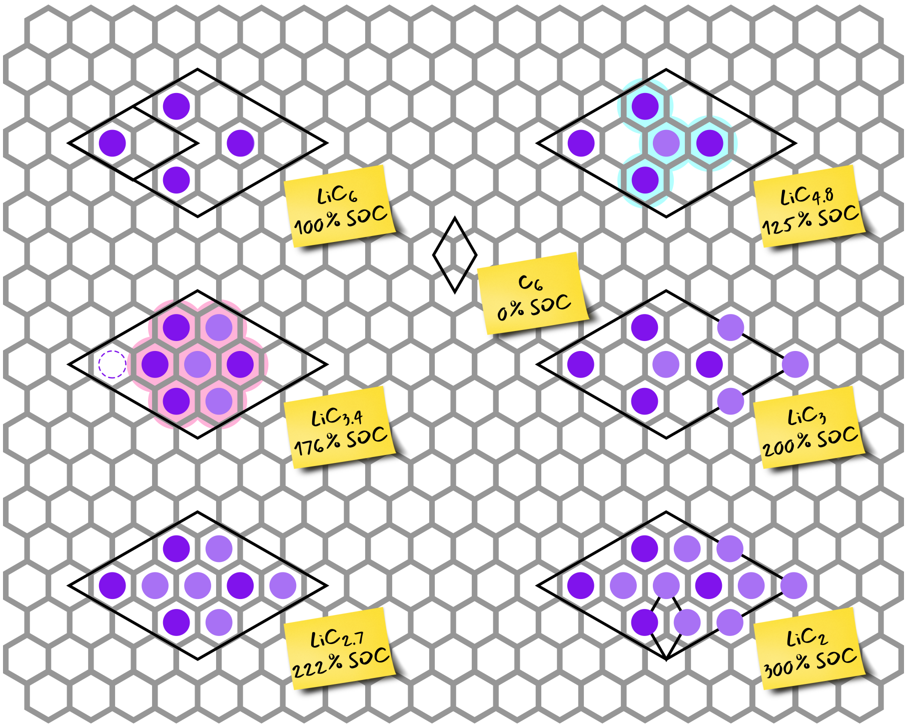

Figure 4.2 Schematic single-layer representation of some superdense LiC_{6-x} high-symmetry structures and respective states of charge (SOC) relative to LiC_6. The grey honeycomb represents the graphitic host lattice assumed to be AA stacked, and purple circles represent lithium atoms. Excess lithium with respect to LiC_6 is represented in lighter purple. The dotted circle in $LiC_{3.4}$ marks how at least one Li atom must move from its original position in order to achieve the Li_7 cluster motif. Black diamonds represent the smallest supercell commensurate to all the lithiated stoichiometries. For LiC_6 and LiC_2, the (smaller) primitive cell is also shown. Highlighted in red and cyan are structural motifs that can give rise to high-ppm NMR signals.

lation cycle [193]. More recently Paronyan *et al.* successfully used carbon foam as anode material to investigate overlithiation [195].

A systematic investigation of the relative stability of overlithiated compounds, especially the intermediate stoichiometries between LiC_6 and LiC_2, is currently missing, both from the experimental and the computational standpoint. On the experimental side, there is widespread consensus [196–199] that the free energy of intercalation of LiC_6 falls in the range of -6 to -14 kJ/mol (-0.06 to -0.14 eV). Yet little is known about the free energies of overintercalation, except that the formation of LiC_2 is assumed endergonic at ambient conditions. On the computational side, previous studies based on Density Functional Theory (DFT) only report total energy calculations of LiC_6 and – less often – LiC_2 [172, 200–202]. Two main limitations are recurring among these. First, dispersion interactions, which are crucial in intercalation chemistry, were not included in all the studies. Secondly, total energies only provide a “virtual” zero-temperature picture, while finite temperature and pressure require a description in terms of free energies. Despite these limitations, the reported total energies are compatible with the measured thermochemistry. However, no coherent body of literature exists that addresses the energetics of the entire LiC_{6-x} range on the same footing.

4.2 Materials and Methods

4.2.1 Experimental

Synthesis and Sample Preparation The LiC_6 sample was prepared using an infiltration technique. Metallic lithium with 99.9 % purity (Sigma-Aldrich) was intercalated into highly oriented pyrolytic graphite

HOPG (Goodfellow purchased by Sigma-Aldrich). The lithium metal was heated after the melting point up to 220 ° C. The lithium's self-cleaning properties ensure a higher purity of the molten lithium metal. Afterwards the HOPG was added. In order to ensure complete lithium intercalation, the intercalation process has been allowed to take place for a period of over 2 months. This long infiltration time was necessary due to the dimension of the host material (pre-intercalation size = $10.0 \times (4.9) \times 2.0$ mm) [177–179]. The ageing process was performed in a closed container in a glove box under argon atmosphere. The sample was left to age for 5 months initially, followed by an additional period of 2 months. For the 5 months aged sample, a series of temperature dependency spectra of ^{7}Li static NMR were recorded.

NMR Measurements and Data Analysis All ^{7}Li NMR spectra were acquired using a Bruker BioSpin spectrometer Avance IIITM HD 600 XWB MHx at B_0 = 14.1 T (^{7}Li Larmor frequency = 233.3 MHz) equipped with a Bruker DiffBB 5 mm BBO-H/F-Z Gradient diffusion probe-head. A single 90 ° pulse excitation of 11 μs with recovery delays of 10 s on ^{7}Li was employed. The raw data were analysed using MATLAB. An exponential window function was employed before a fast Fourier transform (FFT). The spectra were zero- and first-order phase corrected as well as background corrected.

4.2.2 Computational

DFT Calculations and *ab initio* Thermodynamics All the DFT calculations were performed using the plane-wave code `VASP` [203] v.5.4.4, with the GGA-PBE functional [100] and the Projector Augmented-Wave (PAW) pseudopotentials [204]. Dispersion interactions were taken into account with the D3 method [121]. To ensure well converged total energies, a basis-set cutoff of 599 eV was chosen. All the calculated geometries were represented in appropriate periodic supercells and the Brillouin zone was sampled at a fixed k-point density of 0.1 Å^{-1}. The vibrational densities of states were calculated using `phonopy` [205] at the harmonic approximation level. The chemical potential of lithium was mapped to the temperature in a 0-600 K range using Janaf thermochemical tables [206] up to the fusion temperature (453.69 K) and employing a linear approximation for higher temperatures as described in Section 4.5. AIMD simulations were performed by means of the DFTB [109] code `dftb+` [207] v.19.1 using the parametrisation developed in our group [112, 119]. Trajectories of variable length were propagated with a time step of 1 fs in the canonical ensemble at 500, 750 and 1000 K, using a Nosé-Hoover thermostat [208] with a coupling strength of 41 THz, corresponding to the highest vibrational mode of LiC_6 as calculated with `phonopy`.

4.3 Results and Discussion

4.3.1 Static ^{7}Li Nuclear Magnetic Resonance on Lithium intercalated HOPG

Static ^{7}Li NMR spectroscopy is a valuable tool to distinguish different degrees of lithiation in carbonaceous materials [173]. The ^{7}Li nucleus possesses spin 3/2, making observations of central transitions and quadrupolar satellite transitions possible. Satellite transitions allow conclusions on ordered structures with low Li-ion mobility [178, 191], whereas their absence may indicate a lack of perfectly ordered motifs and/or a motional averaging of the quadrupolar interaction [191].

Figure 4.3 shows a photograph of the fully intercalated HOPG sample. The golden colour is characteristic of LiC_6. However, overlithiated compounds were also reported to appear golden [182, 187]. Figure 4.3 represents the static ^{7}Li solid state NMR spectrum of the polished sample. All chemical shifts are reported against an external reference of a 1.0 M solution of LiCl in D_2O. We assign the isotropic chemical shift at 45 ppm with quadrupolar satellites to LiC_6, compatibly with previous works [63, 175, 209]. Additionally, an asymmetric signal with a sharp peak at 274 ppm and a shoulder at *ca.* 256 ppm is present. We also observe a broad spectral feature around 100-200 ppm, that is not background distortion (*cf.* Figure 4.8). At first, the high-ppm signals may be attributed to plated lithium on the sample. The HOPG surface was

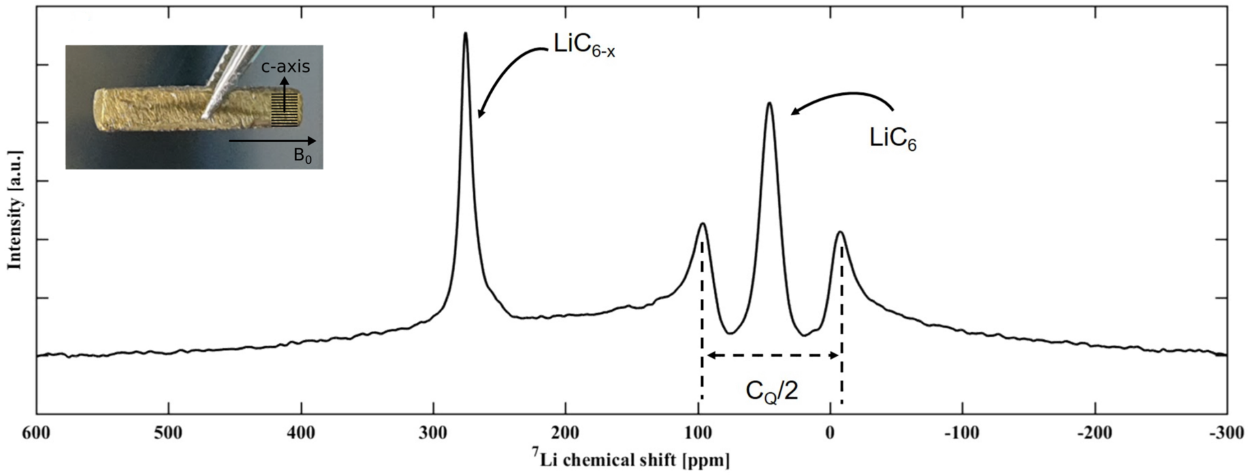

Figure 4.3 Static ^{7}Li NMR and initial sample in the NMR tube: Static ^{7}Li spectrum of lithium intercalated in HOPG. The isotropic chemical shift at 45 ppm is assigned to LiC_6. The quadrupolar satellites are compatible with a single-crystal pattern [178, 191]. The quadrupolar coupling constant C_Q for LiC_6 is 46 kHz. The peak at 274 ppm and the shoulder at 256 ppm show the presence of superdense LiC_{6-x} compositions [185]. Inserted figure shows the golden colour of lithium-intercalated HOPG, nominally corresponding to LiC_6 [14, 178]. Schematics in overlay show the orientation of the graphite layers, the crystallographic c-axis and the direction of B_0.

polished using sand paper (Figure 4.7), but residual metallic Li may persist. However, the intensity is too high for only trace amounts of lithium metal on the surface that are not detectable by visual inspection. Moreover, HOPG can be considered a defect-free single crystal, thus lacking internal pores that could accommodate pockets of metallic lithium [22].

At this point, we must consider the possibility that these high-ppm signatures are generated by superdense phases instead. We are aware that superdense Li-GICs were never reported before without harsh pressure conditions. However, the uncertainty raised in our sample reflects the ambiguity of assignments present in literature. Azaïs *et al.* assigned a 259 ppm ^{7}Li NMR resonance to lithium metal, despite using the exact ratio of Li/C to form LiC_2 with a ball-milling synthesis. Interestingly, they found no Li metal signal in the X-ray spectrum, which is explained by intensive milling applied to the sample [194]. Conversely, Conard *et al.* assigned a peak at 259 ppm to LiC_2 [171]. Since the spectrum was recorded after releasing the pressure, the true LiC_2 chemical shift might be closer to the Li metal shift. The 259 ppm peak could then be attributed to $LiC_{2.2-2.4}$ [171, 181, 190].

As shown in Figure 4.2, two local structural motifs are recurring in superdense compositions: a Li_4 pattern in the shape of a three-pronged “star” (highlighted in cyan) and a denser Li_7 pattern in the shape of a flat cluster, or “flower” (highlighted in red). The central Li atom is coordinated by three or six nearest Li neighbors, respectively. It is therefore expected to exhibit pseudo-metallic character. This was already suggested to explain the high-ppm signals associated to LiC_2 decomposition products [181, 187, 191].

Chang *et al.* showed that variable shifts at high-ppm can arise from different microstructures of lithium metal in electrochemical systems [210]. Since no current or potential was applied during sample preparation, the formation of dendrites or mossy-type microstructures is not expected here. Trease *et al.* showed that lithium metal in non-spherical shapes is also sensitive to the direction of the magnetic field, with resonances shifting between about 245 and 270 ppm if a planar sample is placed perpendicular or parallel to B_0, respectively [211]. This is known as orientation-dependent shift due to the bulk magnetic susceptibility effect. All our comparative measurements were performed using the same sample orientation, with the c-axis perpendicular to B_0 (Figure 4.3). In a control experiment, we also cut part of the sample to measure at parallel orientation. The high-ppm signature only moved to 264 ppm (Figure 4.8) within the limits set

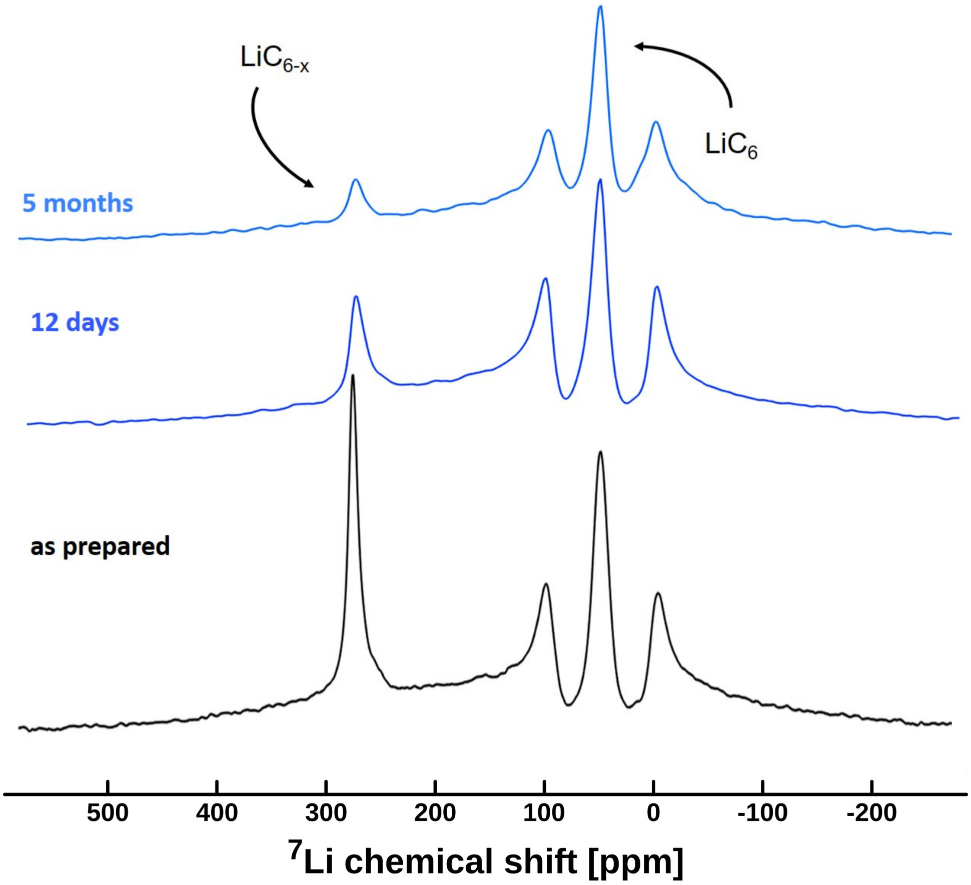

Figure 4.4 Evolution of the static ^{7}Li NMR spectrum during ageing of Li-intercalated HOPG. The black curve shows the spectrum recorded after preparation. The dark blue curve shows the spectrum of the same sample aged for twelve days and the light blue curve after aging of five months. The signal appearing at 10-13 ppm overlaps with the first quadrupole satellite peak of LiC_6 and appears more pronounced after five months compared to twelve days.

by the original 274 and 256 ppm signals. This indicates a susceptibility effect also for the quasi-metallic superdense species, as it has been observed for Li metal, before.

4.3.2 Calendar Ageing and Post-ageing Temperature dependent static ^{7}Li NMR of lithium intercalated HOPG

We aged the sample to investigate the long term (meta-)stability as well as changes in composition of LiC_{6-x} over time. In addition, more invasive temperature dependent NMR experiments were performed after five months, followed by another two months of ageing.

We recorded static ^{7}Li NMR spectra after twelve days (dark blue curve in Figure 4.4) and after five months (light blue curve Figure 4.4). The sample was thoroughly cleaned before each measurement, exposing golden shiny faces on each side of the HOPG crystal. We observe a decrease in the high-ppm peak intensities, suggesting a partial degradation of the corresponding structures. The degradation process appeared incomplete, with a residual broad signal that appears as the overlap of both shifts present in the fresh sample spectrum. The stability of the structures associated with these signals over several months is compatible with Nalimova *et al.* [181]. The 274 ppm signal seems to decrease the most during this timeframe but cannot be fully disentangled from the 256 ppm (light blue *vs.* black curve Figure 4.4) A new Li environment with a chemical shift of 10–13 ppm forms concomitantly. Signatures in

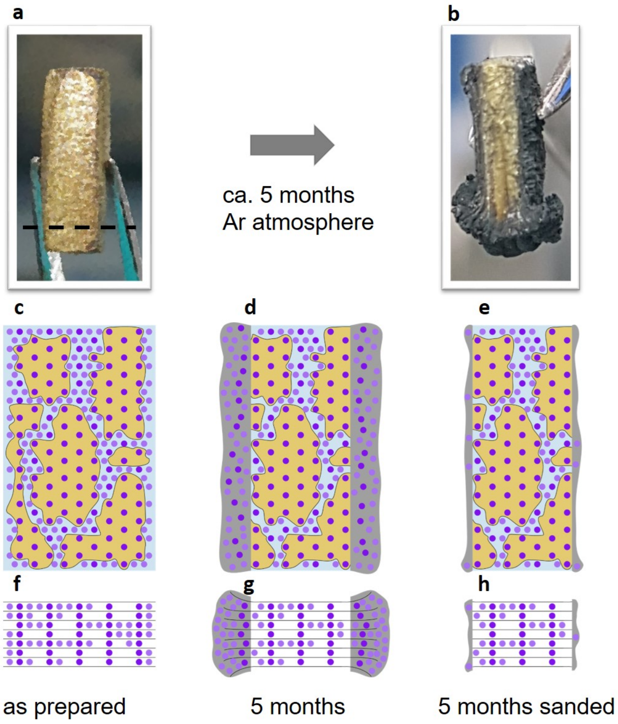

Figure 4.5 Representation of the sample: a, Image of Li intercalated in HOPG after polishing. The golden colour indicates LiC_6 or LiC_{6-x} compounds. The dashed black line indicates the cut for complementary measurement (*cf.* Figure 4.9). The golden face is shown after partially cleaning the sample. b, The sample after *ca.* five months of calendar aging in an inert atmosphere. The delamination shows the partial decomposition of the superdense compound. (c-h), Schematic cuts through the overlithiated HOPG sample. Horizontal black lines in (f-h) represent graphene layers, and violet dots are Li nuclei. Golden shaded regions represent well-ordered LiC_6 domains, giving rise to the 45 ppm NMR signal with quadrupolar satellites (*cf.* Figure 4.3). The lower intensity of the satellites compared to the central transition indicates the presence of such ordered domains with limited dimensions, not spanning the whole HOPG sample. The blue interdomain region is overlithiated. Note that the dimensions are not drawn to scale – the intensity of the satellites indicates LiC_6 domains with a fairly large ratio of Li nuclei on the surface to Li in the volume of a domain of about 1:1. Upon aging, the surface of the lithiated HOPG crystal delaminates (grey shading), with disordered carbon forming that pulls Li from disordered regions, yet maintaining the LiC_6 domains and the overlithiated interdomain region. Sanding only affects the surface, leaving the inner regions unchanged.

this region are commonly associated to lower SOC and generically identified as LiC_{6+x} [175], or, in other works, attributed to Li–Li dimers [41].

After five months the sample decomposed visibly as shown in Figure 4.5. The observed drastic delamination is only compatible with the expulsion of lithium from inside the sample, thus it would not have occurred if the high-ppm signal was caused by surface metal only. The opening of the graphite sheets also indicates pressure release from within the bulk material [181, 187, 190]. This is a further indicator towards the degradation of a superdense structure. Figure 4.5 also shows a schematic model of the possible microscopic configuration of sample (Panels a, f), with ordered LiC_6 domains and overlithiated interdomain regions. Panels d, g show the schematic delamination after five months. Panels e, h represent the sample after cleaning.

In the temperature dependent measurements (Figure 4.6 and Figure 4.9), the residual high-ppm peak disappears after mild heating to 310–330 K, while the 10–13 ppm signal becomes more evident (*cf.* Figure 4.9). The broad spectral feature between about 100–200 ppm, which temporarily vanishes at elevated temperature during the heating cycle (*cf.* Figure 4.9 at 40 and 60℃), reappears post-heating and only vanishes permanently after two more months of ageing.

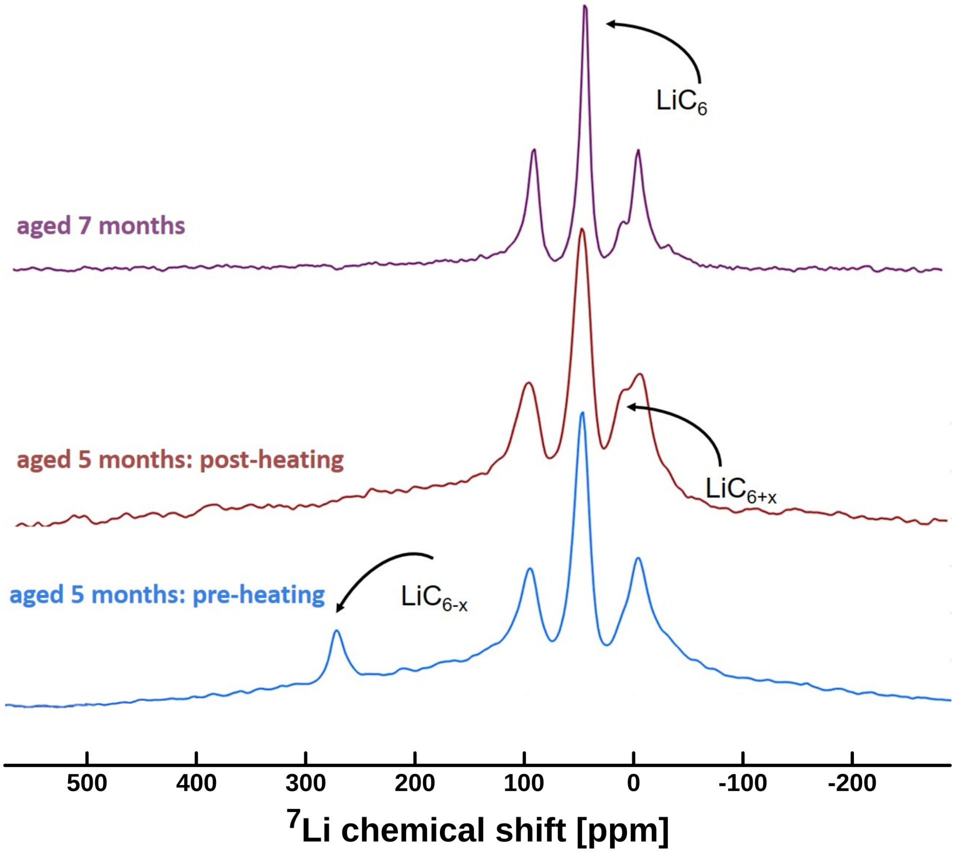

Figure 4.6 Static ^{7}Li NMR spectra taken after the decomposition process and pre- and post-heating to accelerate the equilibration of the residual superdense phases. All curves are shown for 25 °C, while the sample was treated and measured from -10 °C to 60 °C (*cf.* Figure 4.4). The violet curve shows the sample aged for two additional months. The peak at 10-13 ppm remains stable.

4.3.3 Ab initio Thermodynamics and Dynamics of superdense GICs

A basic modelling approach is to initially consider periodic high-symmetry structures as shown in Figure 4.2, and calculate the formation free energies of these extended "pure" phases. To this end, we adopted an *ab initio* thermodynamics (AITD) approach [212]. A detailed derivation of the formalism adapted to our system is provided in Section 4.5. Within this framework we calculated the free energy of intercalation $\Delta G^{\mathrm{interc}}$ for the stoichiometries above at 300 and 500 K and ambient pressure. Based on these, we estimate relative populations $N(\mathrm{LiC}_{6-x})/N(\mathrm{LiC}_6)$ at equilibrium as Boltzmann ratios with respect to LiC_6. The results are reported in Table 4.1. The effect of configurational entropy was neglected, which would further favour overlithiated compounds (except LiC_2; see Section 4.5 *Ab initio thermodynamics*). As such, the relative populations are to be considered a lower estimate.

With a ΔG^{interc} of +1.09 eV for LiC_2(105.17 kJ/mol) at 500 K, we exclude its presence in the sample. However, $LiC_{3.4}$ and $LiC_{4.8}$ have only mildly positive $\Delta G^{\mathrm{interc}}$ at 500 K, which becomes even negative at room temperature for $LiC_{4.8}$. Correspondingly, their relative populations are non-vanishing. Regardless of the precise assignment of the high-ppm signal (*vide infra*), we stress at this point that the energetics above, albeit simplified, confirm that a certain amount of excess lithium does indeed enter spontaneously. In other words, the common conception that LiC_6 corresponds to 100 % SOC is not entirely accurate thermodynamically. The exact upper limit of overlithiation accessible beyond LiC_6 and its dependence on external conditions can only be determined by means of computationally expensive statistical sampling, which goes beyond the scope of this work.

Table 4.1 Formation energies of selected LiC_{6-x} intercalation compounds. ΔE is calculated from DFT total energies (*cf.* Methods section), not including the zero point energies nor any finite temperature contribution. The values of ΔG at different temperatures and ambient pressure are calculated using the *ab initio* thermodynamics approach. Our experimental conditions are T = 500 K and P = 1 atm. In bold, non-negligible populations at 300 and 500 K.

	LiC_6	$\text{LiC}_{4.8}$	$\text{LiC}_{3.4}$	LiC_3	$\text{LiC}_{2.7}$	LiC_2
ΔE^{interc} (DFT-D3) / eV	-0.10	-0.01	0.14	0.27	0.46	1.08
ΔG^{interc} (300 K) / eV	-0.12	-0.03	0.09	0.24	0.40	1.00
ΔG^{interc} (500 K) / eV	-0.09	0.02	0.12	0.28	0.44	1.09
$N(\text{LiC}_{6-x})/N(\text{LiC}_6)$ (300 K) / eV		**0.03**	0.00	0.00	0.00	0.00
$N(\text{LiC}_{6-x})/N(\text{LiC}_6)$ (500 K) / eV		**0.08**	**0.01**	0.00	0.00	0.00

The observed high-ppm signal may indeed arise from Li_7 "flowers" and/or Li_4 "stars" present not only in sizeable domains of exact $\text{LiC}_{3.4}$ and $\text{LiC}_{4.8}$ compositions, but also diluted in a LiC_6 environment. Considering that, starting from a LiC_6 environment, every additional lithium will form at least a Li_4 "star", this can happen at any LiC_{6-x} stoichiometry. Additionally, a "flower" may form if three neighbouring Li atoms from the immediate surroundings aggregate around the centre of a "star". We estimate the cost of such aggregation as *ca.* 0.11 eV, thus also thermally accessible. Subsequently, "star" and "flower" motifs are in equilibrium with each other, thus both can contribute to the high-ppm signals.

The relative populations at 300 K (*cf.* Table 4.1) confirm the metastability of superdense patterns at room temperature. However, the relative concentrations of these patterns in the fresh sample must be closer to those at 500 K than those at 300 K, as the calendaric aging showed a slow equilibration towards degradation.

Assuming that the decomposition is diffusion-controlled, we estimate the effective diffusion barrier and thus the relative degradation rate at 300 *vs.* 500 K. We performed *ab initio* molecular dynamics (AIMD) simulations, based on Density Functional Tight Binding (DFTB) [109], to evaluate Li mobility in a slightly oversaturated LiC_{6-x} supercell with two Li_7 motifs in an LiC_6-like environment. The resulting diffusion coefficients (Figure 4.10) show Arrhenius behaviour with an effective barrier of 0.35 eV, which slows down the delithiation about 225 times at room temperature compared to 500 K (*cf.* Ab initio Molecular Dynamics) 4.6.

We note in passing that the AIMD trajectories exhibited frequent occurrences of directly connected Li dimers and trimers in an isosceles triangular configuration as transient byproducts of the decomposition of the Li_7 clusters (Figure 4.11). This nicely ties in with the appearance of the low-ppm shoulder upon ageing, if this were to be attributed to Li–Li dimers rather than low-SOC patterns.

4.3.4 Discussion

Without explicitly simulating chemical shifts, we cannot unambiguously assign each resonance. We excluded that the high ppm features are generated by lithium metal. On energetic grounds, we also exclude full LiC_2. Thus, we infer the presence of some form of intermediately overlithiated phase containing Li_7 ("flowers") and/or Li_4 ("star") motifs, and associate the high-ppm shift to pseudo-metallic character of the central atoms. While one may argue whether the Li_4 stars are "dense" enough to produce high-ppm shifts, their formation is more energetically accessible than that of Li_7 flowers, therefore a spectroscopic signature is to be expected. In the light of this, we put forward the following scenario, qualitatively combining experimental observations and simulations. The asymmetric high-ppm signal corresponds to sizeable domains of at least $LiC_{4.8}$ stoichiometry, possibly mixed with $LiC_{3.4}$, and domains of variable $LiC_{x>3.4}$ stoichiometries with Li_7 and/or Li_4 motifs diluted in LiC_6-like surroundings.

The signal is split into a sharp 274 ppm feature and a broad 256 feature due to susceptibility effects analogously to metallic lithium, but of smaller magnitude. As such, the more intense 274 ppm peak would correspond to sample faces with normal vectors perpendicular to B_0, while the 256 ppm corresponds to face normals parallel to B_0. It is reasonable to assume that overlithiation mainly occurs in the proximity of the HOPG surface, while the inner bulk is predominantly LiC_6. Then, the relative magnitude of the two peaks reflects the dimensions of the sample (longer surface along B_0). Moreover, as the core of the sample may be shielded to a fair degree, surface species may be weighted more strongly and therefore show a higher relative amplitude with respect to the LiC_6 bulk than relative energetics would suggest [213].

Considering the inherent metastability of Li_7 clusters, an additional significant population of imperfect Li_n clusters (with $3 \geq n > 7$) can be expected ("broken flowers"). The lithium atoms belonging to these clusters are undercoordinated with respect to the Li_7 central atom but still occupying adjacent C_6 rings, therefore they can be expected to produce a signal at a higher shift than the "free" lithium atoms in LiC_6. Li_3 motifs can analogously appear as "broken stars". Additionally, both the crown atoms of the Li_7 and the prongs of the Li_4 motifs have lower coordination than the respective central atoms. As such, there are many possible realisations of microstructures with a wide range of coordinations, thus we may attribute the broad spectral feature at 100–200 ppm to a superposition of resonances corresponding to all the above.

Both the high-ppm peaks and the broad 100–200 ppm spectral feature are correlated with the increase of the 10–13 ppm feature. This is a strong indication that the degradation of superdense structures directly corresponds to the appearance of a new Li environment. In line with previous assignments of the low-ppm feature in literature, this can correspond to either Li–Li dimers occurring as the smallest possible decomposition product before isolated Li, or to the formation of locally Li-depleted LiC_{6+x} regions following the ejection of Li at the surface. Of note, these two patterns can coexist as a result of decomposition (cf.Figure 4.11).

While preparing a reference sample of fully intercalated LiC_6 for ^7Li NMR spectra, we observed unexpected high-ppm resonances. Confidently ruling out that the observed signatures arise from residual metallic lithium, we attribute these to superdense LiC_{6-x} compounds formed under ambient pressure. We investigate the evolution of the signal under calendaric aging and rationalise our observations with *ab initio* simulations. We infer that the signal arises from sizeable domains containing Li_7 ("flowers") and/or Li_4 ("stars") motifs in sufficient amounts and we estimate the long-term (meta-)stability. *Ab initio* thermodynamics confirms that a non-negligible excess of lithium enters spontaneously, which, to the best of our knowledge, had never been considered before. These findings challenge the currently accepted hypothesis that, since LiC_2 can only be prepared under high pressure [181, 187, 191], any additonal intercalation beyond LiC_6 is implausible. In hindsight, the simple consideration that the range of stoichiometries between LiC_6 and LiC_2 spans 200% states of charge beyond 100% should suggest prudence in such an assumption. Yet, it was never rigorously verified. In our view, multiple previous works on electrochemical cells contain indications compatible with at least a sparkle of doubt [192, 193, 195]. To be fair, the question of assessing the true capacity of ordered graphitic hosts was explicitly addressed for bilayer or multilayer graphene [17, 48]. Inexplicably however, the evidence of overlithiation in the latter did not reopen the question of analogous occurrence in extended graphite – which is the material actually used in working batteries. For decades, superdense graphite intercalation compounds have been considered only accessible as decomposition products of LiC_2 under high-pressure synthesis ("from above") [181, 187, 191]. Here we confirm that superdense compositions are also accessible directly as overintercalation products of LiC_6 at ambient pressure ("from below"). If this is possible under the synthesis conditions employed here, it is reasonable to expect that overlithiation is further favoured under an applied potential. Particularly in fast charging conditions, lithium plating is also increasingly favoured [214]. Hence, the most intriguing aspect is the interplay of partially reversible plating, overlithiation and reintercalation. On this account, we call for a reconsideration of the role of overlithiation, so far excluded from the picture with graphite as a host. Taking overlithiation into consideration may also shed light onto other hitherto unexplained phenomena, such as the apparent "disappearance" of some amount of available lithium between cycles, the latter commonly attributed solely to the formation of solid electrolyte interfaces (SEI) and "dead" lithium [215]. Finally, with regards to the use of NMR for the detection of plating and dendrite formation, our results also suggest that caution is indicated with assigning high-ppm signals non-specifically to the emergence of metallic lithium deposits.

4.4 Details on the Experimental Section

4.4.1 Sample Preparation

The LiC_6 sample was prepared using an infiltration technique. Metallic lithium with 99.9 % purity (Sigma Aldrich) was intercalated in highly oriented pyrolytic graphite (HOPG) from Goodfellow. The lithium metal was heated above the melting point until 220 °C was reached. Note that the self-cleaning property of lithium ensures an even higher purity of the liquid lithium metal bulk. [179] Afterwards the HOPG was added. As one can see in Figure 4.7.a, the sample was cut, in order to expose some edges and to facilitate the starting of the intercalation by maximizing lithium wetting on graphite, although recent studies show that graphite is lithiophilic. [179] In order to ensure complete lithium intercalation, the high-temperature intercalation process has been allowed to take place for a period of over two months in an inert atmosphere. This long infiltration time was necessary due to the dimension of the host material pre-intercalation size of 10.0x(4.9)x2.0 mm^3. [177–179] The dimensions were determined by the requirement to fit the final sample into an NMR tube of 5 mm diameter. The bracket notation is due to the cut of the original 10.0x10.0x2.0 mm^3 piece. The final sample was, by applying a cleaning procedure, adapted to fit within the NMR tube, so reduced even more in dimension. This was done, before recording the nuclear magnetic resonance (NMR) spectra, by polishing the fully intercalated HOPG mechanically using sand paper, in order to avoid further chemical contamination. The full synthesis workflow is sketched in Figure 4.7.

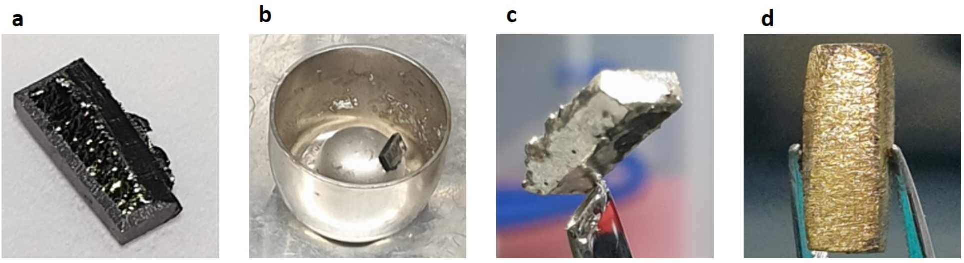

Figure 4.7 Summary of the steps to produce the lithium–graphite intercalation compound. a, shows the raw sample of HOPG, cut mechanically from a 10.0x10.0x2.0 mm^3 piece. b, represents the molten lithium in a nickel crucible and the subsequently inserted HOPG, whereas c, is the fully intercalated sample after *ca.* two months, plated by lithium metal, as it was removed from the molten lithium at the end of the synthesis. d, shows the final stage post polishing. The golden colour indicates full lithiation.

4.4.2 ^{7}Li Nuclear Magnetic Resonance

Susceptibility effects are known to be present when measuring the ^{7}Li NMR spectra of metallic or pseudo-metallic samples. In particular, lithium metal can exhibit shift variations of *ca.* 10–30 ppm, depending on the sample geometry and the angle of the c-axis of the sample with respect to the B_0 field direction. The maximum difference will be found comparing sample orientations with surface normal vectors aligned parallel and perpendicular to B_0. [211, 216] To investigate the influence of the susceptibility, our sample

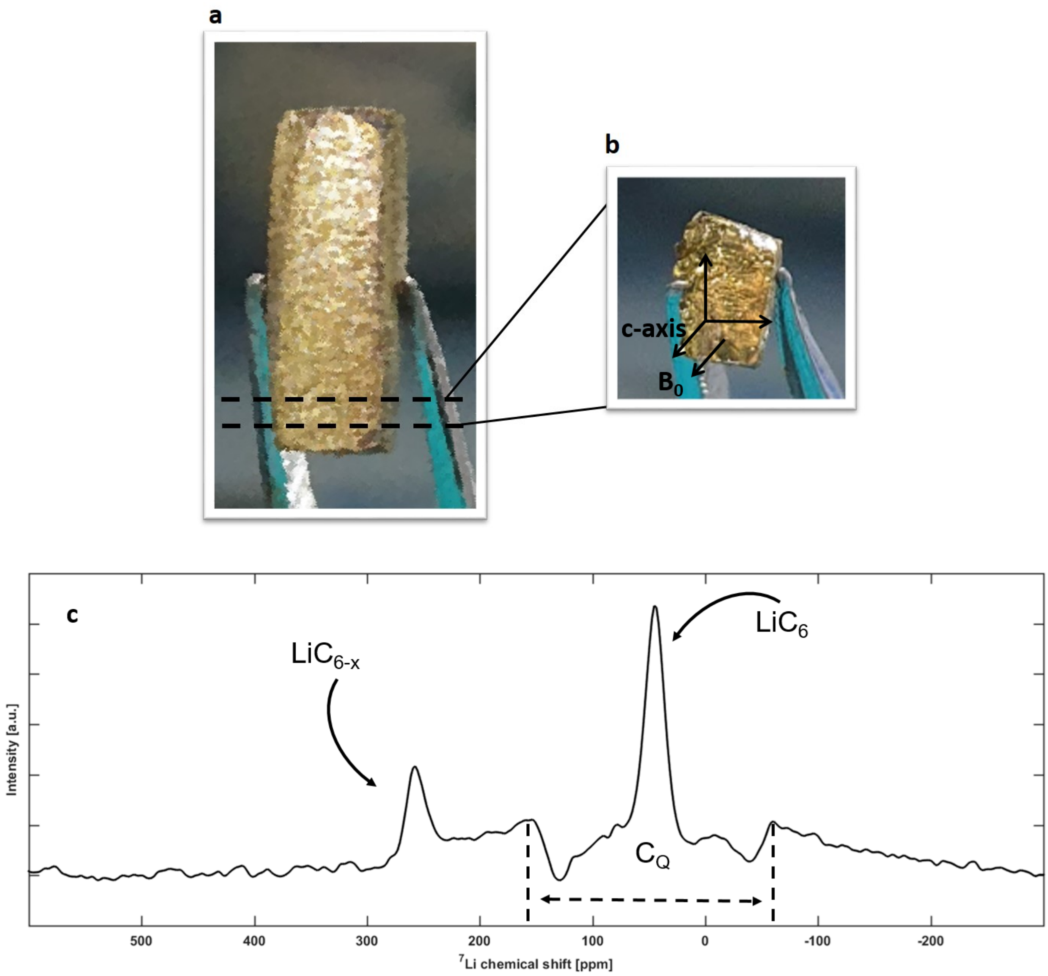

Figure 4.8 Photograph of the fully intercalated sample and the cut out fraction for the in-plane ^{7}Li NMR measurements. a, showing the whole sample after mechanical cleaning; the black dashed lines indicate the location of the cut to produce a sliced sample that would fit into an NMR tube with its c-axis rotated by $90°$ with respect to the external magnetic field B_0. b, displays the sliced part from the main sample for measurement at the parallel orientation of the c-axis towards the B_0 field. The a and b directions are not labeled. c, ^{7}Li NMR spectrum of the sample with its c-axis oriented parallel to the B_0 field direction. The signature at 45 ppm corresponds to the LiC_6 phase, while the peak at 264 ppm, excluding a lithium metal signal (see main text), corresponds to the LiC_{6-x} phase.

was cut as shown in Figure 4.8.a-b. Figure 4.8.c shows the ^{7}Li NMR spectrum, with the graphite c-axis oriented parallel to the B_0 field, while Figure 3 in the main text (as well as Figure S3) shows the spectrum taken at perpendicular c-axis orientation towards B_0. The signal-to-noise ratio (S/N) is weaker due to the smaller size of the sample. The high-ppm chemical shift is moving from 274 ppm for perpendicular orientation to 264 ppm for parallel orientation. The effect is similar to that observed for a Li metal sheet, but of different magnitude (10 *vs.* 30 ppm, respectively). [211] However, given the different shapes of the two samples (Figure 4.8) and the anisotropic nature of susceptibility in graphite, no quantitative conclusion can be drawn at this point. Since our main conclusions are reached by comparing a sample with invariant shape at identical orientation, this aspect is not characterized in more detail here.

By comparing the resonance frequencies of the satellite transitions of the resonance at 45 ppm for our single-crystal sample placed with its crystallographic c-axis in perpendicular and parallel directions with respect to the magnetic field B_0, the quadrupolar coupling constant can be extracted. The results are consistent with the values reported by Roth *et al.* [217], with Figure 4.8.c showing the full quadrupolar constant C_Q at *ca.* 47 kHz and Figure 3.b in the main text shows $C_{Q/2}$ with *ca.* 23 kHz.

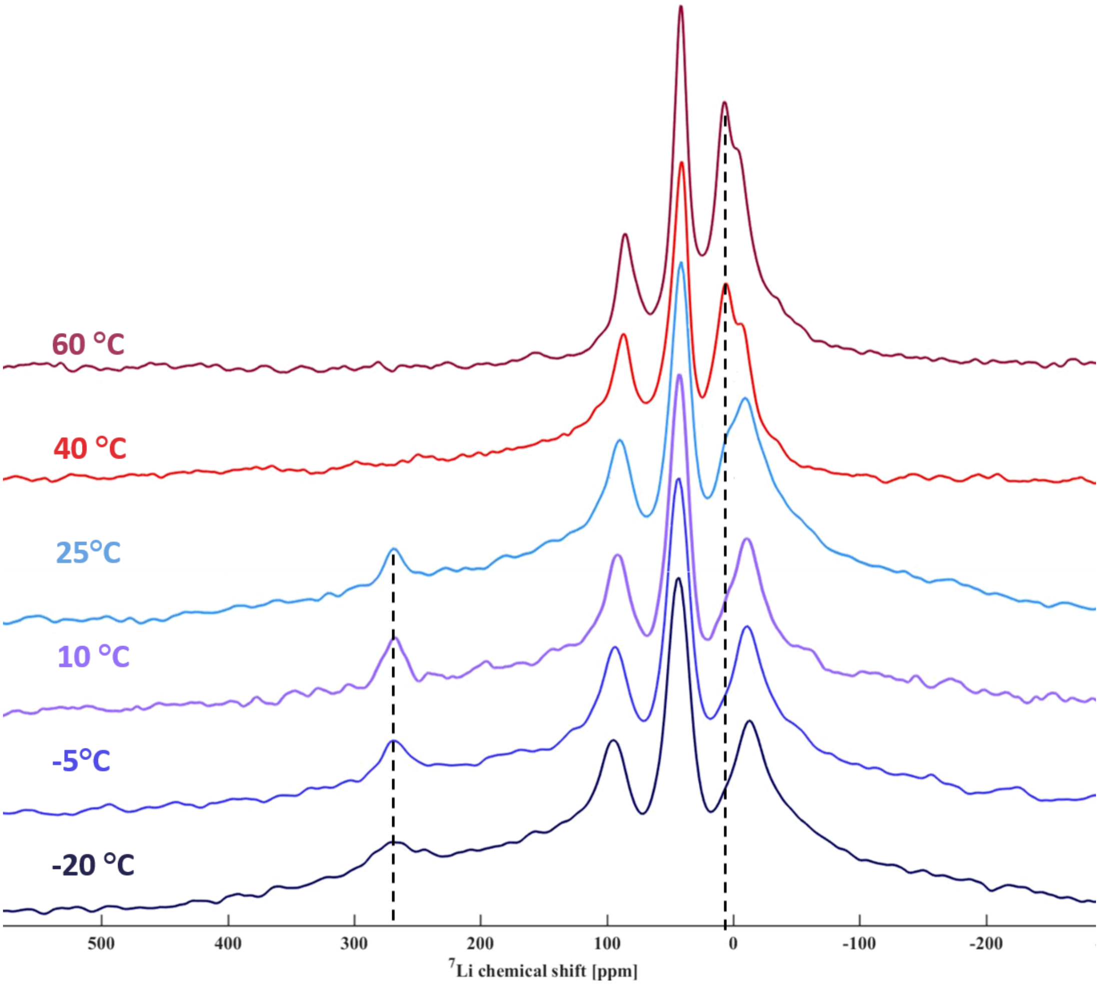

Figure 4.9 Representation of the ^{7}Li static NMR in function of different temperatures during the heat treatment cycle of the sample after 5 months ageing. ^{7}Li-NMR spectra recorded from -20 °C to 60 °C, show the evolution of the high-ppm signal and the appearance of the low-ppm feature at *ca.* 10-13 ppm, marked both by dashed lines.

Temperature dependent static ^{7}Li NMR of the lithiated HOPG sample was performed after 5 months of ageing of the cleaned sample, after removal of all surface decomposition products. The spectra were recorded with increasing temperature from -20 °C to 60 °C in steps of 15 °C. For temperature adjustment, the integrated system for the temperature control of the Bruker DIFFBB probe was used. Figure 4.9 shows the temperature series of the NMR spectra during heating of the sample. Interestingly, the residual high-ppm peak, discussed in the main text, disappears, while concomitantly a peak at *ca.* 10–13 ppm rises. In addition, attention has to be paid to a broad background signal of the spectra between 130–300 ppm at temperatures from -20 °C to 25 °C. This background signal disappears at $40 - 60$ °C. Upon cooling to 25 °C, it reappears and, correlated to this intensity change, the peak at 10–13 ppm decreases in intensity. This indicates a reversible character of the associated species. The high-ppm feature, however shows an irreversible character. The background entirely vanishes after an additional ageing of two months (*cf.* Figure 4.5). After the full seven months of ageing, the sharp peak at *ca.* 11 ppm exhibits a quadrupolar pattern of *ca.* 40 kHz. This and the overall narrower linewidths indicate that the sample reached a more ordered equilibrium state, as visible in Figure 6 (violet curve).

4.5 Ab initio Thermodynamics

4.5.1 General Concept

The idea behind *ab initio* atomistic thermodynamics is to evaluate relative stabilities of different stoichiometries as a function of the chemical potential of the variable components (in our case, μ_{Li}), by expressing them in terms of quantities directly accessible via first principle calculations. Our system is effectively graphite in equilibrium with a reservoir of liquid Li, so we can in principle express free energies and free energy variations as a function of μ_{Li}. Following the same well established reasoning for surfaces, [212] we can partition the total free energy of the entire system as

$$G = G_{\mathrm{graphite}} + G_{\mathrm{lithium}} + \Delta G^{\mathrm{interc}} \tag{4.1}$$

where graphite and lithium are extended (infinite) regions and $\Delta G_{\mathrm{interc}}$ accounts for the (finite) intercalation region. Then we may write, for any lithiated compound in the intercalation region, with N_{Li} Li atoms and N_{C} C atoms per C_6 formula:

$$\Delta G^{\mathrm{interc}} = G - G_{\mathrm{graphite}} - G_{\mathrm{lithium}} = \tag{4.2}$$

$$= G(T, P, N_{\mathrm{C}}, N_{\mathrm{Li}}) - N_{\mathrm{C}} g_{\mathrm{C}}(T, P) - N_{\mathrm{Li}} \mu_{\mathrm{Li}}(T, P) \quad , \tag{4.3}$$

where g denotes the partial molar free energy, or, for an infinite reservoir such as liquid Li, the chemical potential. If we now introduce the limit case

$$\Delta G^{\mathrm{interc}}_{\mathrm{empty}} = G(T, P, N_{\mathrm{C}}, 0) - N_{\mathrm{C}} g_{\mathrm{C}}(T, P) \tag{4.4}$$

as the “formation energy” of empty graphite in the intercalation region (in other words, a reference finite slab of empty graphite), then we can express

$$\begin{aligned} \Delta\Delta G^{\mathrm{interc}} &= \Delta G^{\mathrm{interc}} - \Delta G^{\mathrm{interc}}_{\mathrm{empty}} = \\ &= G(T, P, N_{\mathrm{C}}, N_{\mathrm{Li}}) - G(T, P, N_{\mathrm{C}}, 0) - N_{\mathrm{Li}} \mu_{\mathrm{Li}}(T, P) \quad . \end{aligned} \tag{4.5}$$

Trivially, this reference will be zero at any T, P and will allow us to conveniently evaluate the relative stability of any lithiated compound simply with respect to empty graphite. In that regard, we simply indicate those as ΔG rather than $\Delta\Delta G$ in the main text.

4.5.2 Lithium chemical potential

In general, we can express the chemical potential of lithium at any (T, P) as

$$\mu_{\mathrm{Li}}(T,P) = \mu_{\mathrm{Li}}(0,0) + \Delta\mu_{\mathrm{Li}}(T,P) \tag{4.6}$$

and use the fact that at vanishing temperature and pressure, the chemical potential is equal to the internal energy U of the stable state at $T = 0$ K (*i.e.* BCC lithium):

$$\mu_{\mathrm{Li}}(0,0) = g_{\mathrm{Li}}(0,0) = U_{\mathrm{Li}}(0,0) \simeq E^{\mathrm{DFT}}_{\mathrm{Li,BCC}} \quad , \tag{4.7}$$

where we approximate the internal energy as the calculated DFT total energy (neglecting the zero point energy). The variation $\Delta\mu_{\mathrm{Li}}(T,P)$ may be evaluated from *ab initio* calculations, or, where available, extracted from thermochemical tables [206] as:

$$\begin{aligned}\Delta\mu_{\mathrm{Li}}(T,P) &= \Delta G_{\mathrm{Li}}(T,P) = \Delta H - T\Delta S = \\ &= [H(T,P) - H(0,0)] - T\,[S(T,P) - S(0,0)] \quad .\end{aligned}$$

Technically, thermochemical tables only report values at the standard pressure of $P^0 = 0.1$ MPa rather than the hypothetical $P = 0$. However, as will be apparent in the next section, up to P^0 the effect of pressure on the chemical potential of condensed phases is negligible, so we can safely approximate $H(0,0) = H(0,P^0)$ and $S(0,0) = S(0,P^0)$, obtaining:

$$\Delta\mu_{\mathrm{Li}}(T,P^0) \simeq \left[H(T,P^0) - H(0,P^0)\right] - T\left[S(T,P^0) - S(0,P^0)\right] \quad . \tag{4.8}$$

In principle, we may use the above equation to directly obtain the value of $\Delta\mu_{\mathrm{Li}}(T,P^0)$ at the experimental temperature $T = 500$ K. However, this would require extrapolating H and S to $T = 0$ K for *liquid* lithium, as those are not directly included in the corresponding thermochemical table – contrary to the reference solid state. Thus, it is safer to calculate $\Delta\mu_{\mathrm{Li}}$ for solid lithium up to the fusion temperature $T_{\mathrm{fus}} = 453.69$ K and then, using the fact that, at the fusion temperature:

$$\mu_{\mathrm{Li,sol}} = \mu_{\mathrm{Li,liq}} \quad , \tag{4.9}$$

proceed to calculate the chemical potential of liquid lithium for higher temperatures from there. Since the experimental temperature is not much larger than the fusion temperature, we can from this point on use a simple linear approximation for the variation of the chemical potential:

$$\Delta(T,P) = \mu(T_{\mathrm{fus}},P^0) - s\Delta T + v\Delta P \tag{4.10}$$

with s is the negative molar entropy (also tabulated) and v is the molar volume, which can be easily calculated from the experimental density.

Of note, it is easy to verify that $s\Delta P$, for $\Delta P = 0.1$ MPa, only changes the chemical potential by 10^{-5} eV, justifying the approximation in Equation. 4.8. Conversely, at the much higher pressures usually employed in the synthesis of $\mathrm{LiC_2}$, the effect is in the order of 1 eV. We note in passing that this straightforwardly brings the formation free energy $\mathrm{LiC_2}$ in the thermally accessible range at high pressure, in agreement to its reported synthesis.

4.5.3 Free Energies of Graphite and $\mathrm{Li}_x\mathrm{C}_y$

At this point we have a full, quantitative expression for μ_{Li} at any finite T and P. Let us now go back to Eqn. 4.5 and let us simplify the notation posing $N_{\mathrm{Li}} = x$ and $N_{\mathrm{C}} = y$ for a generic $\mathrm{Li}_x\mathrm{C}_y$ intercalation compound. As a first approximation (often used in AITD), one may neglect all T and P effects on the intercalated compounds, thus replacing the free energy with the DFT total energy:

$$G_{\mathrm{Li_xC_y}}(T,P,x,y) \simeq U_{\mathrm{Li_xC_y}}(0,0) \simeq E^{\mathrm{DFT}}_{\mathrm{Li_xC_y}} \quad , \tag{4.11}$$

and analogously for empty graphite. This approximation is extremely convenient and has been employed successfully for (semi-)quantitative predictions especially in heterogeneous catalysis, where it is largely justified by the fact that *i)* there the chemical potential which is allowed to vary is typically of some gas species, hence it is much more sensitive to T and P effect than condensed phases, and *ii)* it is assumed that the competing species are similar enough that the vibrational, entropic and PV contributions between different species largely cancel each other. [212] This allows to draw simple diagrams in which the relative stabilities of different stoichiometries vary linearly with the chemical potential of the variable component, with slopes proportional to its content in the formula. However, the neglection of the finite temperature contributions to the total energies should be carefully evaluated case by case – as it turns out, they do make a difference in our case.

In the most complete picture, and employing the usual approximation of expressing the zero-temperature internal energy as the DFT total energy, one may write

$$G = F + PV =\simeq E^{\mathrm{DFT}} + F_{vib} + PV; \tag{4.12}$$

where F_{vib} is the vibrational free energy, directly calculated from the first-principles vibrational density of states in the harmonic approximation. [205] The latter includes the Zero Point Energy, the vibrational contribution to the internal energy and the vibrational entropy. This, the only contribution neglected here is the configurational entropy. [218] Its estimation is computationally intensive. For the scope of this work we may limit ourselves to qualitatively note that, being by definition always positive or zero, it would be positive for lithiated compounds and zero for pristine graphite and perfect LiC_2, for which only one realisation is possible. Therefore, it would lower the formation free energy for all the intermediate compounds.

All the calculated free energies are normalized per graphite unit (or, equivalently and consistently with the notation used here, per mole of Li_xC_y with $y = 6$).

4.6 Ab initio Molecular Dynamics

4.6.1 Diffusion Coefficients and Effective Diffusion Barrier

Due to the high computational cost of DFT, MD was performed based on Density Functional Tight Binding (DFTB), a semi-empirical tight-binding approximation to DFT, with the recently developed parametrization [112, 119] augmented with Li–Li repulsion. The diffusion coefficients were calculated from the mean square displacements using Einstein's relation

$$D = \frac{1}{2nt}\left\langle |r(t) - r(0)|^2 \right\rangle \tag{4.13}$$

where $r(t)$ is the position at time t and n is the number of degrees of freedom. Only the 2D diffusion in the xy plane was taken into account. The analysis was performed using a module implemented in ASE, using an average over 3 segments per trajectory to improve statistics.

The diffusion coefficients are reported in Table 4.2 and plotted in Figure 4.10.

Table 4.2 Diffusion Coefficients from MD

$T\ (K)$	500	750	1000
$D \pm \sigma\ (cm^2/s)$	$4.1 \cdot 10^{-7} \pm 4.6 \cdot 10^{-7}$	$6.3 \cdot 10^{-6} \pm 1.5 \cdot 10^{-6}$	$2.3 \cdot 10^{-5} \pm 4.4 \cdot 10^{-6}$

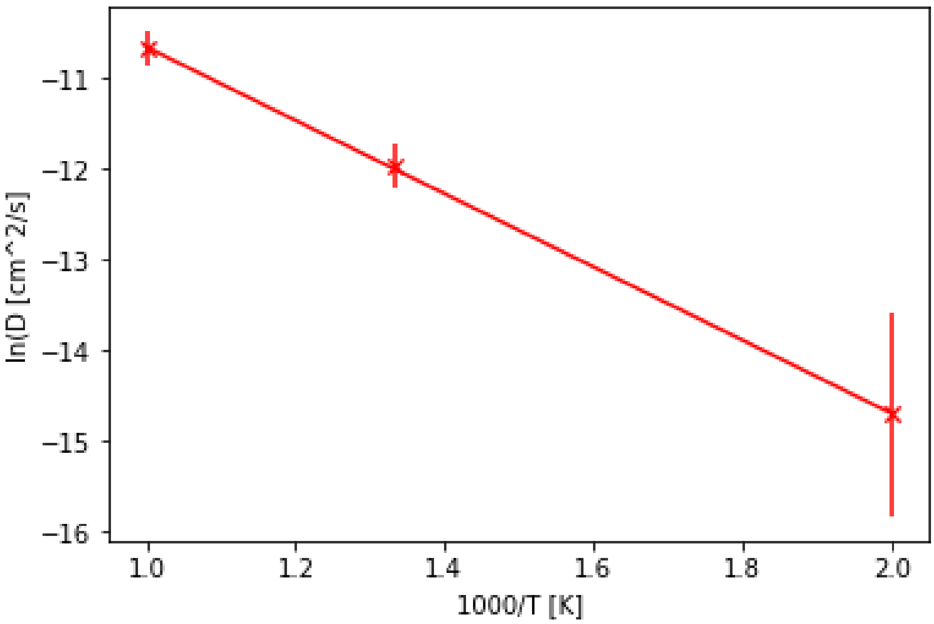

Figure 4.10 Arrhenius plot of diffusion coefficients at 500, 750 and 1000 K. The error bars are computed by error propagation based on the standard deviation of the mean square displacement. The error for 500 K is larger due to the limited statistics, due to the fact that at lower temperatures the trajectory is dominated by vibrational noise with very few true diffusion events (jumps).

The ratio between characteristic times t_2 and t_1 at temperatures T_2 and T_1 can be calculated as

$$\frac{t_2}{t_1} = \frac{k_1}{k_2} = \exp\left[\frac{(T_1 - T_2) \cdot E_a}{k_B \cdot T_1 \cdot T_2}\right] \tag{4.14}$$

where k_1 and k_2 are the rates at T_1 and T_2 respectively, E_a is the effective activation barrier of the diffusion, and k_B is the Boltzmann constant.

4.6.2 Degradation of Clusters from MD Snapshots

Figure 4.11 shows selected snapshots of the MD trajectory, at 750 K to show advanced stages of degradation of Li_7 clusters. Similar fragments appear in the 500 K trajectory, only significantly more slowly. The occurrence of disordered planar clusters with various coordinations, as well as dimers and trimers is evident.

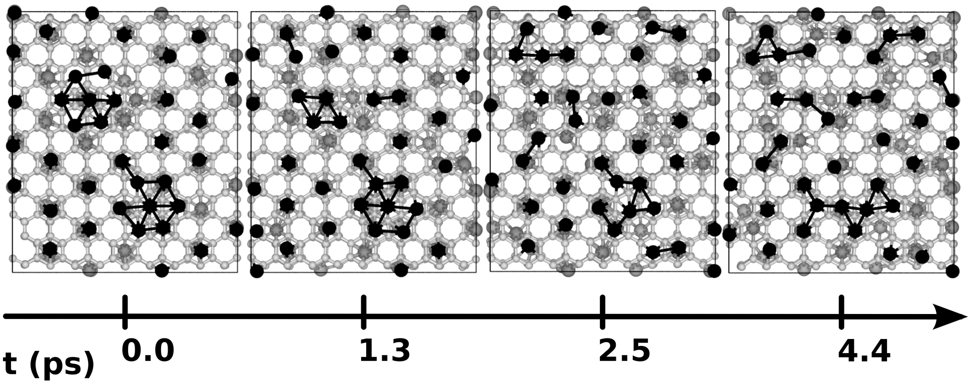

Figure 4.11 Selected snapshots in the MD trajectory at 750 K showing the frequent appearance of Li-Li dimers as transient byproducts of superdense cluster decomposition.

5 Investigating Diffusion of Lithium intercalated in Graphite by a Combination of charged kinetic Monte Carlo and Spin-alignment Echo Nuclear Magnetic Resonance

The following describes the results of the lithium intercalation within ideal HOPG. This serves as a reference sample in order to validate the combination of kMC and ILT-SAE which was presented in the previous chapters. This chapter is part of a publication which is currently under preparation, where some parts are adapted to follow the structure of the thesis and might overlap with the general introduction in some concepts.The kMC simulations in this work were performed using `kmos` kMC code generator as a basis. [129]. A particular challenge in ion transport is the charge of the particles and the resulting long range interaction by electrostatic forces. This motivated to implement a dedicated kMC algorithm for charged particles. 5.2 This work has been conducted in collaboration with Sandra Döpking (FU Berlin) and S. Matera (FU Berlin and FHI Berlin), who developed the algorithm and implemented it for a cubic lattice showcase by extending the FORTRAN code generated by `kmos`. Cristina Grosu adapted this implementation for Li^+ diffusion on the hexagonal graphite lattice. Peter Jakes and Steffen Merz contributed valuable clues for the spectra acquisitions, discussions and sample preparation. Data evaluation was done by Cristina Grosu in collaboration with Josef Granwehr and Steffen Merz. Chiara Panosetti helped in the design of the kMC model, based on the first principle calculations

5.1 Introduction

Li^+ diffusion in graphite, based on the hexagonal structure LiC_6 stoichiometry (commonly known as 100 % SOC) will be used as a validation and reference system for modelling ion diffusion in solid materials. When modelling such systems, and in particular intercalation compoundswe can often exploit that the matrix, built of the atoms of the host material, is only mildly affected by the the presence of additional ions. On its way through this matrix, an ion will most of the time reside in the low energy sites defined by the atomic structure of the host. When an ion moves from one site to another it typically has to overcome a significant (free) energy barrier and thus such events appear rarely on the timescale of atomic motion. Assessing diffusion by means of molecular dynamics simulations then becomes computationally expensive, because the diffusion is dominated by the rare transitions between the sites. With other words long simulation times are necessary in order to achieve proper statistical sampling. To overcome this limitation, we coarse-grain the dynamics to these rare events and employ a discrete description where the ion jumps between different sites. Instead of following the detailed trajectories by employing molecular dynamics, we therefore simulate the sequence of jumps using the kinetic Monte Carlo (kMC) technique, in combination with a novel implementation which allows us to describe the charged lithium ion moving under an external field. To assess diffusivity experimentally we decided for NMR which already showed great success in investigating ion mobility within battery materials. [63, 153] The working principle of SLR-NMR for Li intercalated in graphite was already proven with a robust approximation by Langer *et al.* [63] On the other hand SAE-NMR is more sensitive to extremely slow translational and rotational jump processes, allowing for a broader range of timescales for the observed processes, `c.f.` chapter 3. The peculiarity of SAE-NMR is that it can access much slower lithium ion motions compared to other NMR techniques as mentioned in section 3.2.2. To concisely recapitulate the basics, a SAE-NMR signal is observed if local changes of the electric field gradient (EFG) are sampled by the nucleus. The echo decay is then characterized by correlation time constants, i.e. τ_c that may be associated to a hopping time between sites, provided that the origin and the destination of a jump are not electrically equivalent. [63,153] A single ion moving to a neighboring single defect site thus does not "see" a different environment before and after the jump due to the inversion symmetry with respect to the jump barrier. It is, therefore, rather the ions in the environment of the initial and final sites which produce the SAE signal. Within the LiC_6, in principle, a fully ideal – defect free – system, the lithium sites are electrically equivalent. Advanced analysis tools like the Inverse Laplace Transformation (ILT) help to unravel the detailed nature of this system from an experimental point of view. Note that ILT was already used successfully for studying other battery materials, *i.e.* LTO. [152,153] From the theoretical perspective, the standard kinetic Monte Carlo offers a good starting point, but is limited as it describes the lithium ions as neutral species. Hereby, the charge treatment for the lithium ions is necessary. On top the external field will mimic closer the real diffusivity from the solid materials.

5.1.1 Standard kinetic Monte Carlo

The basic principle of a kMC simulation is to generate a Poisson process of stochastic events with a hierarchy of rate constants in such a way that events with higher rates are more likely to occur than slower ones. The state of the system is modeled as a vectorial integer random variable $X \in \mathbb{Z}^D$, with realizations denoted by x. Each entry of X corresponds to a spatial site in the electrode material, where a charge carrier (or any other kind of species) can bind. Its value defines which species is bound there.

X evolves in time by subsequently executing processes ξ,

$$\xi : \quad x \rightarrow x + d_\xi \quad , \tag{5.1}$$

where d_ξ is the change in the state due to execution of the processes ξ and independent of the current realization x. Such processes could be the jump of a charge carrier from a site i to a neighboring site j. In the following, we restrict ourselves to the rather general case, where d_ξ is sparse, i.e. it has only $O(1)$ non-zero entries, `i.e.` their number is independent of the total number of sites D. Further, we assume that the changes caused by each process are only local - only the species on nearby sites are involved in a process - and we therefore have $O(D)$ different processes. The rare event nature of the processes allows us to regard the time evolution $X(t)$ as continuous time Markov jump processes. The probability $p(x,t)$ to find the system in state x at time t then obeys the master equation [130,219]

$$\frac{dp(x,t)}{dt} = \sum_\xi a_\xi(x - d_\xi)p(x - d_\xi, t) - \sum_\xi a_\xi(x)p(x,t) \quad , \tag{5.2}$$

where $a_\xi(x)$ is the propensity (or rate function) of the process ξ. An equivalent formulation in terms of the process $X(t)$ is

$$X(t) = X(0) + \sum_\xi d_\xi P_\xi \left(\int_0^t a_\xi(X(s))ds \right) \quad , \tag{5.3}$$

where the P_ξ are independent unit rate Poisson processes [220]. For any reasonable choice of D, the numerical solution of the master equation must be regarded as intractable, albeit progress has been made during the last years for not too complex problems [127, 135, 221]. Therefore, any practical and unbiased approach to estimate expected values of the process $X(t)$ is based on simulating it by some kind of kinetic Monte Carlo (kMC) algorithm, sometimes named Dynamic Monte Carlo or simply Stochastic Simulation [125,222]. Albeit there exist different kinds of kMC algorithms, the majority can be cast into the abstract form

Algorithm 1 Pseudocode of an abstract kinetic Monte Carlo algorithm

```
initialize $x_0$ and $t_0$,
for $n = 0 : N - 1$ do
    calculate/update propensity values $k_{\xi,n} = a_\xi(x_n)$
    determine time step $\Delta t$ on basis of the propensity values $k_{\xi,n}$,
    set $t_{n+1} = t_n + \Delta t$
    select a process $\chi_n$ on basis of $k_{\xi,n}$, set $x_{n+1} = x_n + d_{\chi_n}$
end for
```

for N kMC steps.

5.2 Charged kinetic Monte Carlo (ckMC)

The implementation of the external field in is constrained to a cubic lattice. Due to that, the hexagonal structure of the graphite was mapped onto a 3D cubic lattice. With the corresponding processes, the ones that were identified on the hexagonal unit cell, subsequently were mapped onto the simple cubic lattice. The implementation is available on request from the author and more details are given in the Appendix B. The charged kinetic Monte Carlo is not new, however it was never applied to lithium ion diffusivity under the influence of an external field. In literature, so far it was only used for the description of semi-conductors, ionized-gases or simple cluster systems. [223, 224] Additionally, treating diffusion processes with charged particles becomes quickly costly and not trivial. In particular when a charged particle moves in a certain environment, it will influence also the surroundings of the neighbouring particles and will move slower or faster depending on it. Moreover, in a system where ideally it is necessary to know the right time scales for the processes, problems can occur if we fix a step size within the MC. Ideally the steps size should be small enough in a way that the fastest diffusion or reaction is captured. However with only small step sizes, the sampling of slower reactions is inefficient. The sampling of all timescales might quickly become computationally prohibitive for very large system sizes. [222] Usually, diffusion is much faster than chemical reactions. In our case, we do not deal with reactions at all, however the diffusion processes are changing under an external potential,that might slowly build up due to charge accumulation or separation e.g. at or across interfaces. Here, the necessity of having explicit charges within the kMC approach is relevant. Additionally, in structurally highly ordered, *i.e.* single crystalline systems, defects are also required for the movement of atoms or ions, otherwise jumps simply not occur. The concentration of point defects will then influence the mobility. In this study, the so-called Variable Step Size Algorithm within the `kmos` [129] framework is employed. However, the following methodology is largely independent of the employed kMC algorithm, because it only focuses on the most expensive part —for problems which involve long range interactions— which is the update of the propensity values. Note that the update of the propensity values has to be done in all kMC algorithms. Most kMC models for charge transport simulation employ propensity models in which long range interactions only enter by the difference of the change in (free) energy $\Delta E_\xi(x)$ caused by the event $x \to x + d_\xi$, such as Marcus theory [225] or Transition State theory c.f. Section 2.2.4 with Bronsted-Evans-Polanyi terms [226]. These models can be cast into the general form

$$a_\xi(x) = a_\xi\left(x, \Delta E_\xi(x)\right) \quad , \tag{5.4}$$

where the explicit dependence on x is only local, i.e. only those entries of x have an impact which represent the immediate surrounding of ξ. Then $\Delta E_\xi(x) = E(x + d_\xi) - E(x)$ and $E(x)$ is the (free) energy in the state x due to the complex interaction. In the case of long range interactions $\Delta E_\xi(x)$ will depend on $O(D)$ entries of x. Thus it is necessary to update the $O(D)$ propensity values in every kMC step.

To be specific, in this work we employ:

$$a_\xi(x) = \theta_\xi(x) f_\xi(x) \quad , \tag{5.5}$$

with

$$f_\xi(x) = \exp\left(-\beta\left(E_{a,\xi} + \frac{1}{2}\Delta E_\xi(x)\right)\right) \quad . \tag{5.6}$$

Here, $\theta_\xi(x)$ is only local, with a constant prefactor which acts as an indicator function and which returns one if the process is possible otherwise it returns zero. For the long range energy contribution $E(x)$, pairwise interactions are assumed

$$E(x) = q(x)^T V q(x) \quad , \tag{5.7}$$

with the dense interaction matrix $V \in (R)^{D\times D}$ and the charge state $q(x) : \mathbb{Z}^D \to \mathbb{R}^D$. In case of isotropic Coulomb interactions, the element of V would be $V_{ij} = \epsilon^{-1}/||r_i - r_j||$ for non-periodic problems, where r_i and r_j are the positions of the i-th and the j-th site. For the charge state $q(x) : \mathbb{Z}^D \to \mathbb{R}^D$ it is assumed that $q(x + d_\xi) = q(x) + \Delta q_\xi$, i.e. every process induces a constant sparse shift Δq_ξ in the charge state. For the problem at hand, this is trivial because q can be identified with x ($x_i = 1$: a Li$^+$ is on site i, and $x_i = 0$: site i is empty). The energy differences can be exploited in the $(n + 1)$-th step and can be written as $E_\xi(x_{n+1}) = E_\xi(x_n) + 2\Delta q_\xi^T V \Delta q_{\chi_n}$, where χ_n is the process executed in the n-step. Given the value for f_ξ in the n-th kMC step, $f_{\xi,n}$, the update rule can be formulated as

$$f_{\xi,n+1} = f_{\xi,n} g_{\xi,\chi_n}, \text{ with } g_{\xi,\chi} = \exp(-\beta\Delta q_\xi^T V \Delta q_\chi) \quad . \tag{5.8}$$

The factors $g_{\xi,\chi}$ can now be precomputed and stored. In the general case without translational symmetry, there are $O(D^2)$ factors $g_{\xi,\chi} \neq 1$ and storage consumption will be the limiting factor for large D. For the translational invariant problem of this study, which can be mapped onto a regular lattice, one can exploit that V is of convolution type and the memory requirement is reduced to $O(D)$. Irrespective of this, we can then perform the update of the propensity values in every step exploiting Equation (5.10) and (5.8). This boils down to updating a vector which carries the values for $\theta_\xi(x)$, which requires only to recalculate a few of the values because of the locality of $\theta_\xi(x)$. Updating the vector and carrying $f_{\xi,n+1}$ results in $O(D)$ scaling and calculating the propensity values $k_{\xi,n+1}$ from both vectors results again in $O(D)$ scaling behaviour.

Still, the standard kMC requires $O(D)$ operations per step for problems with long range interactions. For large values of D, this means a substantial overhead compared to problems with only local interactions. The idea to overcome this problem is now to replace the interaction matrix V by a sparse approximation $\tilde{V}$ in the update rule Equation (5.8). In practice, the interactions are truncated after a certain distance. The sparsity of $\tilde{V}$ implies that most factors $g_{\xi,\chi}$ equal one and thus it is necessary to update $O(1)$ of the factors f_ξ (and therefore propensities) per time step. Starting with correct values for the factors f_ξ, however, this will lead to errors in every kMC step which will accumulate over time. To avoid a too strong deviation of the propensities, the update rule (5.8) in every H steps is replaced by the calculation of the factors f_ξ (and the propensities) using Equation (5.10) with the correct original interaction V leading to the following update rule (again χ_n is the process executed in the n-th step):

$$f_{\xi,n+1} = \begin{cases} = \exp\left(-\beta\left(E_{a,\xi} + \frac{1}{2}\Delta E_\xi(x_{n+1})\right)\right) & \text{if } n = H \\ = f_{\xi,n}\tilde{g}_{\xi,\chi_n} & \text{else} \end{cases} \tag{5.9}$$

5.2.1 Extension for Coulomb Interactions

The Coulomb interaction between the ions is long range and can not be truncated. Thus, the barriers, needed to calculate the rate constants from Section 2.2.4, and hence the rate values $r_{\xi,n}$, depend on all entries of the current configuration x_n, they are needed in every kMC step. Calculating them beforehand or on-the-fly during the kMC simulation is prohibitively expensive, even with DFTB. In order to overcome this problem, we employ the Bronsted-Evans-Polanyi approximation (BEP) to incorporate the interaction. In this case, the rate function approximately assumes the following

$$\begin{aligned} r_\xi(x) =& \theta_\xi(x) f_\xi(x)), \\ & \text{with} \\ f_\xi(x) =& \exp\left(-\beta\left(E_{a,\xi} + \alpha \Delta E_\xi(x)\right)\right) \end{aligned} \tag{5.10}$$

where $\beta = (k_{\mathrm{B}}T)^{-1}$ and $E_{a,\xi}$ is the barrier of the process ξ in the limit of an infinitely diluted crystal (or if x and $x + d_\xi$ are symmetry equivalent). The energy difference before and after the process (starting in x) is given by $\Delta E_\xi(x) = E(x + d_\xi) - E(x)$ and $E(x)$ is the energy in the state x due to the interaction of the ions. The prefactor $\theta_\xi(x)$ is assumed to have only a local dependency, i.e. it depends only on those entries of x which correspond to the sites which are in close vicinity to those sites for which occupations are altered by the process ξ. In the simplest case, this is just the Arrhenius prefactor times an indicator function which is one if the process ξ is possible and zero else. The factor α in Equation 5.10 describes the nature of the transition state in BEP. The symmetry of the diffusion jumps of Li$^+$ in graphite implies then that $\alpha = 1/2$. Coulomb interactions are pairwise, which means that

$$E(x) = x^T V x \tag{5.11}$$

where V with $V_{ij} = u(q_i - q_j)$ is a dense matrix with $u(q_i - q_j)$ being the interaction energy between two ions at the positions q_i and q_j of the i-th and j-th site for a homogeneous matrix material. Please note, that $u(*)$ already incorporates the Ewald summation for periodic boundary conditions. Existing approaches either employ some kind of physical or mathematical approximation [223] or employ “fast” potential evaluations like the Ewald summation. [221] Our approach instead will be completely approximation free and be based on update rules for $r_{\xi,n}$, which exploit the structure of Equation 5.10 and 5.11 and can be efficiently be executed on modern compute units. For this, we investigate how $\Delta E_\xi(x)$ evolves from step to step. We find that the energy differences in the $(n+1)$-th step can be written as $\Delta E_\xi(x_{n+1}) = E_\xi(x_n) + 2 d_\xi^T V \Delta d_{\chi_n}$, where χ_n is the process executed in the n-step. Given the value for f_ξ in the n-th kMC step, $f_{\xi,n}$, we can now pose the update rule

$$f_{\xi,n+1} = f_{\xi,n} g_{\xi,\chi_n}, \text{ with } g_{\xi,\chi} = \exp(-\beta d_\xi^T V d_\chi). \tag{5.12}$$

the factors $g_{\xi,\chi}$ can easily be precalculated. In the general case, they form a $N_p \times N_p$ matrix and thus would have a huge memory foodprint. For the considered case of periodic lattices, they are of convolution type, which, together with the locally of the processes, results in a memory consumption which is linear in the system size. Updating the rate values $r_{\xi,n+1}$ requires to updating the values for θ_ξ, which however is local and therefore needs only performed for very few processes. All non-local operations reduce to two vector-vector multiplications, one for updating the factor $f_{\xi,n+1}$ and one for multiplications of $f_{\xi,n+1}$ with θ_ξ. Since the number of processes is linear in the system size, this comes at linear costs. Furthermore, modern CPUs are very efficient in vector-vector multiplications and our implementation runs efficiently on a single core of a standard desktop CPU (see Appendix B). Especially compared to an Ewald summation in each step, this comes at much reduced costs and, by using a GPU, this could be further accelerated. What remains is the calculation of $g_{\xi,\chi}$ and $f_{\xi,0}$, for which we need to calculate $d_\xi^T V d_\chi$ and $d_\xi^T V x_0$. For this we employ lattice Ewald summation, see Appendix B

5.2.2 Ewald summation

Yet, we have to calculate the factor g_{ξ,χ_n} and our initial $f_{\xi,0}$, for which we need to calculate $d_\xi^T V d_\chi$ and $d_\xi^T V x_0$. Both can be calculated using an Ewald summation. For this, we represent the distances in the basis of the lattice vectors. Then our ions will resides on the sites of a simple cubic lattice, for which lattice Ewald summation is quasi exact and can be done using a Fast Fourier Transform [227].

5.3 The ckMC Algorithm and a Practical Guideline for Initializing the Simulation

This section presents an explanation of the necessary steps and procedures required for the initialization of a `kmos` run using the ckMC feature. However, the focus here lies only on the implemented ckMC feature, for a more general description of the `kmos` input structure the reader is referred to the manual.
As already mentioned in the previous sections we are usually dealing with a simple cubic (SC) lattice for which we have to set up the input structure. This lattice is usually characterized by a length L and a volume V which is given by L × L × L (L^3). Initialization is then achieved by placing ions in a random fashion onto the given lattice. One can also interpret the process of filling up the structure from the point of view of a fully packed system where randomly vacancies are created and distributed. Note that the lattice and the structure is usually imposed by the underlying system which is supposed to be studied by a kmos simulation. Parameters which are determined by the system are usually the distances to other sites, possible jumps or the barrier heights of the jump processes. For this work we only considered to types of systems, the toy system NiAl (which has already simple cubic crystal structure) and LiGIC. The latter has a hexagonal structure and therefore requires a mapping of all relevant processes onto the SC lattice (see section 5.5). After initialization of the system the total number of charges is then given by

$$N = N^+ + N^- \quad . \tag{5.13}$$

Here, N^+ denotes the total number of positive charges (q_i^+) and N^- being the number of negative charges. As a practical example, for our toy model system NiAl, the ions would be then divided into 50 $\%$ positive and negative charges, $N^+ = \frac{1}{2}N$ and $N^- = \frac{1}{2}N$. As we only allow positively charged species to move, q_i^+ (x,y,z) is the charge which would move freely in the medium. With other words, q_i^+ is the charge associated with cation i. Furthermore, q_i^- (x, y, z) is the charge of the anion i which is fixed at its position, or in other words which is not allowed to move. Of course one can easily also allow the negatively charged species to move freely through the system. The charge density ρ_i at position r induced by a moving particle is then given by:

$$\rho_i(r) = q_i\delta(r - r_0) \quad , \tag{5.14}$$

where the + sign on q^+ and also on N^+ in the following is dropped due to simplicity. As a consequence, the total charge density is then given by the sum over the single densities:

$$\rho(r) = \sum_{i=1}^{N} q_i\delta(r - r_i) \quad . \tag{5.15}$$

The total charge for the moving species is then obtained in the same fashion, $Q = \sum_{i=1}^{N} q_i$. In order to guarantee the electroneutrality of the system the following condition,here summing over all (cations $q_i = q_i^+$ and anions $q_i = q_i^-$ ions,is imposed:

$$\sum_{i=1}^{N} q_i p_i = 0 \quad . \tag{5.16}$$

Furthermore, the total density needs to obey at any time,

$$\rho_i = \frac{Q}{V} \quad . \tag{5.17}$$

Again, Q is the total charge and V is the volume of the cubic lattice. Knowing the position of each particle, and hence the charge density, the potential of the system then obeys a Poisson equation,

$$\mathit{\Delta}\varphi(r) = -\frac{\rho(r)}{\varepsilon_0\varepsilon_r} \tag{5.18}$$

which needs to be solved for the update steps. Here, the problem is that the coulomb interaction of the particle is long-range. As a consequence solving these equation in real space becomes unrealistic. Therefore, we make use of the Ewald method where the long range electrostatics are solved within Fourier space. Switching between real space and Fourier space is achieved by Fast Fourier Transform (FFT). Note that this is one of the most common procedures in order to deal with long-range electrostatic problems. [228] The potential then enters the rate equations of the kMC algorithm and one obtains the new jump processes of the next kMC step. Before we will simulate lithium intercalated in graphite it is reasonable to consider a much simpler test system in order to validate and benchmark the new implementation. Within this thesis we chose nickel aluminide (NiAl) in its simple cubic crystal structure. In our case the dielectric constant is of course also material specific.

5.3.1 Simple Cubic: Intrinsic NiAl Test Case

From a computational point of view, in particular so for the Ewald summation, it is most convenient to use a rather simple structure in order to map the charges onto a lattice. In our case we use a simple cubic lattice. In the following, the method will be discussed based on the usage of such a simple lattice. The charge carrier in our case will be ions, with the ionic motion under the influence of an electric field, that will describe then the ionic mobility or conductivity. In our system the moving charge carrier is positive, where the flux is created by external driving force *i.e.* the potential or field, that exactly counterbalances the diffusion flux. We will then obtain the mobilities and diffusivities as a result of propagating the system. As a first step and in order to validate our approach we chose NiAl to serve as a test system. NiAl is intrinsically simple cubic (SC). It is known to have mobile ions at high temperature with a hopping motion and this is known enough to allow us to validate the newly implemented charged feature. In this case the cation (Ni) will move and its possible jump processes are shown in Figure 5.1. [229] As already mentioned above the atom moving through a solid can be seen as performing jumps between minima of a potential energy landscape, where in crystalline solids these minima are represented by lattice sites or interstitial sites. Therefore, in order for a jump to occur it is necessary to have a certain amount of vacancies. The validation of the Ni mobility was performed then under the conditions, reported by Pelleg [229]. For more details the reader is referred to Appendix B. However, the important part here is to think of how do we map the charges and how is that treated from a mathematical point of view, first, and subsequently how will be that resolved within the propagation of the kMC framework. In a solid state diffusion process the species are moving with different rates. Locally, this will be altered by the surrounding neighbors, however, as we are dealing with charges long range interaction will then influence the global properties as well. However, let us make a step back and try to solve the problem of mapping the charged particles onto a lattice and solve how the external field will influence their mobility. The mapping itself is not the limiting part, despite the fact that we will need to ensure the electroneutrality of the system. According to Singer [230] the distribution of charges can be simplified in a few cases under the constraint of keeping the system neutral. Firstly, random arrays of charges can be distributed onto the lattice, with random distances between the two nearest charges. Another way is to use a lattice (of random or periodic structure) with a random distribution of charges, that does not need to the be alternated periodically. A third alternative would be a lattice (of random or periodic structure) with random charge strengths. The main part is to maintain the electroneutrality while distributing those charges. Having the charges as q_1, q_2,...q_n with their probabilities p_1, p_2,...p_n onto a lattice the electroneutrality is then given by the equation 5.16 [230]. For the NiAl system, the hopping motion is related to the cation that is diffusing (Ni) within the NixAl$_{1-x}$ single crystal. The typical Arrhenius plot of the Ni self-diffusion was for example measured by Frank *et al.* [229, 231] where Figure 5.2 shows the reported results as function of temperature and concentration. It should be noted that the results displayed in Figure 5.2 have been obtained with different methods at low temperature and high temperatures. The different results clearly show the complexity one has to deal with when performing

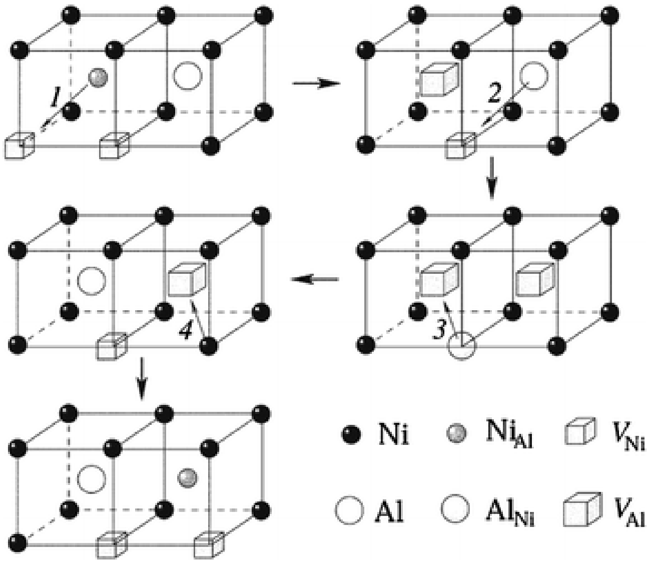

Figure 5.1 Schematic representation of possible pathways of the triple-defect diffusion fro Ni in NiAl. The sequences 1-4 indicate possible jumps. Permission from Springer and Elsevier, Peleg [229] and Frank *et al.* [231]..

experiments. Despite the different experimental methods and thus slightly different results a qualitative comparison with our theoretical simulations still provides an excellent benchmark for our implementation.

Input parameters for our test calculations have been obtained from Frank *et al.* [229,231]. To be specific we used the data provided for the the 48.7 at. % Ni reference as shown in Figure 5.2. We applied an activation barrier of 3 eV [229, 231]. More details in the input parameters can also be found within Appendix B.

The ions have been allowed to be mobile along all three directions of the cubic crystal. The simulations spanned the elevated temperature range of 1000-1700 K. As one can clearly see from Figure 5.3 we obtain excellent Arrhenius type behaviour for the ion mobility in the NiAl system and a qualitatively good agreement with the absolute experimental rates. Overall, this clearly demonstrates the validity and correctness of our charged kinetic Monte Carlo implementation. Having established and validated our approach we now move forward to lithium intercalated in graphite.

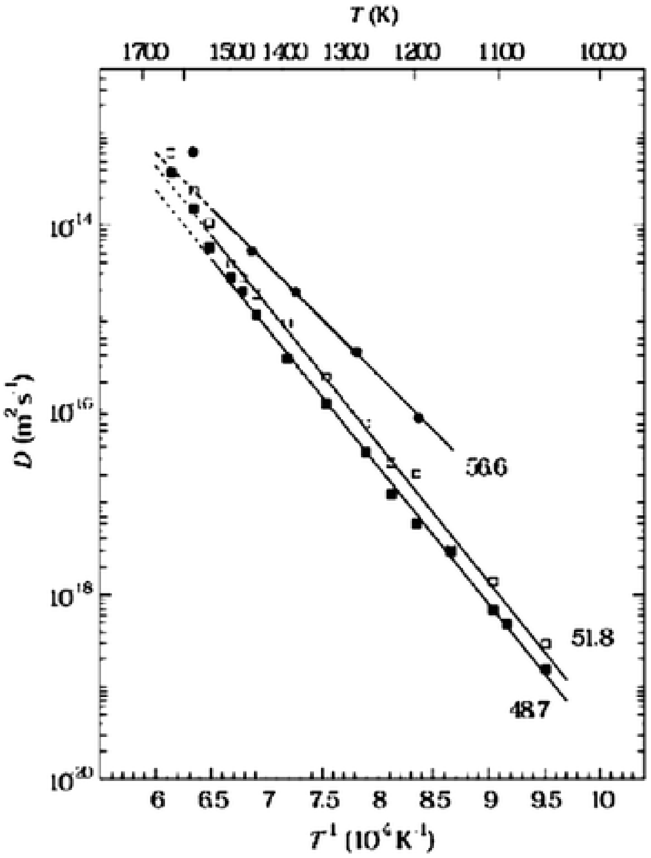

Figure 5.2 Arrhenius plots of Ni bulk self-diffusion in Ni$_x$Al$_{1-x}$ single crystal. The Ni content x is given in atom percent and depicted as number close to the corresponding Arrhenius plot. Permission from Springer and Elsevier, Pelleg [229] and Frank *et al.* [231].

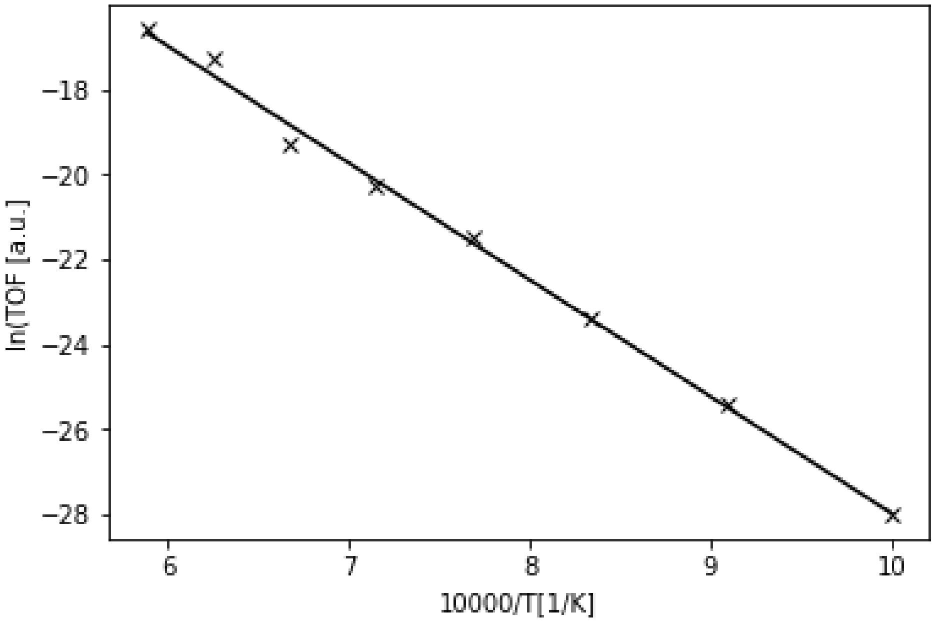

Figure 5.3 Arrhenius like plot of ion diffusion in the toy system NiAl. The Arrhenius plot has been obtained by using the charged kinetic Monte Carlo implementation. The plot was obtained for the vacancy concentration of 48.7 atom % Ni.

5.4 More on Diffusivity and Ionic Conductivity of Lithium

When taking into account the intercalation phenomena, the exchange of Li^+ between the electrode and the electrolyte is a key factor of this process.In principle a simulation would require to describe the electrolyte as a Li^+ reservoir with a fixed chemical potential that exchanges ions with the electrode material. To address this, a kMC model must include the diffusion of the ions outside and inside the host for being able to mimic the starting of the intercalation, *i.e.* such as from the surface of the electrode. Conceptually, this sounds simple. However, despite years of research, the exact process of how the first lithium atom intercalates into graphite is still unknown. Additionally, there would be the problem that a liquid electrolyte would best be described with an off-lattice kMC approach.To circumvent this problem we decided to start the cKMC model with lithium ions being already randomly distributed over the lattice.

In fact, within solid state materials, diffusion is governed by random jumps of atoms or ions, which of course also results in exchange with their next neighbors. Within the LIB, the diffusivity is reported as a function of intercalation or electrode voltage. [232] Ideally, it would be desirable to simulate the full range of intercalation and to investigate how intercalation evolves. In order to address this complex part we first address the two possible extremes. Further, despite focusing on the validation of the reference system LiC_6 the diffusion in Li_2C_{216} will also be reported. In general, vacancy/defects play a central role in ion diffusion. The vacancy/defects mediated mechanism are common in this kind of materials, however the non-vacancy/non-defect mediated ones can occur as well. Li-ions diffuse mainly by an interstitial mechanism due to the small radius of the lithium. [232] However, the motion of the lithium ions is strongly impeded by the potential created by the presence of neighboring ions. In this case, the diffusion can be the rate-determining process compared to electronic conduction in an electrochemical reaction. Diffusion within the `kmos` framework is treated by applying an external field, that will allow the description of the diffusivity as a function of the external field that can be varied and which mimics ideally the diffusivities as in the experimental measurements, as function of the intercalation or the electrode voltage. [232] The kinetics of diffusion processes are temperature dependent and expected to follow a typical Arrhenius type relationship. This is another key aspect why a validation is necessary and as this can be strongly affected by defects. In the case of the graphite anode, a Li-ion can fairly easily diffuse parallel to the graphene layers while diffusion perpendicular to the graphene layers has a significantly larger barrier and is thus not likely to occur. In order to understand the diffusion of a Li-ion it is important to consider the crystal structure as well as the surrounding potential. One needs to be careful when describing the motion of Li-ions, and consider the relationship between diffusivity and ionic conductivity. Motion of the lithium ions gives rise to ionic conduction under external electrical potential. The charged particles, in this case the lithium ions, can pass through a media under two driving forces: an externally applied electric field or a concentration gradient. The mobility (u_i) of ions represents the degree of ease with which ions pass through the media under a concentration gradient. Mobility, diffusivity and ionic conductivity are all related. The relationship between mobility and diffusivity can be obtained by considering the drift velocity (v_i) in terms of mobility (u_i) under both an externally applied electric field and a concentration gradient. [232] The Nerst-Planck equation implies that mobility and diffusivity are interchangeable and uses the definition of current density induced by ionic flux. In fact, if the contribution of ionic conductivity to the total conductivity (electronic conductivity + ionic conductivity) is known, the diffusivity can be deduced and vice-versa. Normally, diffusivity in an electrode materials is hard to measure from an experimental point of view. On the other side, ionic conductivity is easier to measure. As a consequence the diffusivity, in principle, can be deduced from such measurements. However, despite this general correspondence both are not directly related in practice. Cyclic Voltammetry (CV), Galvanostatic Intermittent Titration Technique (GITT), Potentiostatic Intermittent Titration Technique (PITT) and Electrochemical Impedance Spectroscopy (EIS) usually measure the variation of ionic current under an applied voltage in order to calculate diffusivity. [233] From these one usually just obtains an overall diffusivity. Therefore, having theoretical support which allows independent diffusivities (distinguishing between directions, and different jump processes) becomes even more relevant. [232]

On top, the various phase changes over the range of SOCs Li-GIC makes the diffusivities of Li ions even more complicated, since this can introduce disorder into the originally ordered structure. [14]This is observed within the modelling by the variation of the so called vacancy concentration or also known as empty sites. Hence this will describe different state of charge.

5.5 Mapping the Hexagonal Graphite onto a Cubic Lattice

From a theoretical point of view the most convenient way in order to solve the mobility of a charged particle, in this case a positive ion under an external field, is when there is only one particle that moves. Of course, in a real system that is never the case; however, if we think of the graphite structure, entirely empty but for a single lithium/ion inserted within the graphene layers, is the closest scenario. Relatively, this would also be the case for the low state of charge *i.e.* as LiC_{108} or Li_2C_{216}, which will correspond to 5 $\%$ SOC. Simply, this situation can be depicted as only one lithium that is moving ideally within an empty layer as it is shown in Figure. 5.4.

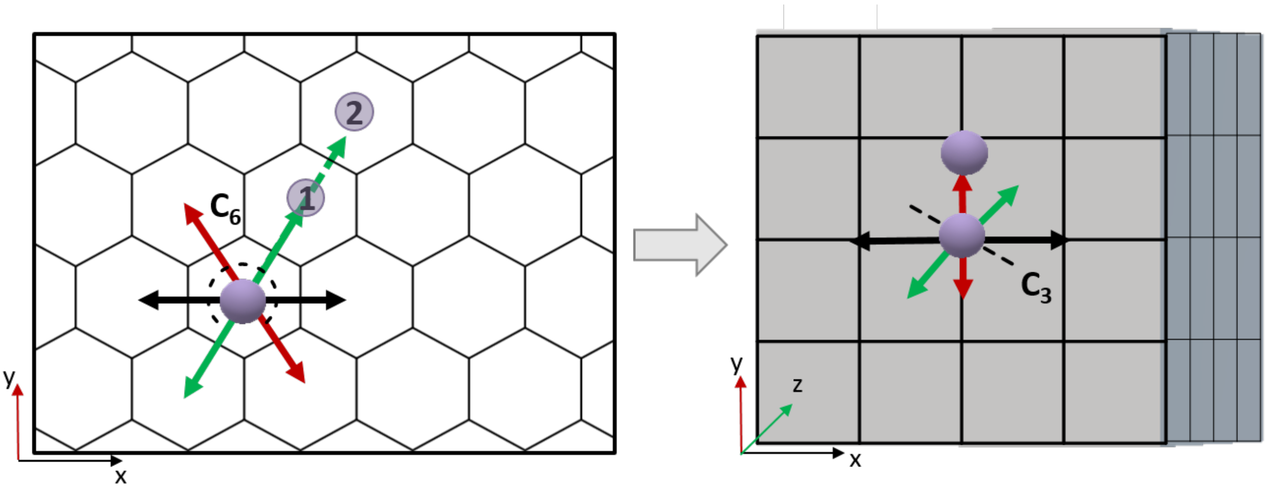

Figure 5.4 Left panel: representation of the lithium atom on top of one graphene layer within the x/y plane. The arrows indicate the direction of the jumps within the plane, the z-direction is not represented. Right panel: a simple cubic representation in 3D with the superimposed x/y plane on top, to identify the sites that were translated from the hexagonal symmetry.

The influence not only of the charged particles but also of the screening of the materials is taken into account through the dielectric constant. As a good starting point for our calculation we used values obtained from Bessler *et al.* [234]. Bessler and co-authors managed to measure the dielectric response within the bilayer graphene which can be considered to be a good approximation for the Li_2C_{216} [234]. The value is given by 6 C^2/Nm^2. Here, the lithium ion is left free to move within the framework of the sheet as depicted in Figure 5.4. The jumping vectors are identified with motion to the next neighbour (NN) empty site, or the 2 NN, corresponding to jump distances $j_1 = 2.46$ Å and $j_2 = 4.30$ Å .

Another important aspect which needs to be taken into account is the treatment of the prefactor. The geometrical factor of the structure was included within the treatment.For our kMC simulation we used a lithium hopping barrier of 0.503 eV which was obtained from DFTB simulations c.f. chapter 3. [112] Note that by this we establish for the first time a multiscale modeling approach for mesoscopic Li diffusion in graphite where the input parameter of first-principles calculations have been used to feed a more coarse-grained kMC approach. Again, comparison with experiment further helps us to validate our theoretical approach. For this purpose, we list our obtained diffusion coefficients together with values found in literature (Table 5.1). As one can clearly see, our obtained diffusion coefficients are in good agreement with the listed experimental values. Slight differences can be explained by impurities or other defects as these effects are not capture by our model. However, this clearly demonstrates the capabilities of our implementation.

Table 5.1 Calculated diffusion coefficients obtained from cKMC are compared with diffusion coeffiecients obtained form experiment. Literature values have been experimentally determined by Hall measurements Kühne *et al.* [54]. These specific values are for Li intercalation in bilayer graphene $C_6Li_{2y}C_6$.

$D_{Li_2C_{216}}[cm^2/s]$	$D[cm^2/s]$
$4 \cdot 10^{-6}$	$10 - 70 \cdot 10^{-6}$
$0.7 \cdot 10^{-6}$	$1 \cdot 10^{-6}$

5.5.1 Modelling Ion Diffusion and Mapping of LiC_6

Similar to the previous case, LiC_6 will be treated in the following by a ckMC description. Note, that LiC_6 is now assumed to be the case of full intercalation which corresponds to high SOC.

Naturally, the lithium mobility depends on the number of introduced vacancies. This is easy to explain as an empty site is necessary so that a successful Li jump can occur (Figure 5.5).

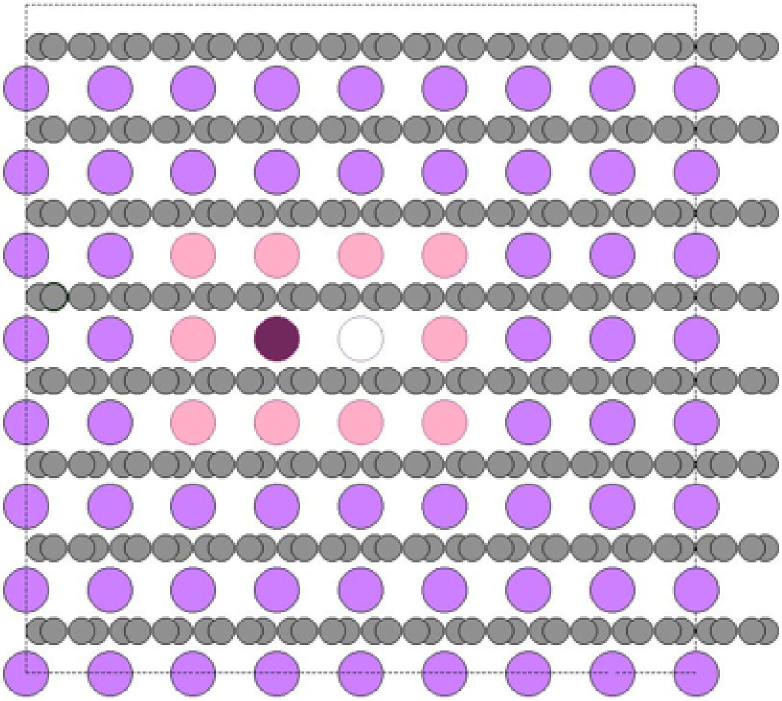

Figure 5.5 Representation of the simple cubic lattice. Lithium atoms/ions are represented by the violet dots. The dark one is the ion that is considered to start moving. The white sphere is the nearest empty site. Rosa are the next nearest neighbor ones that will count for the coulomb interaction. Diffusion across the layers is not allowed. The unit cell is indicated by a black dashed line.

In general, the process of a moving a charged particle will have immediately an influence on the other particles as well. On top, if the electric field is applied, the ion mobility is further influenced. This effect then needs to be evaluated and adapted (*on the fly (otf)*) if the system is propagated. The influence of the overall material itself is introduced within the model through the dielectric constant and the occupancy will be used to control the number of the ions. For more details the reader is referred to Appendix B. We are using two parameters, $j_1 = 2.46$ Å and $j_2 = 4.30$ Å are distance parameters used to control the allowed distances of a jump and to identify the possibilities of the jumps. Possible jump processes are shown in Figure 5.6. The exact geometrical meaning of j_1 and j_2 is depicted in Figure 5.4. Here, the index 1 and 2 are site labels, with other words j_1 and j_2 are possible jumps that can occur during the simulation. Note, that these are the same settings as for the previous case of the low state of charge. This is not surprising at all as the structure is the same, only the number of intercalated lithium ions is different. For the treatment of the dielectric properties we used a value of 11 C^2/Nm^2 for the dielectric constant of the system. [235] This value is slightly higher than for the low state of charge system since more lithium ions in the structure result in an increased screening effect.

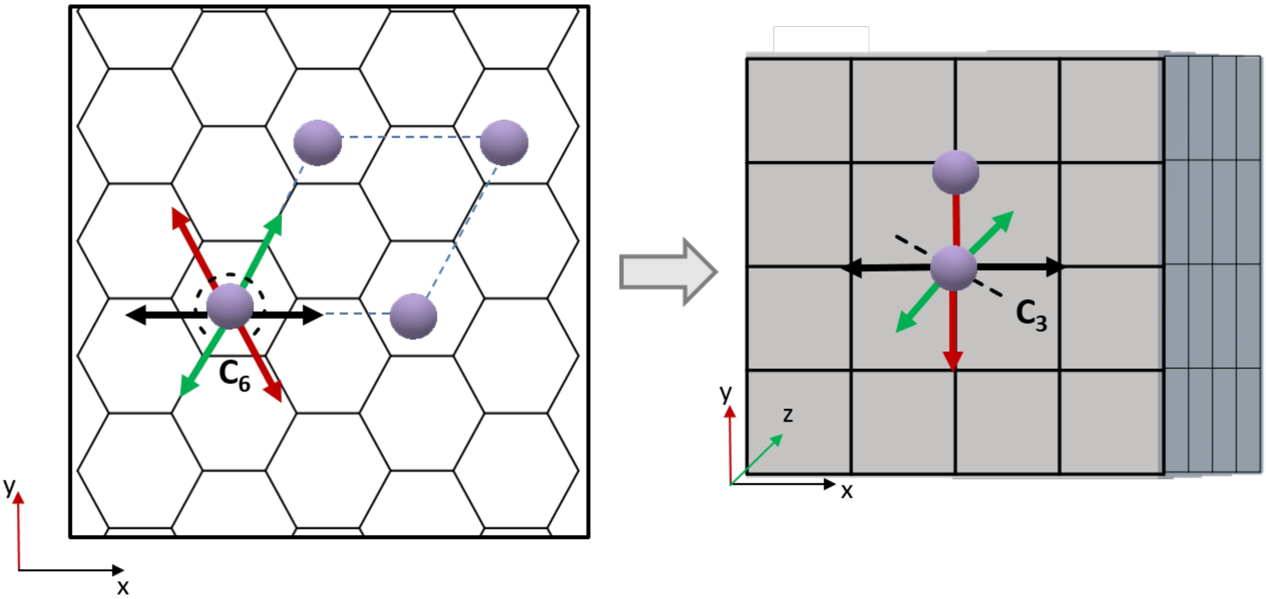

Figure 5.6 Left panel: representation of the lithium atom on top of one graphene layer within the x/y plane. The arrows indicate the direction of the jumps within the plane, the z-direction is not represented. Right panel: a simple cubic representation in 3D with the superimposed x/y plane on top, to identify the sites that were translated from the hexagonal symmetry. Jump processes which would occur along hexagonal lattice directions are no mapped onto a cubic lattice.

For our simulation we used the computed activation barrier height of 0.503 eV. Table 5.2 lists the obtained diffusion coefficients for different lithium vacancy concentrations. As one can clearly see, the lithium vacancy concentration directly affects the diffusion. If more vacancies are present the diffusion coefficient increases as more jumps can occur. It has to be noted, though, that the change in the diffusion constant is not simply proportional to the increase in vacancy concentration. Further, if one compares the obtained values with the values which are listed in Table 5.1 one directly sees that the values for LiC_6 are several orders of magnitude lower. Again, this can be easily explained by the number of jumps which are possible. Within LiC_6 less jumps can occur since lithium ions occupy most lattice. It should be emphasized that this results confirms the correctness of the ckMC implementation as the less mobile lithium ions of a packed structure (here LiC_6) lead to a significantly lower diffusion coefficient which will be validated experimentally in the following sections.

$D_{LiC_6} [cm^2/s]$	vacancy concentration %
$4 \cdot 10^{-16}$	[0.003]
$7 \cdot 10^{-15}$	[0.012]

Table 5.2 Calculated diffusion coefficients for different lithium vacancy concentrations in LiC_6.

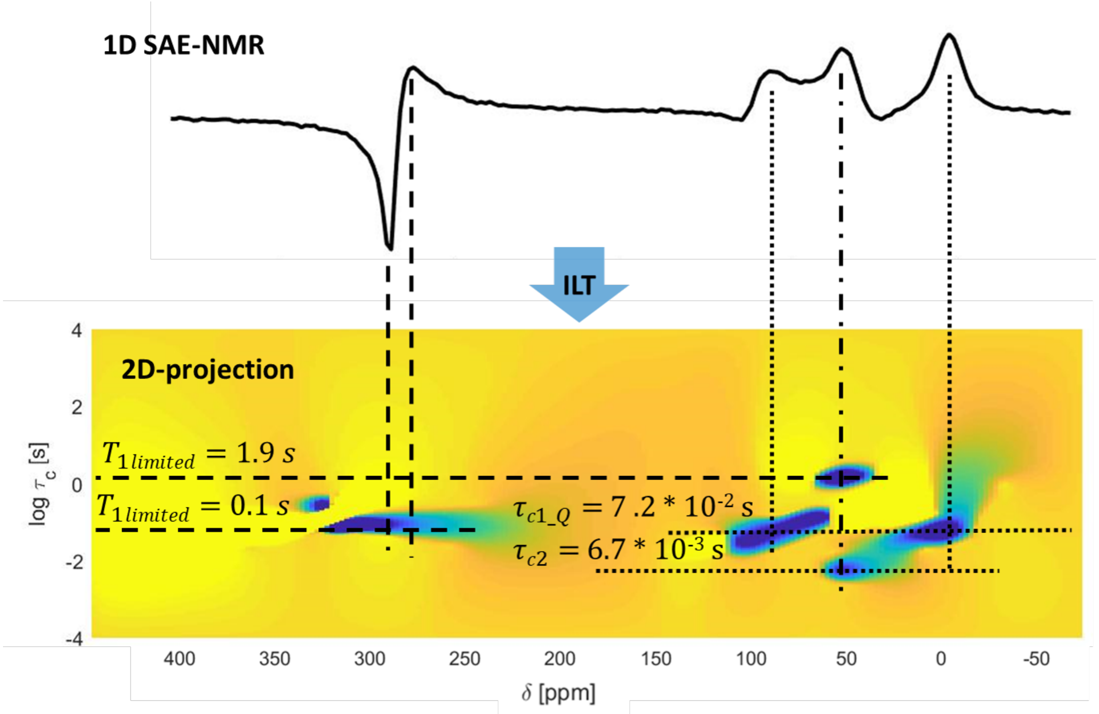

Figure 5.7 Upper panel: the representation of the ^{7}Li static NMR, obtained under the spin alignment echo (SAE) pulse. Lower panel: The inverse Laplace transformation (ILT) of ^{7}Li SAE spectra recorded at room temperature for the mechanical intercalated LiC$_6$ within the HOPG, via the infiltration technique. The underlying correlation times are associated with different relaxation processes and correspondingly different diffusion processes.

5.6 ILT-SAE on Lithium intercalated HOPG

The LiC$_6$ sample was prepared using an infiltration technique as described and characterized in chapter 4. All the ^{7}Li NMR spectra were acquired with a Bruker BioSpin spectrometer Avance III HD 600 XWB MHx at B$_0$ = 14.1 T (^{7}Li Larmor frequency of 233.3 MHz). The spectrometer was equipped with a Bruker DIFF50 probe-head. For the spin alignment echo, the SAE-NMR was recorded with the Jeener-Broekaert pulse sequence $\beta_1 - t_p - \beta_2 - t_m - \beta_3 - t_d$. Here β represents radio frequency pulses, t_p is the evolution time, t_m the mixing time and t_d the detection transient. [164] For the determination of T_1 or spin-lattice relaxation, the inversion recovery (ISR) pulse was used. For more details of this method the reader is referred to the theory part in chapter 3. The SAE and ISR were analyzed using an inverse Laplace transformation by closely following the procedure described by Granwehr *et al.* 3.3 [152]. The extracted correlation times can be related to the diffusion coefficient by considering the Einstein-Smoluchovsky relation, [63]

$$D_{dD} = \frac{a^2}{2d \cdot \tau} \quad . \tag{5.19}$$

As shown in reference [63] τ can be assumed to be equal to τ_c, where a is the mean jump distance of ≈ 3 Å and d is the dimensionality of the diffusion process (d=2 if it is a restricted and d=3 if it is a non restricted motion). Note that the mean jump distance was obtained from literature. [63]

For τ_c one can write,

$$\tau_c^{-1} \approx \tau^{-1} \approx \tau_0^{-1} exp^{\frac{-E_a}{k_B}T} \quad , \tag{5.20}$$

where the τ_c^{-1} is extracted in this case from SAE.τ_0^{-1} is the pre-exponential factor. [63]

In Figure 5.7 we show the obtained SAE with correlation times which where obtained by ILT. It is important to realize that not all obtained correlation times can be attributed to diffusion processes. Here, T_1

from Figure 5.7, can be attributed to spin lattice relaxation processes, hence, it will not be considered in the following analysis. Table 5.1 then lists the calculated diffusion coefficients obtained from the assigned correlation times.

$D_{\tau_{c1Q}}$	$4.5 \cdot 10^{-16} cm^2/s$
$D_{\tau_{c2}}$	$1.4 \cdot 10^{-15} cm^2/s$

Table 5.3 Diffusion coefficients obtained from the SPE experiment. The diffusion coefficients have been calculated using equation 5.19. Inverse Laplace Transformation (ILT) was used to obtain the correlation times.

The fact that we are actually observing a signal which can be attributed to a diffusion process is at first quite surprising. If we think of a jump process within an ideal LiC_6 system, the moving lithium ion should on average see the same environment, if thinking of the local electric field. In other words the hopping lithium ion has the same local environment before and after the jump. It only interchanges its positions with a lithium vacancy. As a consequence one would assume that no signal is observable. However, as our experiment shows, we are clearly obtaining correlation times which can be attributed to diffusion processes. On the other side, one could argue that the jump processes change the chemical environment of the local environment. Hence, the signal could originate from the lithium ions which are in close proximity to the lithium ion which performs a jump process. Up to now, it is not fully clear which exact process we are looking at, leaving room for interpretation. More investigations are needed in order to shed more light on the relevant processes, however taking into account the fully intercalated structure that is the only interpretation.

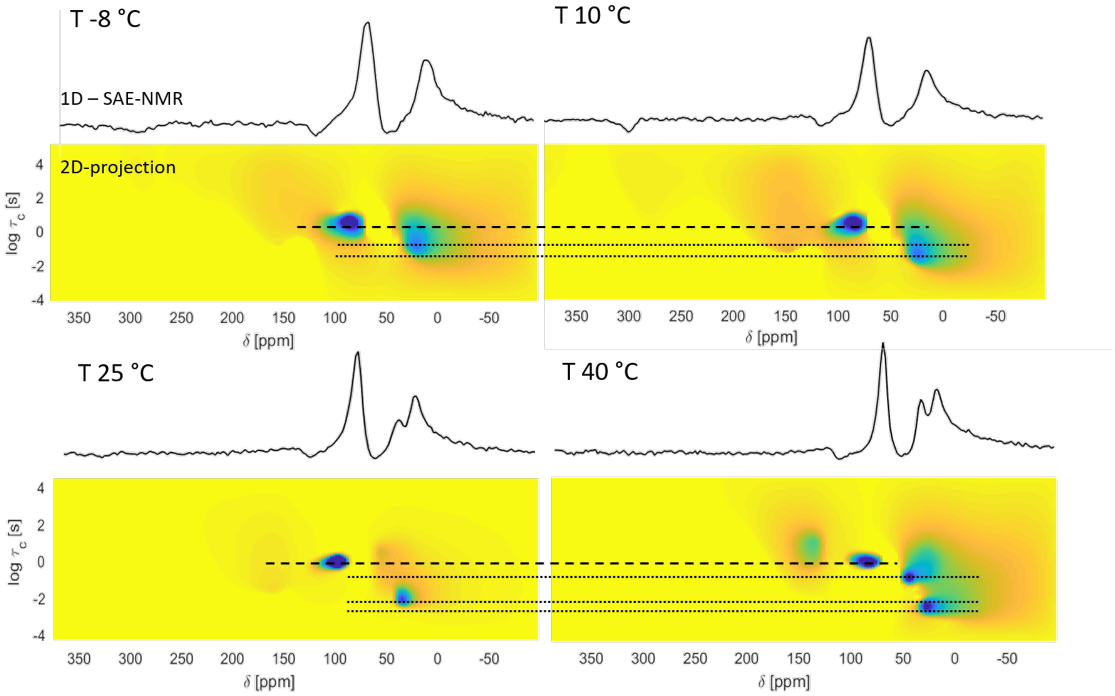

Figure 5.8 The representation of the ^{7}Li static NMR (black spectra), obtained under the spin alignment echo (SAE) pulse with the respective inversion Laplace transformation (ILT) of ^{7}Li SAE spectra below. The system under consideration is the mechanical intercalated LiC_6 within the HOPG framework. The infiltration technique was used. The measurements have been conducted for four different temperatures as indicated above. The underlying correlation times are associated with different relaxation processes and subsequently different diffusion processes.

To be able to cross validate our single-spectrum approach with ckMC, we recorded SAE-NMR as a function of different temperatures. From this, one can extract activation barrier assuming an Arrhenius like temperature dependence. Figure 5.8 shows results for the temperature dependent SAE measurements from -8 ° C to 40 ° C and the corresponding ILT-SAE below. The first feature indicated by the black big dashed line 45 ppm that is present in all four graphs are the T_1 limited relaxation processes. Those are not taken into account as correlation times which can be related with diffusivities. The appearance of additional features at room temperature (25 ° C) and 40 ° C is given from the overall broad contribution underneath the spectra which is discussed in more detail in part 4. The maximum of the second feature 45 ppm is used to construct the Arrhenius plot (Figure 5.9) of the system. To identify the limit on the T_1 relaxation the ILT was applied with the extraction of the T_1 inversion limit for all the samples systematically.

As one can see from Figure 5.9 we clearly obtain an Arrhenius like behaviour. Note that the data points in the plot are related to the maximum of the obtained signals. The bars indicate the range of the obtained correlation times from the width of the corresponding distribution. By analysing the slope of the fitted line in figure 5.9 one can extract the activation barrier for the diffusion process. In this case the barrier is measured to be $0.539 \pm 0.037\ eV$. This is consistent with the activation barrier predicted by the DFTB simulations (0.503 eV) and for a certain vacancy with cKMC (0.604 eV).

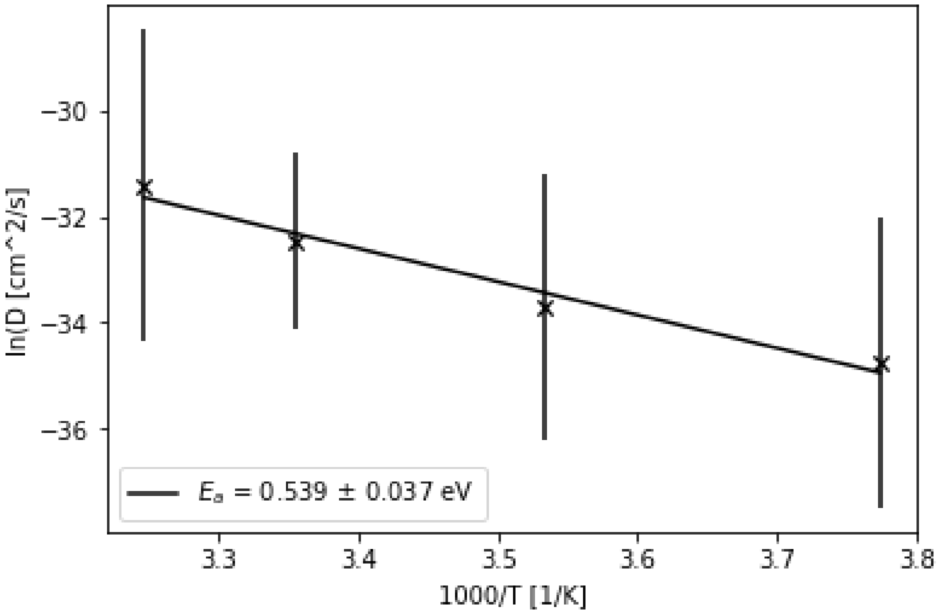

Figure 5.9 An Arrhenius like behaviour for the temperature dependent SAE-ILT. The range which is given as additional bars are taken from the upper and lower correlation time distribution post inversion. The activation barrier of $0.539 \pm 0.037\ eV$ is consistent with the literature [63].

5.7 Comparison of ILT-SAE and cKMC

In the previous section the ILT-SAE and cKMC were described independently of each other. The validation first was done using the experimental data of the fully intercalated LiC_6 spectrum. The values obtained were extracted from the distribution of the correlation time after the inversion, and through equation 5.19 converted in diffusion coefficients, with $a = 3$ Åand $d = 2$. Table 5.4 compares the results from the kMC calculations with the experimentally obtained diffusion coefficients calculated from the NMR correlations times. Also listed is the lithium vacancy concentration used within the kMC runs.

We see an exact match between the one extracted from cKMC, with the vacancy concentration tending to zero, and with the first value listed in table 5.4. To recall, the lithium intercalated within the HOPG should be almost perfect which means, from a theoretical point of view, the vacancy concentration within the system should tend to be zero. Indeed, thinking of the LiC_6 as a fully packed system with a few lithium atoms missing from the intercalation, will lead to a surprisingly perfect match. However, we should not forget the discussion on the overintercalation. Here, the specific chemical shifts (45ppm) for the LiC_6 are then used to know that we are looking at that exact phase. The T_1 limitation, does also exclude the relaxation related to the spin-lattice relaxation, so in this case the correlation time we are comparing is related indeed to a diffusion process. From theory, we observe that the system with the nominal vacancy concentration of 0.003% is the one closest to the diffusion process extracted for the correlation times of the quadrupoles and the one at 0.012 to the correlation time extracted from the main central peak. Since we cannot measure the concentration of the vacancy experimentally, we can just speculate. However, the perfect match between both theory and experiment clearly indicates that only a very low number of vacancies exist in the sample and are responsible for lithium jumps to occur. Note, that this clearly shows how helpful our kMC analysis is for interpretation of our experiment.

$D_{cKMC}[cm^2/s]$	theoretical vacancy concentration %	$D_{ILT-SAE}[cm^2/s]$
$4 \cdot 10^{-16}$	[0.003]	$4 \cdot 10^{-16}$
$7 \cdot 10^{-15}$	[0.012]	$1 \cdot 10^{-15}$

Table 5.4 On the left the diffusion coefficients obtained from our cKMC calculations are listed. The middle column shows the theoretical vacancy concentration which where used for initializing the kMC runs. On the right the experimentally obtained diffusion coeffiecents are shown. Both values have been obtained from ILT-SAE

From this perspective so far the match between experiment and theory was almost perfect, however the validation was extended additionally to the cross-checking of the diffusivity in function of the temperature that can be analyzed through the Arrhenius behaviour. In this case for the comparison the activation barrier was taken into account. Unfortunately, using a lithium vacancy concentration of 0.003% and 0.012% for our simulations results in a non Arrhenius like behaviour. At this low vacancy concentrations the Arrhenius behaviour is probably hindered. However, once we go up to 0.1% we obtain an excellent Arrhenius relationship (Figure 5.11). Nevertheless, this raises ultimately two questions. First, why does the obtained activation barrier of 0.604 eV, from the kMC run, not align with the activation barrier from DFTB and second how does the diffusion coefficient depend on the vacancy concentration? The first question is easy to answer, as the DFTB simulations do not fully account for long range static correlation which is better captured by the ckMC approach. Hence, in the obtained activation barrier of 0.604 eV we additionally see those effects. Nevertheless, the obtained activation barrier of 0.604 eV is still in good agreement with the activation barrier which was obtained from the NMR experiment.

To shed more light on the second question we show in Figure 5.10 the diffusion coefficients with respect to lithium vacancy concentration. For this analysis we used again the same input parameters as for the previous ckMC calculations. The vacancy concentration was varried between 0.0 and 0.9 %. The obtained graph directly shows how sensitive the diffusion coefficient is. Over the full range the diffusion coefficient varies quite significantly. From the cKMC we took into account just the diffusion in terms of jumps, for the reference. Yet at point this can be extended to any vacancy concentration. And to investigate more complex diffusion phenomena.

Here, we present a fundamental understanding for the scattering of this values with a synergistic approach between experiment and theory. This lies intrinsically in the distribution and concentration of the lithium vacancies or defects. In fact defining just the basic empty lithium position in an ideal LiC_6-HOPG as a simple lithium defect, and performing our simulation, by varying only this parameter, we observe a huge variation. It might be obvious, but a four orders of magnitude difference included just in a few percentages of vacancy within the ideal system is important if we have to think about battery performance prediction or a battery management system. As we mentioned above we are aware of not performing for this presented results any real prediction, since will go beyond our validation and investigation of the upper boundary limit of the system.

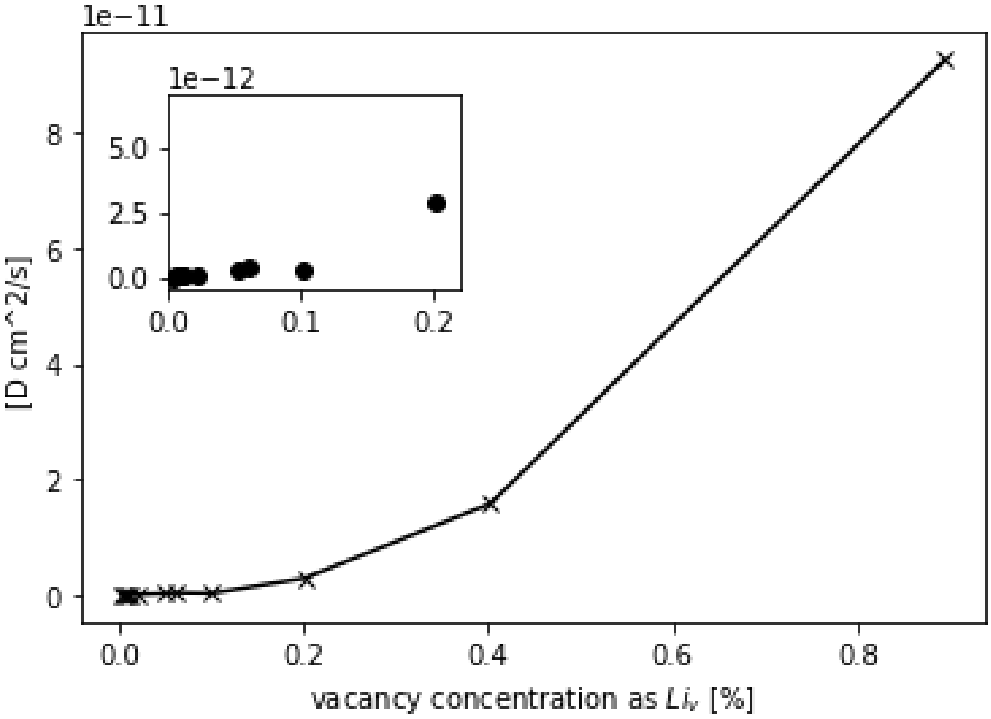

Figure 5.10 Shows the diffusion coefficient of the LiC_6 as function of vacancy concentration, defined as empty lithium $[Li_v]$ within the cell. These results have been obtain from the previously described ckMC approach. Same settings apply as described previously in section 5.5.1.

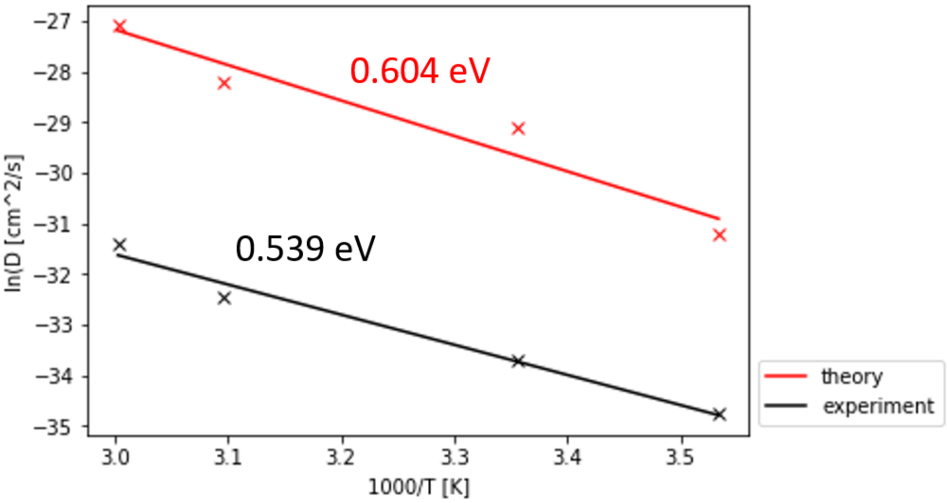

Figure 5.11 Arrhenius like behaviour for the diffusion coefficients for the lithium ion in LiC_6. The black line shows the data extracted from the ^{7}Li ILT-SAE NMR at different temperatures. The red one is the one extracted from cKMC at 0.1 % vacancy concentration.

6 Summary, Conclusions and Outlook

Within this work, theoretical methods were successfully combined with experimental investigation in order to address complicated diffusion phenomena not only within battery materials but also within solid-state systems in general. To be specific, the diffusion of Li intercalated in HOPG was investigated using state of the art spin alignment echo techniques in combination with inverse Laplace transformation (ILT-SAE) serving as a tool for signal analysis. The experimental measurements have been then supported by kinetic Monte Carlo simulations by applying the newly implemented cKMC approach within the *kmos* code. Within this approach, the ILT-SAE allows us to identify correlation times using an Einstein-Smoluchowski approximation. These correlation times then can be related to diffusion coefficients. It could be demonstrated that Li intercalated in HOPG serves as an excellent candidate for being a reference system in order to validate the ILT-SAE and the newly implemented *kmos* feature. Further in order to shed more light on the detailed mechanism within the industrially used graphite powder, more defects and disorder will need to be introduced as a next logical step. Moreover, the impact of the grain boundaries and particle size needs to be considered as well in order to slowly advance to a complete picture. This clearly demonstrates how important the combination between experiment and theory actually is and specifically how valuable the developed ckMC approach is for investigating diffusion phenomena. The key feature is that it allow us to study the influence of these material characteristics from a well-defined first principles starting point. Comparing with experiment then directly allows for a more detailed interpretation of the gathered experimental data sets. Within this work it could already be shown that the vacancy concentration has a huge effect on the diffusion coefficient which ultimately raises the question if the diffusion coefficient can be used as a reliable parameter in order to predict the performance or the lifetimes of LIBs. Clearly, the discussion above as well as the discussions throughout this thesis directly reflect how challenging it is to measure and to distinguish different self diffusion processes. However, it is necessary and mandatory to continue within this direction of research as identifying possible limiting factor can lead to a more reliable prediction of battery performance. The tools applied in this thesis, clearly show the validity of both independent techniques and demonstrate the reliability of computer generated diffusion values. The complexity of disentangling the single contributions within the experimental measurements can be circumvented by applying our ckMC approach. On top, the applied external field will allow in a shorter time to simulate extreme conditions and identify their effect on the mobility. Further it will help to correlate experimental observed properties to the atomistic process. Despite the fact that the main scope of this thesis is the investigation of the ion mobility for different state of charge within LiGIC compounds, also patterns of overintercalated lithium (beyond LiC_6) could be identified while preparing the reference system (LiC_6) for the NMR-investigation. This was then rationalized and investigated in more detail. By doing it could be finally confirmed that overintercalation is indeed happening even at moderate synthesis conditions. This result shows that overlithiation has to be considered while addressing complex concepts such as re-intercalation, lithium plating and of course intercalation processes especially under the extreme fast-charging conditions. The findings reported here will further help to contribute to the development of better battery management with a better prediction and estimation of the *a priori* performance and duration of the graphite anodes, as well as of the full battery cells.

A Appendix I

A.1 Density Functional Theory

Variational principle of the density states that only the ground state density $n(1)$ minimizes the energy of the system,

$$E^{(1)}\left[n(1)\right] \leq E^{(2)}\left[n(2)\right] \quad . \tag{A.1}$$

Within KS-DFT the ground state is described by a single Slater determinant

$$\Theta_S = \frac{1}{\sqrt{N!}} \begin{vmatrix} \psi_1(\vec{x}_1) & \psi_2(\vec{x}_1) & ... & \psi_N(\vec{x}_1) \\ \psi_1(\vec{x}_2) & \psi_2(\vec{x}_2) & ... & \psi_N(\vec{x}_2) \\ \vdots & \vdots & & \\ \psi_1(\vec{x}_N) & \psi_2(\vec{x}_N) & ... & \psi_N(\vec{x}_N) \end{vmatrix} \quad . \tag{A.2}$$

Here, the spin orbitals are given by following single-particle like quations (Kohn-Sham equations),

$$\hat{f}_{KS}\psi_i = \varepsilon_i\psi_i \quad . \tag{A.3}$$

The one electron Kohn-Sham operator $\hat{f}_{KS}$ has the follwing form:

$$\hat{f}_{KS} = -\frac{1}{2}\nabla^2 + V_S(\vec{r}) \quad , \tag{A.4}$$

where $V_S(\vec{r})$ is the potential which acts on the particles. The so called Kohn-Sham orbitals can be used to obtain the total density according to.

$$\rho_o(\vec{r}) = \sum_i^N |\psi_i(\vec{r})|^2 \quad . \tag{A.5}$$

The kinetic energy of an single-slater determinant of a non-interacting electron system than can be calculated as

$$T_s = -\frac{1}{2}\sum_i^N \langle\psi_i|\nabla_i^2|\psi_i\rangle \quad . \tag{A.6}$$

$F[\rho(\vec{r})]$ is an unknown functional, however, it can be written in following the general form

$$F[\rho(\vec{r})] = T_s[\rho(\vec{r})] + J[\rho(\vec{r})] + E_{XC}[\rho(\vec{r})] \quad , \tag{A.7}$$

where $J[\rho(\vec{r})]$ describes the classical coulomb interaction. The non-classical exchange and correlation interaction are included in $E_{XC}[\rho(\vec{r})]$ with

$$E_{XC}[\rho(\vec{r})] = (T[\rho] - T_s[\rho]) + (E_{ee}[\rho] - J[\rho]) = T_C[\rho] + E_{ncl}[\rho] \quad . \tag{A.8}$$

Here, $T[\rho]$ is the kinetic energy of the true interaction system.

A.2 Hartree-Fock

In order to distinguish Kohn-Sham orbitals from ther Hartree-fock counterpart the Hartree-fock single-particle states are denoted by χ_i. The kinetic energy can be obtained by

$$T_{HF} = -\frac{1}{2}\sum_{i}^{N}\langle\chi_i|\nabla^2|\chi_i\rangle \quad . \tag{A.9}$$

As already mentioned for DFT, the variational principle can be also applied to the Hatree-Fock energy. The true ground state energy then can be obtained by minimization,

$$E_{HF} = \min_{\phi_{SD}\rightarrow N}\langle\phi_{SD}|\hat{T} + \hat{V_{Ne}} + \hat{V_{ee}}|\phi_{SD}\rangle \tag{A.10}$$

Note that ϕ_{SD} denotes the total Hartee-Fock wavefunctions in form of a Slater determinant (SD). The Hartee-Fock Hamiltonian can be written as

$$\hat{H}_S = -\frac{1}{2}\sum_{i}^{N}\nabla_i^2 + \sum_{i}^{N}V_S(\vec{r_i}) \quad . \tag{A.11}$$

Note that $V_S(\vec{r_i})$ has to be distinguished from its DFT counterpart. Within Hartree-Fock only exchange contributions are included whereas correlation contributions are in general not described by this level of theory.

B Appendix II

B.1 NiAl: Test and Input Parameters

For the simulation we chose a lattice size with dimension $32 \times 32 \times 32$, with an occupation parameter of 0.487. The latter corresponds to the control of the concentration of the ions. A hopping activation barrier of E_a = 3.0 eV was employed. The dielectric constant was sampled and 30 [C^2/Nm^2] was used for the simulation. The electric field was set to $1e^8$ [V/m].

B.1.1

The diffusion can be described by following equation,

$$J = -D_i \nabla C \quad . \tag{B.1}$$

where J is the diffusion flux of the particles and C the concentration of charged particles or better their number density. The negative sign indicates the opposite directions of diffusion flux and concentration gradient. Nabla operator acts on a scalar concentration field C(x,y,z,t) and produces the concentration gradient field ∇C.

Ohm's law, ohm's transport of electric charge (for us ions), under the influence of the electric field (ionic conductivity) can be expressed as

$$j_e \equiv -\sigma_d c \cdot E \quad . \tag{B.2}$$

With setting $E = -\nabla V$ on obtains,

$$Je \equiv -\sigma \cdot \nabla V \quad . \tag{B.3}$$

where Je is the electric current density, V the electrostatic potential and σ the conductivity. If we have a certain number of the particles with charge q_i and their mobility (μ_i) and N_i the number density of ions of type i we will have

$$\sigma_d c = \sum_{i=1} N_i q_i \mu_i \quad . \tag{B.4}$$

Which is the velocity of the particles under the action of the driving force.

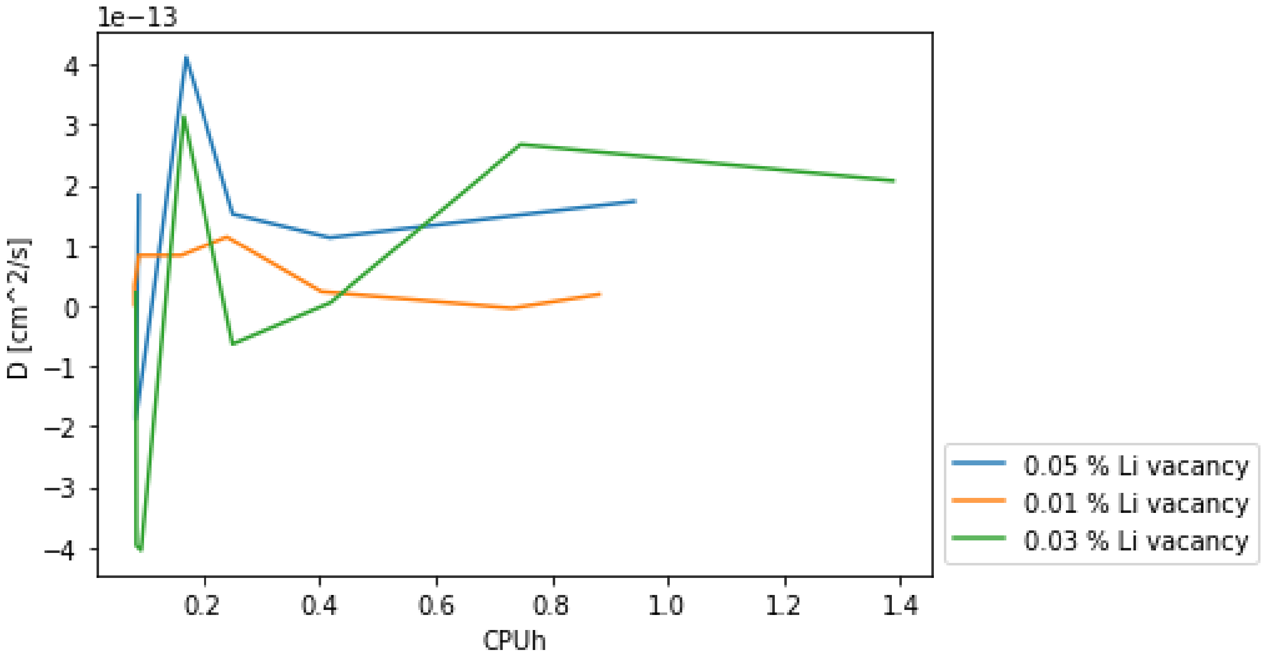

Figure B.1 Convergence test for the lithium diffusion coefficient within the graphite structure. The different lines represent different vacancy concentrations. This convergence test was performed on one computer core of a Intel(R) Core(TM) i7-6700 CPU.

B.2 LiC$_6$: Input Parameters and Analysis

If we go to a high occupancy parameter, which will bring us to the fully intercalated LiC$_6$, the position are controlled as well by the distance parameter $j_1 = 2.46$ Å and $j_2 = 4.30$ Å.

$$N_{cc} = N_{sites} \cdot occ \tag{B.5}$$

where the number of sites is determined by the length of the lattice $N_{sites} = L^2$ and occ is the parameter that controls the empty/full sites of the charged particles. In this case the velocity can be directly calculated using a simple `python` command

Algorithm 2 A simple python command in order to obtain directly the velocity

```
velocity = occ * (OTF * prc.T) *a
```

In general, the starting point for the simulation was an activation energy of 0.503 meV for a lithium jump. For additional details the reader is also referred to chapter 3.

In Figure B.1 we show the convergence behaviour of the diffusion coefficient of lithium with respect to the required CPUh. As one can clearly see from the picture, the diffusion coefficient is already converged within 1 h of simulation time for both 0.05% and 0.01% of Li vacancy concentration. Only the system with a Li vacancy of 0.03% needs a slightly longer simulation time until convergence is reached. However, convergence is reached within 2 h simulation time. Overall this clearly demonstrates the capabilities of our ckMC approach. Similar statistics can not be achieved with MD simulations, at least not within such a short simulation time. It should be noted, that this convergence test was performed on one computer core of a Intel(R) Core(TM) i7-6700 CPU.

B.3 Equations related to the ckMC implementation

$$p = k_o e^{q^T V q^T} e^{2\alpha q^T (Vi)} \quad . \tag{B.6}$$

$$k_{\text{rate}} = \frac{k_{\text{B}} T}{h} e^{-E_{\mathrm{A}}/k_{\text{B}} T} \quad . \tag{B.7}$$

Rate constants

$$k_i = k_0 * e^{(q^T V q - (q^T + \Delta q_i^T) V (q + \Delta q_i))} = k_0 * e^{(-2 q^T V \Delta q_i - \Delta q_i^T V (q + \Delta q_i))} \quad . \tag{B.8}$$

the factors

$$f_i^{n+1} = f_i^n * e^{(-2 * \Delta q_n^T V \Delta q_i)} \quad . \tag{B.9}$$

with

$$f_i^0 = f_i^n * e^{(-2 q_0^T V \Delta q_i - \Delta q_n^T V \Delta q_i)} \quad . \tag{B.10}$$

Here, V is the solution from the Poisson equation, and the potential is

$$V(i,j) = \phi(r_{i,j}) \quad . \tag{B.11}$$

with:

$$\phi(r_{i,j}) = \sum_n \frac{erfc(\eta |r_{i,j} - \boldsymbol{n} L|)}{|r_{i,j} - \boldsymbol{n} L|} \quad . \tag{B.12}$$

It is the easiest to introduce classes of process (in kmos we call these classes 'reactions'), which combine all equivalent processes. A particular process is then identified by its class label α and the site i at which it is defined. One particular property of these classes is that their changes obey the relation

$$\Delta(q_{i,\alpha})_j = \Delta(q_{0,\alpha})_{j+1} \quad . \tag{B.13}$$

j is a multi-index and periodic, *i.e.* if j, in one dimension, is larger than the periodicity n we set $j = j$ mod n. In three dimensions, this is meant elementwise. For diffusions, an example is the process class α, whose members moves a positive charge from a site $\boldsymbol{i}$ $\boldsymbol{i} = (i_x, i_y, i_z)$ to $\boldsymbol{i} + \boldsymbol{e}_y = (i_x, i_y + 1, i_z)$. The corresponding Δq_i, α is given by

$$(\Delta q_{\boldsymbol{i}}, \alpha)_{\boldsymbol{j}} = -\delta_{ix,jx} \delta_{iy,jy} \delta_{iz,jz} + \delta_{ix,jx} \delta_{iy+1,jy} \delta_{iz,jz} \quad . \tag{B.14}$$

In general, a class β moves a charge by a vector $\boldsymbol{v}_\beta Z$. Then

$$(\Delta q_{\boldsymbol{i}}, \alpha)_{\boldsymbol{j}} = -\delta_{\boldsymbol{i},\boldsymbol{j}} + \delta_{\boldsymbol{i}+\boldsymbol{v},\boldsymbol{j}} \quad . \tag{B.15}$$

One has to be aware that

$$\boldsymbol{r}_{\boldsymbol{i}} = i_x \Delta r_x \boldsymbol{e}_x + i_y \Delta r_y \boldsymbol{e}_y + i_z \Delta r_z \boldsymbol{e}_z \quad . \tag{B.16}$$

The update involves then the following changes:

$$\Delta q_i = (0, ..., -1, 1, ...0) \quad . \tag{B.17}$$

Here, the q_i is the distributed ion after the propagation of the system. It follows that,

$$\Delta q_n = (0, ..., -1, 1, ...0) \quad . \tag{B.18}$$

The q_n is then the generic update, on the distribution of the atoms after a certain point.

$$V \Delta q_n = \phi(r_{i,n}) + q^2 \phi(r(i,n)) = \phi(r_{i,n}) \Delta q_n + \frac{\epsilon}{2L} q_n^2 n \tag{B.19}$$

It holds,

$$V = \frac{1}{2} \sum_i^N q_i \phi(r_i) \quad . \tag{B.20}$$

with

$$\phi(r_i) = \sum_{j,n} \frac{q_j}{|r_{ij} + nL|} \quad . \tag{B.21}$$

B.4 Poisson Boltzmann Linearized

The Poisson Boltzmann Linearized (PBL) is a second order partial differential equation given by

$$\triangle \varPhi(r) = -\frac{\rho(r)}{(\varepsilon_0 \varepsilon_r)} \quad . \tag{B.22}$$

where $\triangle$ is the Laplace operator.
The charge density can be replaced by q_i. One obtains the following form of PBL:

$$\nabla \phi(r) = \sum_{i=1}^{N} \frac{q_i}{(\varepsilon_0 \varepsilon_r)} \quad . \tag{B.23}$$

B.5 Equations related to the ionic conductivity and mobility

The ionic conductivity in solids is given by $\sigma_{DC} = \sigma_C + \sigma_A$ Obviously this will be mediated by the concentration of the cation vacancy and the background. However, in general, it is given by the contribution of the cation and anions. One can identify the fowllowing:

$$D_{\sigma C} = \frac{k_B T \sigma_C}{N_C q^2} \tag{B.24}$$

and

$$D_{\sigma A} = \frac{k_B T \sigma_A}{N_A q^2} \quad . \tag{B.25}$$

Here, if one uses the relationship $N_C = N_A = N_{ion}$ one can then write

$$D_\sigma = D_{\sigma_C} + D_{\sigma_A} \tag{B.26}$$

or

$$D_\sigma = \frac{k_B T \sigma_{DC}}{N_{ion} q^2} \quad . \tag{B.27}$$

$$\sigma = \frac{q_i^2 c_i}{k_B T} D_i \tag{B.28}$$

$$D_{iO} = u_i RT; D_i = \frac{D_{i0}}{N_A} = \frac{u_i RT}{N_A} = u_i k_B T \tag{B.29}$$

For the ion mobility calculation we use

$$D_i = \lambda_i RT(z_i/(F^2) \tag{B.30}$$

where F is the Faraday constant, R the molar gas constant, T the temperature and z_i is the charge of the ion, λ_i is the single ion conductivity which is given by

$$\lambda_i = u_i \cdot F \quad . \tag{B.31}$$

The velocity u_i (sometimes also denoted as v_i) of an ion under the influence of an electric field (E) can be described using the following formula:

$$u_i = \frac{v_i}{E} \quad . \tag{B.32}$$

One can then define the ion mobility within a crystal by

$$\sigma = nzeu \quad . \tag{B.33}$$

where n is the charge carrier per volume, z is again the charge of the ion and u the velocity.

A word on rate equations

The interaction between the charged ions was taken into account within the on the fly (otf) approach, as a novel feature. The external field and the multilevel approach that is not discussed here where implemented as additional features within the code and is available upon request. The otf rates read to

$$OTF_{rate} = BASE_{rate} \cdot e^{\beta(Nr_{cation-1nn} \cdot E_{cation-1nn})} \quad , \tag{B.34}$$

where β is given by

$$\beta = \frac{1}{k_B T} \tag{B.35}$$

Here, k_B is the Boltzmann constant and T the temperature.

Bibliography

[1] [Online]. Available: https://ec.europa.eu/clima/policies/international/negotiations/paris_en

[2] D. V. Ragone, "Review of battery systems for electrically powered vehicles," in *SAE Technical Paper Series*. SAE International, Feb. 1968. [Online]. Available: https://doi.org/10.4271/680453

[3] Y. Liu, Y. Zhu, and Y. Cui, "Challenges and opportunities towards fast-charging battery materials," *Nature Energy*, vol. 4, no. 7, pp. 540–550, Jun. 2019. [Online]. Available: https://doi.org/10.1038/s41560-019-0405-3

[4] J.-M. Tarascon and M. Armand, "Issues and challenges facing rechargeable lithium batteries," *Nature*, vol. 414, no. 6861, pp. 359–367, Nov. 2001. [Online]. Available: https://doi.org/10.1038/35104644

[5] M. Armand and J.-M. Tarascon, "Building better batteries," *Nature*, vol. 451, no. 7179, pp. 652–657, Feb. 2008. [Online]. Available: https://doi.org/10.1038/451652a

[6] W. Cai, Y.-X. Yao, G.-L. Zhu, C. Yan, L.-L. Jiang, C. He, J.-Q. Huang, and Q. Zhang, "A review on energy chemistry of fast-charging anodes," *Chemical Society Reviews*, vol. 49, no. 12, pp. 3806–3833, 2020. [Online]. Available: https://doi.org/10.1039/c9cs00728h

[7] J. B. Goodenough and K.-S. Park, "The li-ion rechargeable battery: A perspective," *Journal of the American Chemical Society*, vol. 135, no. 4, pp. 1167–1176, Jan. 2013. [Online]. Available: https://doi.org/10.1021/ja3091438

[8] V. Aravindan, J. Gnanaraj, Y.-S. Lee, and S. Madhavi, "Insertion-type electrodes for nonaqueous li-ion capacitors," *Chemical Reviews*, vol. 114, no. 23, pp. 11 619–11 635, Jul. 2014. [Online]. Available: https://doi.org/10.1021/cr5000915

[9] B. Scrosati, *Modern Batteries*. Elsevier, 1997. [Online]. Available: https://doi.org/10.1016/b978-0-340-66278-6.x5000-1

[10] R. A. Huggins, *Advanced Batteries*. Springer US, 2009. [Online]. Available: https://doi.org/10.1007/978-0-387-76424-5

[11] B. Scrosati and J. Garche, "Lithium batteries: Status, prospects and future," *Journal of Power Sources*, vol. 195, no. 9, pp. 2419–2430, May 2010. [Online]. Available: https://doi.org/10.1016/j.jpowsour.2009.11.048

[12] M. S. Whittingham, "Lithium batteries and cathode materials," *Chemical Reviews*, vol. 104, no. 10, pp. 4271–4302, Sep. 2004. [Online]. Available: https://doi.org/10.1021/cr020731c

[13] T. P. Kumar, T. S. D. Kumari, and M. Stephan, "Carbonaceous anode materials for lithium-ion batteries - the road ahead," *Journal of the Indian Institute of Science*, vol. 89, pp. 393–424, 2012.

[14] M. S. Dresselhaus and G. Dresselhaus, "Intercalation compounds of graphite," *Advances in Physics*, vol. 51, no. 1, pp. 1–186, Jan. 2002. [Online]. Available: https://doi.org/10.1080/00018730110113644

[15] J. Asenbauer, T. Eisenmann, M. Kuenzel, A. Kazzazi, Z. Chen, and D. Bresser, “The success story of graphite as a lithium-ion anode material – fundamentals, remaining challenges, and recent developments including silicon (oxide) composites,” *Sustainable Energy & Fuels*, vol. 4, no. 11, pp. 5387–5416, 2020. [Online]. Available: https://doi.org/10.1039/d0se00175a

[16] M. Winter, K. C. Moeller, and J. O. Besenhard, “Carbonaceous and graphitic anodes,” in *Lithium Batteries*. Springer US, 2009, pp. 145–194. [Online]. Available: https://doi.org/10.1007/978-0-387-92675-9_5

[17] K. Ji, J. Han, A. Hirata, T. Fujita, Y. Shen, S. Ning, P. Liu, H. Kashani, Y. Tian, Y. Ito, J. ichi Fujita, and Y. Oyama, “Lithium intercalation into bilayer graphene,” *Nature Communications*, vol. 10, no. 1, Jan. 2019. [Online]. Available: https://doi.org/10.1038/s41467-018-07942-z

[18] H. Zabel and S. Solin, Eds., *Graphite Intercalation Compounds I*. Springer Berlin Heidelberg, 1990. [Online]. Available: https://doi.org/10.1007/978-3-642-75270-4

[19] M. Letellier, F. Chevallier, C. Clinard, E. Frackowiak, J.-N. Rouzaud, F. Béguin, M. Morcrette, and J.-M. Tarascon, “The first in situ 7li nuclear magnetic resonance study of lithium insertion in hard-carbon anode materials for li-ion batteries,” *The Journal of Chemical Physics*, vol. 118, no. 13, pp. 6038–6045, Apr. 2003. [Online]. Available: https://doi.org/10.1063/1.1556092

[20] X. Han, L. Lu, Y. Zheng, X. Feng, Z. Li, J. Li, and M. Ouyang, “A review on the key issues of the lithium ion battery degradation among the whole life cycle,” *eTransportation*, vol. 1, p. 100005, Aug. 2019. [Online]. Available: https://doi.org/10.1016/j.etran.2019.100005

[21] J. D. Bernal, “The structure of graphite,” *Proceedings of the Royal Society of London. Series A, Containing Papers of a Mathematical and Physical Character*, vol. 106, no. 740, pp. 749–773, Dec. 1924. [Online]. Available: https://doi.org/10.1098/rspa.1924.0101

[22] M. Winter, J. Besenhard, M. Spahr, and P. Novak, “Insertion electrode materials for rechargeable lithium batteries,” *Advanced Materials*, vol. 10, no. 10, pp. 725–763, JUL 9 1998.

[23] E. A. Taft and H. R. Philipp, “Optical properties of graphite,” *Physical Review*, vol. 138, no. 1A, pp. A197–A202, Apr. 1965. [Online]. Available: https://doi.org/10.1103/physrev.138.a197

[24] R. C. Tatar and S. Rabii, “Electronic properties of graphite: A unified theoretical study,” *Physical Review B*, vol. 25, no. 6, pp. 4126–4141, Mar. 1982. [Online]. Available: https://doi.org/10.1103/physrevb.25.4126

[25] N. Daumas and A. Herold, “Relations between phase concept and reaction mechanics in graphite insertion compounds,” *Comptes Rendus Hebdomadaires Des Seances De L’Academie Des Sciences Serie C*, vol. 268, no. 5, 1969.

[26] W. Rüdorff and U. Hofmann, “Über graphitsalze,” *Zeitschrift für anorganische und allgemeine Chemie*, vol. 238, no. 1, pp. 1–50, Jun. 1938. [Online]. Available: https://doi.org/10.1002/zaac.19382380102

[27] U. Hofmann and W. Rüdorff, “The formation of salts from graphite by strong acids,” *Trans. Faraday Soc.*, vol. 34, no. 0, pp. 1017–1021, 1938. [Online]. Available: https://doi.org/10.1039/tf9383401017

[28] R. B. Smith, E. Khoo, and M. Z. Bazant, “Intercalation kinetics in multiphase-layered materials,” *The Journal of Physical Chemistry C*, vol. 121, no. 23, pp. 12 505–12 523, Jun. 2017. [Online]. Available: https://doi.org/10.1021/acs.jpcc.7b00185

[29] E. R. White, J. J. Lodico, and B. C. Regan, “Intercalation events visualized in single microcrystals of graphite,” *Nature Communications*, vol. 8, no. 1, Dec. 2017. [Online]. Available: https://doi.org/10.1038/s41467-017-01787-8

[30] G. Kirczenow, “Domain model of stage order and disorder in intercalation compounds,” *Physical Review B*, vol. 31, Apr 1985. [Online]. Available: https://link.aps.org/doi/10.1103/PhysRevB.31.5376

[31] S. Krishnan, G. Brenet, E. Machado-Charry, D. Caliste, L. Genovese, T. Deutsch, and P. Pochet, “Revisiting the domain model for lithium intercalated graphite,” *Appl. Phys. Lett.*, vol. 103, dec 2013. [Online]. Available: https://aip.scitation.org/doi/10.1063/1.4850877

[32] J. E. Fischer, “Structural chemistry, phase equilibria and phase transitions in graphite intercalation compounds,” in *Chemical Physics of Intercalation*. Springer US, 1987, pp. 59–78. [Online]. Available: https://doi.org/10.1007/978-1-4757-9649-0_3

[33] D. P. DiVincenzo and T. C. Koch, “Theoretical phase diagram for li-intercalated graphite,” *Physical Review B*, vol. 30, no. 12, pp. 7092–7096, Dec. 1984. [Online]. Available: https://doi.org/10.1103/physrevb.30.7092

[34] D. P. DiVincenzo and E. J. Mele, “Cohesion and structure in stage-1 graphite intercalation compounds,” *Physical Review B*, vol. 32, no. 4, pp. 2538–2553, Aug. 1985. [Online]. Available: https://doi.org/10.1103/physrevb.32.2538

[35] A. Hightower, C. C. Ahn, B. Fultz, and P. Rez, “Electron energy-loss spectrometry on lithiated graphite,” *Applied Physics Letters*, vol. 77, no. 2, pp. 238–240, Jul. 2000. [Online]. Available: https://doi.org/10.1063/1.126936

[36] J. R. Dahn, “Phase diagram ofLixC6,” *Physical Review B*, vol. 44, no. 17, pp. 9170–9177, Nov. 1991. [Online]. Available: https://doi.org/10.1103/physrevb.44.9170

[37] N. Imanishi, Y. Takeda, and O. Yamamoto, “Development of the carbon anode in lithium ion batteries,” in *Lithium Ion Batteries*. Wiley-VCH Verlag GmbH, 1998, pp. 98–126. [Online]. Available: https://doi.org/10.1002/9783527612000.ch5

[38] F. J. Sonia, M. K. Jangid, B. Ananthoju, M. Aslam, P. Johari, and A. Mukhopadhyay, “Understanding the li-storage in few layers graphene with respect to bulk graphite: experimental, analytical and computational study,” *Journal of Materials Chemistry*, vol. 5, pp. 8662–8679, 2017.

[39] F. J. Sonia, M. K. Jangid, M. Aslam, P. Johari, and A. Mukhopadhyay, “Enhanced and faster potassium storage in graphene with respect to graphite: A comparative study with lithium storage,” *ACS Nano*, Jan. 2019. [Online]. Available: https://doi.org/10.1021/acsnano.8b08867

[40] J. R. Dahn, T. Zheng, Y. Liu, and J. S. Xue, “Mechanisms for lithium insertion in carbonaceous materials,” *Science*, vol. 270, no. 5236, pp. 590–593, Oct. 1995. [Online]. Available: https://doi.org/10.1126/science.270.5236.590

[41] K. Sato, M. Noguchi, A. Demachi, N. Oki, and M. Endo, “A mechanism of lithium storage in disordered carbons,” *Science*, vol. 264, no. 5158, pp. 556–558, Apr. 1994. [Online]. Available: https://doi.org/10.1126/science.264.5158.556

[42] R. Yazami and M. Deschamps, “High reversible capacity carbon-lithium negative electrode in polymer electrolyte,” *Journal of Power Sources*, vol. 54, no. 2, pp. 411–415, Apr. 1995. [Online]. Available: https://doi.org/10.1016/0378-7753(94)02113-h

[43] A. Mabuchi, K. Tokumitsu, H. Fujimoto, and T. Kasuh, “Charge-discharge characteristics of the mesocarbon miocrobeads heat-treated at different temperatures,” *Journal of The Electrochemical Society*, vol. 142, pp. 1041–1046, 1995.

[44] P. Liu, “Diffusion of lithium in carbon,” *Solid State Ionics*, vol. 92, no. 1-2, pp. 91–97, Nov. 1996. [Online]. Available: https://doi.org/10.1016/s0167-2738(96)00465-1

[45] T. Zheng, Y. Liu, E. W. Fuller, S. Tseng, U. von Sacken, and J. R. Dahn, “Lithium insertion in high capacity carbonaceous materials,” *Journal of The Electrochemical Society*, vol. 142, no. 8, pp. 2581–2590, Aug. 1995. [Online]. Available: https://doi.org/10.1149/1.2050057

[46] P. Papanek, , M. Radosavljević, and J. Fischer, “Lithium insertion in disordered carbon-hydrogen alloys: Intercalation vs covalent binding,” *Chemistry of Materials*, vol. 8, pp. 1519–1526, 1996.

[47] T. Enoki, M. Endo, and M. Suzuki, *Graphite Intercalation Compounds and Applications*. Oxford University Press, Apr. 2003. [Online]. Available: https://doi.org/10.1093/oso/9780195128277.001.0001

[48] M. Kühne, F. Börrnert, S. Fecher, M. Ghorbani-Asl, J. Biskupek, D. Samuelis, A. V. Krasheninnikov, U. Kaiser, and J. H. Smet, “Reversible superdense ordering of lithium between two graphene sheets,” *Nature*, vol. 564, no. 7735, pp. 234–239, Nov. 2018. [Online]. Available: https://doi.org/10.1038/s41586-018-0754-2

[49] G. Fey, “High-capacity disordered carbons derived from peanut shells as lithium-intercalating anode materials,” *Synthetic Metals*, vol. 139, no. 1, pp. 71–80, Aug. 2003. [Online]. Available: https://doi.org/10.1016/s0379-6779(03)00082-1

[50] E. Pollak, B. Geng, K.-J. Jeon, I. T. Lucas, T. J. Richardson, F. Wang, and R. Kostecki, “The interaction of li+ with single-layer and few-layer graphene.” *Nano letters*, vol. 10 9, pp. 386–8, 2010.

[51] N. Kheirabadi and A. Shafiekhani, “Graphene/li-ion battery,” *Journal of Applied Physics*, vol. 112, no. 12, p. 124323, Dec. 2012. [Online]. Available: https://doi.org/10.1063/1.4771923

[52] F. Yao, F. Güneş, H. Q. Ta, S. M. Lee, S. J. Chae, K. Y. Sheem, C. S. Cojocaru, S. S. Xie, and Y. H. Lee, “Diffusion mechanism of lithium ion through basal plane of layered graphene,” *Journal of the American Chemical Society*, vol. 134, no. 20, pp. 8646–8654, May 2012. [Online]. Available: https://doi.org/10.1021/ja301586m

[53] L.-J. Zhou, Z. F. Hou, L.-M. Wu, and Y.-F. Zhang, “First-principles studies of lithium adsorption and diffusion on graphene with grain boundaries,” *The Journal of Physical Chemistry C*, vol. 118, no. 48, pp. 28 055–28 062, Nov. 2014. [Online]. Available: https://doi.org/10.1021/jp5102175

[54] M. Kühne, F. Paolucci, J. Popovic, P. M. Ostrovsky, J. Maier, and J. H. Smet, “Ultrafast lithium diffusion in bilayer graphene,” *Nature Nanotechnology*, vol. 12, no. 9, pp. 895–900, Jun. 2017. [Online]. Available: https://doi.org/10.1038/nnano.2017.108

[55] V. A. Sethuraman, L. J. Hardwick, V. Srinivasan, and R. Kostecki, “Surface structural disordering in graphite upon lithium intercalation/deintercalation,” *Journal of Power Sources*, vol. 195, no. 11, pp. 3655–3660, 2010.

[56] A. Herold, “Reflections on matter transfer in graphite intercalation chemistry,” *Synthetic Metals*, vol. 23, no. 1-4, pp. 27–35, Mar. 1988. [Online]. Available: https://doi.org/10.1016/0379-6779(88)90457-2

[57] J. Yue and Y.-G. Guo, "The devil is in the electrons," *Nature Energy*, vol. 4, no. 3, pp. 174–175, Feb. 2019. [Online]. Available: https://doi.org/10.1038/s41560-019-0335-0

[58] P. Rozier and J. M. Tarascon, "Review—li-rich layered oxide cathodes for next-generation li-ion batteries: Chances and challenges," *Journal of The Electrochemical Society*, vol. 162, no. 14, pp. A2490–A2499, 2015. [Online]. Available: https://doi.org/10.1149/2.0111514jes

[59] A. Manthiram, J. C. Knight, S.-T. Myung, S.-M. Oh, and Y.-K. Sun, "Nickel-rich and lithium-rich layered oxide cathodes: Progress and perspectives," *Advanced Energy Materials*, vol. 6, no. 1, p. 1501010, Oct. 2015. [Online]. Available: https://doi.org/10.1002/aenm.201501010

[60] A. Magerl, H. Zabel, and I. S. Anderson, "In-plane jump diffusion of li inLiC6," *Physical Review Letters*, vol. 55, no. 2, pp. 222–225, Jul. 1985. [Online]. Available: https://doi.org/10.1103/physrevlett.55.222

[61] K. Toyoura, Y. Koyama, A. Kuwabara, and I. Tanaka, "Effects of off-stoichiometry of LiC6 on the lithium diffusion mechanism and diffusivity by first principles calculations," *The Journal of Physical Chemistry C*, vol. 114, no. 5, pp. 2375–2379, Jan. 2010. [Online]. Available: https://doi.org/10.1021/jp910134u

[62] K. Persson, Y. Hinuma, Y. S. Meng, A. V. der Ven, and G. Ceder, "Thermodynamic and kinetic properties of the li-graphite system from first-principles calculations," *Physical Review B*, vol. 82, no. 12, Sep. 2010. [Online]. Available: https://doi.org/10.1103/physrevb.82.125416

[63] J. Langer, V. Epp, P. Heitjans, F. A. Mautner, and M. Wilkening, "Lithium motion in the anode material LiC_6 as seen via time-domain ^{7}li NMR," *Physical Review B*, vol. 88, no. 9, pp. 094 304–1–094 304–9, Sep. 2013. [Online]. Available: https://doi.org/10.1103/physrevb.88.094304

[64] Y. NuLi, J. Yang, and Z. Jiang, "Intercalation of lithium ions into bulk and powder highly oriented pyrolytic graphite," *Journal of Physics and Chemistry of Solids*, vol. 67, no. 4, pp. 882–886, Apr. 2006. [Online]. Available: https://doi.org/10.1016/j.jpcs.2005.11.003

[65] K. Dokko, N. Nakata, Y. Suzuki, and K. Kanamura, "High-rate lithium deintercalation from lithiated graphite single-particle electrode," *The Journal of Physical Chemistry C*, vol. 114, no. 18, pp. 8646–8650, Apr. 2010. [Online]. Available: https://doi.org/10.1021/jp101166d

[66] N. Takami, A. Satoh, M. Hara, and T. Ohsaki, "Structural and kinetic characterization of lithium intercalation into carbon anodes for secondary lithium batteries," *Journal of The Electrochemical Society*, vol. 142, no. 2, pp. 371–379, Dec. 2019. [Online]. Available: https://doi.org/10.1149/1.2044017

[67] I. Umegaki, S. Kawauchi, H. Sawada, H. Nozaki, Y. Higuchi, K. Miwa, Y. Kondo, M. Månsson, M. Telling, F. C. Coomer, S. P. Cottrell, T. Sasaki, T. Kobayashi, and J. Sugiyama, "Li-ion diffusion in li intercalated graphite c6li and c12li probed by μ+SR," *Physical Chemistry Chemical Physics*, vol. 19, no. 29, pp. 19 058–19 066, 2017. [Online]. Available: https://doi.org/10.1039/c7cp02047c

[68] T. L. Kulova, A. M. Skundin, E. A. Nizhnikovskii, and A. V. Fesenko, "Temperature effect on the lithium diffusion rate in graphite," *Russian Journal of Electrochemistry*, vol. 42, no. 3, pp. 259–262, Mar. 2006. [Online]. Available: https://doi.org/10.1134/s1023193506030086

[69] R. Yazami and P. Touzain, "A reversible graphite-lithium negative electrode for electrochemical generators," *Journal of Power Sources*, vol. 9, no. 3, pp. 365–371, Jan. 1983. [Online]. Available: https://doi.org/10.1016/0378-7753(83)87040-2

[70] R. Yazami and Y. Reynier, “Thermodynamics and crystal structure anomalies in lithium-intercalated graphite,” *Journal of Power Sources*, vol. 153, no. 2, pp. 312–318, Feb. 2006. [Online]. Available: https://doi.org/10.1016/j.jpowsour.2005.05.087

[71] A. M. Skundin, O. Y. Grigor’eva, T. L. Kulova, and S. V. Pouchko, “The lithium intercalation into graphite from electrolyte and from solid lithium,” *Journal of Solid State Electrochemistry*, vol. 8, no. 1, pp. 11–14, Dec. 2003. [Online]. Available: https://doi.org/10.1007/s10008-003-0413-9

[72] T. Uchida, T. Itoh, Y. Morikawa, H. Ikuta, and M. Wakihara, “Anode properties and diffusion coefficient of lithium of pitch based carbon powder,” *Denki Kagaku oyobi Kogyo Butsuri Kagaku*, vol. 61, no. 12, pp. 1390–1394, 1993.

[73] M. Morita, N. Nishimura, and Y. Matsuda, “Charge/discharge cycling behavior of pitch-based carbon fiber in organic electrolyte solutions,” *Electrochimica Acta*, vol. 38, no. 13, pp. 1721–1726, Sep. 1993. [Online]. Available: https://doi.org/10.1016/0013-4686(93)85068-a

[74] M. Jean, C. Desnoyer, A. Tranchant, and R. Messina, “Electrochemical and structural studies of petroleum coke in carbonate-based electrolytes,” *Journal of The Electrochemical Society*, vol. 142, no. 7, pp. 2122–2125, Jul. 1995. [Online]. Available: https://doi.org/10.1149/1.2044261

[75] N. Takami, A. Satoh, M. Hara, and T. Ohsaki, “Rechargeable lithium-ion cells using graphitized mesophase-pitch-based carbon fiber anodes,” *Journal of the Electrochemical Society*, vol. 142, no. 8, p. 2564, 1995.

[76] R. B. Goldner, T.-Y. Liu, and S. Slaven, “A transient method for measuring diffusion coefficients of thin film battery electrodes: Results for and thin films,” *Journal of the Electrochemical Society*, vol. 143, no. 6, p. L129, 1996.

[77] T. Uchida, Y. Morikawa, H. Ikuta, M. Wakihara, and K. Suzuki, “Chemical diffusion coefficient of lithium in carbon fiber,” *Journal of the Electrochemical Society*, vol. 143, no. 8, p. 2606, 1996.

[78] M. D. Levi and D. Aurbach, “Diffusion coefficients of lithium ions during intercalation into graphite derived from the simultaneous measurements and modeling of electrochemical impedance and potentiostatic intermittent titration characteristics of thin graphite electrodes,” *The Journal of Physical Chemistry B*, vol. 101, no. 23, 1997. [Online]. Available: https://doi.org/10.1021/jp9701911

[79] B. Markovsky, M. D. Levi, and D. Aurbach, “The basic electroanalytical behavior of practical graphite–lithium intercalation electrodes,” *Electrochimica Acta*, vol. 43, no. 16-17, pp. 2287–2304, May 1998. [Online]. Available: https://doi.org/10.1016/s0013-4686(97)10172-4

[80] M. D. Levi and D. Aurbach, “The mechanism of lithium intercalation in graphite film electrodes in aprotic media. part 1. high resolution slow scan rate cyclic voltammetric studies and modeling,” *Journal of Electroanalytical Chemistry*, vol. 421, no. 1-2, pp. 79–88, 1997.

[81] N. Takami, A. Satoh, T. Ohsaki, and M. Kanda, “Large hysteresis during lithium insertion into and extraction from high-capacity disordered carbons,” *Journal of the Electrochemical Society*, vol. 145, no. 2, p. 478, 1998.

[82] T. Piao, S.-M. Park, C.-H. Doh, and S.-I. Moon, “Intercalation of lithium ions into graphite electrodes studied by AC impedance measurements,” *Journal of The Electrochemical Society*, vol. 146, no. 8, pp. 2794–2798, Aug. 1999. [Online]. Available: https://doi.org/10.1149/1.1392010

[83] P. Yu, B. N. Popov, J. A. Ritter, and R. E. White, “Determination of the lithium ion diffusion coefficient in graphite,” *Journal of The Electrochemical Society*, vol. 146, no. 1, p. 8, 1999.

[84] Q. Wang, H. Li, X. Huang, and L. Chen, "Determination of chemical diffusion coefficient of lithium ion in graphitized mesocarbon microbeads with potential relaxation technique," *Journal of the Electrochemical Society*, vol. 148, no. 7, p. A737, 2001.

[85] A. Churikov, "Chronoamperometric determination of the rate of lithium transfer in carbon electrodes," *Ehlektrokhimiya*, vol. 38, no. 1, pp. 120–125, 2002.

[86] C. AV, "Chronoamperometric determination of the rate of lithium transfer in carbon electrodes," *Russian journal of electrochemistry*, vol. 38, no. 1, pp. 103–108, 2002.

[87] N. Takami, A. Satoh, M. Hara, and T. Ohsaki, "Structural and kinetic characterization of lithium intercalation into carbon anodes for secondary lithium batteries," *Journal of The Electrochemical Society*, vol. 142, no. 2, p. 371, 1995.

[88] D. D. L. Chung, "Exfoliation of graphite," *Journal of Materials Science*, vol. 22, no. 12, pp. 4190–4198, Dec. 1987. [Online]. Available: https://doi.org/10.1007/bf01132008

[89] D. Aurbach and Y. Ein-Eli, "The study of li-graphite intercalation processes in several electrolyte systems using in situ x-ray diffraction," *Journal of the Electrochemical Society*, vol. 142, no. 6, p. 1746, 1995.

[90] D. Aurbach, Y. Ein-Eli, B. Markovsky, A. Zaban, S. Luski, Y. Carmeli, and H. Yamin, "The study of electrolyte solutions based on ethylene and diethyl carbonates for rechargeable li batteries: Ii. graphite electrodes," *Journal of The Electrochemical Society*, vol. 142, no. 9, p. 2882, 1995.

[91] J. Gong and H. Wu, "Electrochemical intercalation of lithium species into disordered carbon prepared by the heat-treatment of poly (p-phenylene) at 650○c for anode in lithium-ion battery," *Electrochimica Acta*, vol. 45, no. 11, pp. 1753–1762, Feb. 2000. [Online]. Available: https://doi.org/10.1016/s0013-4686(99)00400-4

[92] K. Pridatko, A. Churikov, and M. Volgin, "Determination of lithium diffusion rate by pulse potentiostatic method," *Russ. J. Power Sources (Elektrokhim. Energetika)*, vol. 3, p. 184, 2003.

[93] T. Katrašnik, I. Mele, and K. Zelič, "Multi-scale modelling of lithium-ion batteries: From transport phenomena to the outbreak of thermal runaway," *Energy Conversion and Management*, vol. 236, p. 114036, May 2021. [Online]. Available: https://doi.org/10.1016/j.enconman.2021.114036

[94] E. M. Gavilán-Arriazu, M. P. Mercer, D. E. Barraco, H. E. Hoster, and E. P. M. Leiva, "Kinetic monte carlo simulations applied to li-ion and post li-ion batteries: a key link in the multi-scale chain," *Progress in Energy*, vol. 3, no. 4, p. 042001, Aug. 2021. [Online]. Available: https://doi.org/10.1088/2516-1083/ac1a65

[95] W. Koch and M. C. Holthausen, *A Chemist's Guide to Density Functional Theory*. Wiley, Jul. 2001. [Online]. Available: https://doi.org/10.1002/3527600043

[96] P. Hohenberg and W. Kohn, "Inhomogeneous electron gas," *Physical Review*, vol. 136, no. 3B, pp. B864–B871, Nov. 1964. [Online]. Available: https://doi.org/10.1103/physrev.136.b864

[97] M. Kick, K. Reuter, and H. Oberhofer, "Intricacies of DFT+u, not only in a numeric atom centered orbital framework," *Journal of Chemical Theory and Computation*, vol. 15, no. 3, pp. 1705–1718, Feb. 2019. [Online]. Available: https://doi.org/10.1021/acs.jctc.8b01211

[98] W. Kohn and L. J. Sham, "Self-consistent equations including exchange and correlation effects," *Physical Review*, vol. 140, no. 4A, pp. A1133–A1138, Nov. 1965. [Online]. Available: https://doi.org/10.1103/physrev.140.a1133

[99] D. Fritsch and S. Schorr, “Climbing jacob’s ladder: A density functional theory case study for ag2znsnse4 and cu2znsnse4,” *Journal of Physics: Energy*, vol. 3, no. 1, p. 015002, Nov. 2020. [Online]. Available: https://doi.org/10.1088/2515-7655/abc07b

[100] J. P. Perdew, K. Burke, and M. Ernzerhof, “Generalized gradient approximation made simple,” *Physical Review Letters*, vol. 77, no. 18, pp. 3865–3868, Oct. 1996. [Online]. Available: https://doi.org/10.1103/physrevlett.77.3865

[101] H. Peng and J. P. Perdew, “Rehabilitation of the perdew-burke-ernzerhof generalized gradient approximation for layered materials,” *Physical Review B*, vol. 95, no. 8, Feb. 2017. [Online]. Available: https://doi.org/10.1103/physrevb.95.081105

[102] A. D. Becke, “Density-functional thermochemistry. III. the role of exact exchange,” *The Journal of Chemical Physics*, vol. 98, no. 7, pp. 5648–5652, Apr. 1993. [Online]. Available: https://doi.org/10.1063/1.464913

[103] J. Heyd, G. E. Scuseria, and M. Ernzerhof, “Hybrid functionals based on a screened coulomb potential,” *The Journal of Chemical Physics*, vol. 118, no. 18, pp. 8207–8215, May 2003. [Online]. Available: https://doi.org/10.1063/1.1564060

[104] A. Bruix, J. T. Margraf, M. Andersen, and K. Reuter, “First-principles-based multiscale modelling of heterogeneous catalysis,” *Nature Catalysis*, vol. 2, no. 8, pp. 659–670, Jun. 2019. [Online]. Available: https://doi.org/10.1038/s41929-019-0298-3

[105] J. Fish, G. J. Wagner, and S. Keten, “Mesoscopic and multiscale modelling in materials,” *Nature Materials*, vol. 20, no. 6, pp. 774–786, May 2021. [Online]. Available: https://doi.org/10.1038/s41563-020-00913-0

[106] A. C. T. van Duin, S. Dasgupta, F. Lorant, and W. A. Goddard, “ReaxFF: a reactive force field for hydrocarbons,” *The Journal of Physical Chemistry A*, vol. 105, no. 41, pp. 9396–9409, Sep. 2001. [Online]. Available: https://doi.org/10.1021/jp004368u

[107] V. E. Zalizniak and O. A. Zolotov, “Efficient embedded atom method interatomic potential for graphite and carbon nanostructures,” *Molecular Simulation*, vol. 43, no. 17, pp. 1480–1484, May 2017. [Online]. Available: https://doi.org/10.1080/08927022.2017.1324957

[108] D. Porezag, T. Frauenheim, T. Köhler, G. Seifert, and R. Kaschner, “Construction of tight-binding-like potentials on the basis of density-functional theory: Application to carbon,” *Physical Review B*, vol. 51, no. 19, pp. 12 947–12 957, May 1995. [Online]. Available: https://doi.org/10.1103/physrevb.51.12947

[109] M. Elstner, D. Porezag, G. Jungnickel, J. Elsner, M. Haugk, T. Frauenheim, S. Suhai, and G. Seifert, “Self-consistent-charge density-functional tight-binding method for simulations of complex materials properties,” *Phys. Rev. B*, vol. 58, pp. 7260–7268, Sep 1998. [Online]. Available: https://link.aps.org/doi/10.1103/PhysRevB.58.7260

[110] C. Panosetti, A. Engelmann, L. Nemec, K. Reuter, and J. T. Margraf, “Learning to use the force: Fitting repulsive potentials in density-functional tight-binding with gaussian process regression,” *Journal of Chemical Theory and Computation*, vol. 16, no. 4, pp. 2181–2191, Mar. 2020. [Online]. Available: https://doi.org/10.1021/acs.jctc.9b00975

[111] P. Koskinen and V. Mäkinen, “Density-functional tight-binding for beginners,” *Computational Materials Science*, vol. 47, no. 1, pp. 237–253, Nov. 2009. [Online]. Available: https://doi.org/10.1016/j.commatsci.2009.07.013

[112] C. Panosetti, S. B. Anniés, C. Grosu, S. Seidlmayer, and C. Scheurer, “DFTB modeling of lithium-intercalated graphite with machine-learned repulsive potential,” *The Journal of Physical Chemistry A*, vol. 125, no. 2, pp. 691–699, Jan. 2021. [Online]. Available: https://doi.org/10.1021/acs.jpca.0c09388

[113] C.-P. Chou, Y. Nishimura, C.-C. Fan, G. Mazur, S. Irle, and H. A. Witek, “Automatized parameterization of DFTB using particle swarm optimization,” *Journal of Chemical Theory and Computation*, vol. 12, no. 1, pp. 53–64, Dec. 2015. [Online]. Available: https://doi.org/10.1021/acs.jctc.5b00673

[114] Y. Shi and R. Eberhart, “A modified particle swarm optimizer,” in *1998, IEEE International Conference on Evolutionary Computation Proceedings. IEEE World Congress on Computational Intelligence (Cat. No.98TH8360).* IEEE, 1998. [Online]. Available: https://doi.org/10.1109/icec.1998.699146

[115] A. Engelmann, “The generation of pairwise interatomic potentials from arbitrary structures – a machine learning approach with application in DFTB,” in *he Generation of Pairwise Interatomic Potentials from Arbitrary Structures – A Machine Learning Approach with Application in DFTB*. Master Thesis, Technical University Munich, 2018.

[116] R. D. Woods and D. S. Saxon, “Diffuse surface optical model for nucleon-nuclei scattering,” *Physical Review*, vol. 95, no. 2, pp. 577–578, Jul. 1954. [Online]. Available: https://doi.org/10.1103/physrev.95.577

[117] [Online]. Available: https://github.com/pekkosk/hotbit

[118] [Online]. Available: https://pythonhosted.org/pyswarm

[119] S. Anniés, C. Panosetti, M. Voronenko, D. Mauth, C. Rahe, and C. Scheurer, “Accessing structural, electronic, transport and mesoscale properties of li-GICs via a complete DFTB model with machine-learned repulsion potential,” *Materials*, vol. 14, no. 21, p. 6633, Nov. 2021. [Online]. Available: https://doi.org/10.3390/ma14216633

[120] A. P. Bartók, M. C. Payne, R. Kondor, and G. Csányi, “Gaussian approximation potentials: The accuracy of quantum mechanics, without the electrons,” *Physical Review Letters*, vol. 104, no. 13, apr 2010. [Online]. Available: https://doi.org/10.1103/physrevlett.104.136403

[121] S. Grimme, J. Antony, S. Ehrlich, and H. Krieg, “A consistent and accurate ab initio parametrization of density functional dispersion correction (DFT-d) for the 94 elements h-pu,” *The Journal of Chemical Physics*, vol. 132, no. 15, p. 154104, Apr. 2010. [Online]. Available: https://doi.org/10.1063/1.3382344

[122] A. Tkatchenko and M. Scheffler, “Accurate molecular van der waals interactions from ground-state electron density and free-atom reference data,” *Physical Review Letters*, vol. 102, no. 7, Feb. 2009. [Online]. Available: https://doi.org/10.1103/physrevlett.102.073005

[123] A. Tkatchenko, R. A. DiStasio, R. Car, and M. Scheffler, “Accurate and efficient method for many-body van der waals interactions,” *Physical Review Letters*, vol. 108, no. 23, Jun. 2012. [Online]. Available: https://doi.org/10.1103/physrevlett.108.236402

[124] A. F. Voter, “INTRODUCTION TO THE KINETIC MONTE CARLO METHOD,” in *Radiation Effects in Solids*. Springer Netherlands, 2007, pp. 1–23. [Online]. Available: https://doi.org/10.1007/978-1-4020-5295-8_1

[125] A. P. J. Jansen, *An introduction to kinetic Monte Carlo simulations of surface reactions*. Springer, 2012, vol. 856.

[126] T. J. Delph, P. Cao, H. S. Park, and J. A. Zimmerman, “A harmonic transition state theory model for defect initiation in crystals,” *Modelling and Simulation in Materials Science and Engineering*, vol. 21, no. 2, p. 025010, Feb. 2013. [Online]. Available: https://doi.org/10.1088/0965-0393/21/2/025010

[127] M. Andersen, C. Panosetti, and K. Reuter, “A practical guide to surface kinetic monte carlo simulations,” *Frontiers in Chemistry*, vol. 7, Apr. 2019. [Online]. Available: https://doi.org/10.3389/fchem.2019.00202

[128] B. Peters, “Transition state theory,” in *Reaction Rate Theory and Rare Events Simulations*. Elsevier, 2017, pp. 227–271. [Online]. Available: https://doi.org/10.1016/b978-0-44-456349-1.00010-6

[129] M. J. Hoffmann, S. Matera, and K. Reuter, “kmos: A lattice kinetic monte carlo framework,” *Computer Physics Communications*, vol. 185, no. 7, pp. 2138–2150, Jul. 2014. [Online]. Available: https://doi.org/10.1016/j.cpc.2014.04.003

[130] P. C. Schmidt, “C. w. gardiner: Handbook of stochastic methods for physics, chemistry and the natural sciences, springer-verlag, berlin, heidelberg, new york, tokyo 1983. 442 seiten, preis: DM 115, -,” *Berichte der Bunsengesellschaft für physikalische Chemie*, vol. 89, no. 6, pp. 721–721, Jun. 1985. [Online]. Available: https://doi.org/10.1002/bbpc.19850890629

[131] M. R. Marcelin, “Contribution à l’étude de la cinétique physico-chimique,” *Annales de Physique*, vol. 9, no. 3, pp. 120–231, 1915. [Online]. Available: https://doi.org/10.1051/anphys/191509030120

[132] [Online]. Available: https://kmos.readthedocs.io/en/latest/

[133] K. Reuter, “Ab initio thermodynamics and first-principles microkinetics for surface catalysis,” *Catalysis Letters*, vol. 146, no. 3, pp. 541–563, Jan. 2016. [Online]. Available: https://doi.org/10.1007/s10562-015-1684-3

[134] H. Meskine, S. Matera, M. Scheffler, K. Reuter, and H. Metiu, “Examination of the concept of degree of rate control by first-principles kinetic monte carlo simulations,” *Surface Science*, vol. 603, no. 10-12, pp. 1724–1730, Jun. 2009. [Online]. Available: https://doi.org/10.1016/j.susc.2008.08.036

[135] K. Reuter, “First-principles kinetic monte carlo simulations for heterogeneous catalysis: Concepts, status, and frontiers,” in *Modeling and Simulation of Heterogeneous Catalytic Reactions*. Wiley-VCH Verlag GmbH & Co. KGaA, Dec. 2011, pp. 71–111. [Online]. Available: https://doi.org/10.1002/9783527639878.ch3

[136] M. Stamatakis, “Kinetic modelling of heterogeneous catalytic systems,” *Journal of Physics: Condensed Matter*, vol. 27, no. 1, p. 013001, Nov. 2014. [Online]. Available: https://doi.org/10.1088/0953-8984/27/1/013001

[137] K. A. Fichthorn and W. H. Weinberg, “Theoretical foundations of dynamical monte carlo simulations,” *The Journal of Chemical Physics*, vol. 95, no. 2, pp. 1090–1096, Jul. 1991. [Online]. Available: https://doi.org/10.1063/1.461138

[138] S. Döpking and S. Matera, “Error propagation in first-principles kinetic monte carlo simulation,” *Chemical Physics Letters*, vol. 674, pp. 28–32, Apr. 2017. [Online]. Available: https://doi.org/10.1016/j.cplett.2017.02.043

[139] V. Ramadesigan, P. W. C. Northrop, S. De, S. Santhanagopalan, R. D. Braatz, and V. R. Subramanian, “Modeling and simulation of lithium-ion batteries from a systems engineering perspective,” *Journal of The Electrochemical Society*, vol. 159, no. 3, pp. R31–R45, 2012. [Online]. Available: https://doi.org/10.1149/2.018203jes

[140] Y. Guo, R. B. Smith, Z. Yu, D. K. Efetov, J. Wang, P. Kim, M. Z. Bazant, and L. E. Brus, “Li intercalation into graphite: Direct optical imaging and cahn–hilliard reaction dynamics,” *The Journal of Physical Chemistry Letters*, vol. 7, no. 11, pp. 2151–2156, May 2016. [Online]. Available: https://doi.org/10.1021/acs.jpclett.6b00625

[141] M. Doyle, T. F. Fuller, and J. Newman, “Modeling of galvanostatic charge and discharge of the lithium/polymer/insertion cell,” *Journal of The Electrochemical Society*, vol. 140, no. 6, pp. 1526–1533, Jun. 1993. [Online]. Available: https://doi.org/10.1149/1.2221597

[142] M. Doyle and J. Newman, “The use of mathematical modeling in the design of lithium/polymer battery systems,” *Electrochimica Acta*, vol. 40, no. 13-14, pp. 2191–2196, Oct. 1995. [Online]. Available: https://doi.org/10.1016/0013-4686(95)00162-8

[143] J. Newman, K. E. Thomas, H. Hafezi, and D. R. Wheeler, “Modeling of lithium-ion batteries,” *Journal of Power Sources*, vol. 119-121, pp. 838–843, Jun. 2003. [Online]. Available: https://doi.org/10.1016/s0378-7753(03)00282-9

[144] M. Doyle, T. F. Fuller, and J. Newman, “Erratum: Modeling of galvanostatic charge and discharge of the lithium/polymer/insertion cell [j. electrochem. soc., 140, 1526 (1993)],” *Journal of The Electrochemical Society*, vol. 165, no. 11, pp. X13–X13, 2018. [Online]. Available: https://doi.org/10.1149/2.1181811jes

[145] J. M. Escalante, W. Ko, J. M. Foster, S. Krachkovskiy, G. Goward, and B. Protas, “Discerning models of phase transformations in porous graphite electrodes: Insights from inverse modelling based on MRI measurements,” *Electrochimica Acta*, vol. 349, p. 136290, Jul. 2020. [Online]. Available: https://doi.org/10.1016/j.electacta.2020.136290

[146] M. Z. Bazant, “Theory of chemical kinetics and charge transfer based on nonequilibrium thermodynamics,” *Accounts of Chemical Research*, vol. 46, no. 5, pp. 1144–1160, Mar. 2013. [Online]. Available: https://doi.org/10.1021/ar300145c

[147] R. R. Ernst, G. Bodenhausen, and A. Wokaun, *Principles of magnetic resonance in one and two dimensions*. Clarendon Press, 1987.

[148] H. Günther, “Nmr spectroscopy: Basic principles, concepts and applications in chemistry,” in *NMR spectroscopy: Basic principles, concepts, and applications in chemistry.* Weinheim: Wiley-VCH., 2013.

[149] J. Keeler, “Understanding nmr spectroscopy.” in *Understanding NMR spectroscopy.* Hoboken: Wiley, 2005.

[150] F. Qi, T. Jörg, and R. Böhmer, “Stimulated-echo NMR spectroscopy of 9be and 7li in solids: Method and application to ion conductors,” *Solid State Nuclear Magnetic Resonance*, vol. 22, no. 4, pp. 484–500, Dec. 2002. [Online]. Available: https://doi.org/10.1006/snmr.2002.0073

[151] A. Keller, “Spin-1 behavior of systems of dipolar coupled pairs of spin-1/2 nuclei,” in *Advances in Magnetic and Optical Resonance*. Elsevier, 1988, pp. 183–246. [Online]. Available: https://doi.org/10.1016/b978-0-12-025512-2.50007-5

[152] J. Granwehr and P. J. Roberts, “Inverse laplace transform of multidimensional relaxation data without non-negativity constraint,” *Journal of Chemical Theory and Computation*, vol. 8, no. 10, pp. 3473–3482, May 2012. [Online]. Available: https://doi.org/10.1021/ct3001393

[153] M. F. Graf, H. Tempel, S. S. Köcher, R. Schierholz, C. Scheurer, H. Kungl, R.-A. Eichel, and J. Granwehr, “Observing different modes of mobility in lithium titanate spinel by nuclear magnetic resonance,” *RSC Advances*, vol. 7, no. 41, pp. 25 276–25 284, 2017. [Online]. Available: https://doi.org/10.1039/c7ra01622k

[154] M. Mali, J. Roos, M. Sonderegger, D. Brinkmann, and P. Heitjans, “6li and 7li diffusion coefficients in solid lithium measured by the nmr pulsed field gradient technique,” *Journal of Physics F: Metal Physics*, vol. 18, pp. 403–412, 1988.

[155] E. O. Stejskal and J. E. Tanner, “Spin diffusion measurements : spin echoes in the presence of a time-dependent field gradient,” *Journal of Chemical Physics*, vol. 42, pp. 288–292, 1965.

[156] G. H. Sørland, “Pulsed field gradient—NMR sequences,” in *Dynamic Pulsed-Field-Gradient NMR*. Springer Berlin Heidelberg, 2014, pp. 1–35. [Online]. Available: https://doi.org/10.1007/978-3-662-44500-6_1

[157] D. F. Holcomb and R. E. Norberg, “Nuclear spin relaxation in alkali metals,” *Physical Review*, vol. 98, pp. 1074–1091, 1955.

[158] R. Messer and F. Noack, “Nuclear magnetic relaxation by self-diffusion in solid lithium:t1-frequency dependence,” *Applied physics*, vol. 6, pp. 79–88, 1975.

[159] J. M. Titman and B. Moores, “Nuclear spin relaxation and translational diffusion in dilute alloys of lithium,” *Journal of Physics F: Metal Physics*, vol. 2, pp. 592–604, 1972.

[160] D. C. Ailion and C. P. Slichter, “Observation of ultra-slow translational diffusion in metallic lithium by magnetic resonance,” *Physical Review*, vol. 137, 1965.

[161] M. Weithase and F. Noack, “Kernmagnetische spinrelaxation durch selbstdiffusion in festem lithium7li:t1, -frequenzabhängigkeit,” *Physica Status Solidi B-basic Solid State Physics*, vol. 57, 1973.

[162] P. Heitjans, “Use of beta radiation-detected nmr to study ionic motion in solids,” *Solid State Ionics*, pp. 50–64, 1986.

[163] P. Heitjans, A. Körblein, H. Ackermann, D. Dubbers, F. Fujara, and H.-J. Stöckmann, “Self-diffusion in solid lithium probed by spin-lattice relaxation of 8li nuclei,” *Journal of Physics F: Metal Physics*, vol. 15, pp. 41–54, 1985.

[164] J. Jeener and P. Broekaert, “Nuclear magnetic resonance in solids: Thermodynamic effects of a pair of rf pulses,” *Physical Review*, vol. 157, no. 2, pp. 232–240, May 1967. [Online]. Available: https://doi.org/10.1103/physrev.157.232

[165] R. G. C. McElroy, R. T. Thompson, and M. M. Pintar, “Proton-spin thermometry at low fields in liquid crystals,” *Physical Review A*, vol. 10, no. 1, pp. 403–415, Jul. 1974. [Online]. Available: https://doi.org/10.1103/physreva.10.403

[166] E. Göbel, W. Müller-Warmuth, H. Olyschläger, and H. Dutz, “7li NMR spectra, nuclear relaxation, and lithium ion motion in alkali silicate, borate, and phosphate glasses,” *Journal of Magnetic Resonance (1969)*, vol. 36, no. 3, pp. 371–387, Dec. 1979. [Online]. Available: https://doi.org/10.1016/0022-2364(79)90114-8

[167] A. N. Tikhonov, *Metody resheniya nekorrektnyh zadach*. Nauka, 1974.

[168] S. Merz, P. Jakes, S. Taranenko, R.-A. Eichel, and J. Granwehr, “Dynamics of [pyr13][tf2n] ionic liquid confined to carbon black,” *Physical Chemistry Chemical Physics*, vol. 21, no. 31, pp. 17 018–17 028, 2019. [Online]. Available: https://doi.org/10.1039/c9cp02651g

[169] S. Merz, J. Wang, P. Galvosas, and J. Granwehr, “MAS-NMR of [pyr13][tf2n] and [pyr16][tf2n] ionic liquids confined to carbon black: Insights and pitfalls,” *Molecules*, vol. 26, no. 21, p. 6690, Nov. 2021. [Online]. Available: https://doi.org/10.3390/molecules26216690

[170] M. Paulus, A. Paulus, P. Schleker, P. Jakes, R.-A. Eichel, P. Heitjans, and J. Granwehr, “Experimental evidence for the relaxation coupling of all longitudinal 7li magnetization orders in the superionic conductor li10gep2s12,” *Journal of Magnetic Resonance*, vol. 303, pp. 57–66, Jun. 2019. [Online]. Available: https://doi.org/10.1016/j.jmr.2019.04.006

[171] J. Conard, V. A. Nalimova, and D. Guerard, “Nmr study of lic$_x$ graphite intercalation compounds prepared under high pressure,” *Molecular Crystals and Liquid Crystals Science and Technology. Section A. Molecular Crystals and Liquid Crystals*, vol. 245, no. 1, pp. 25–30, 1994. [Online]. Available: https://doi.org/10.1080/10587259408051661

[172] S. Rabii and D. Guérard, “Stability of superdense lithium graphite compounds,” *Journal of Physics and Chemistry of Solids*, vol. 69, no. 5-6, pp. 1165–1167, May 2008. [Online]. Available: https://doi.org/10.1016/j.jpcs.2007.10.023

[173] O. Pecher, J. Carretero-González, K. J. Griffith, and C. P. Grey, “Materials’ methods: NMR in battery research,” *Chemistry of Materials*, vol. 29, no. 1, pp. 213–242, Nov. 2016. [Online]. Available: https://doi.org/10.1021/acs.chemmater.6b03183

[174] S. A. Kayser, A. Mester, A. Mertens, P. Jakes, R.-A. Eichel, and J. Granwehr, “Long-run in operando NMR to investigate the evolution and degradation of battery cells,” *Physical Chemistry Chemical Physics*, vol. 20, no. 20, pp. 13 765–13 776, 2018. [Online]. Available: https://doi.org/10.1039/c8cp01067f

[175] J. L. L. Lopez, P. J. Grandinetti, and A. C. Co, “Enhancing the real-time detection of phase changes in lithium–graphite intercalated compounds through derivative operando (dOp) NMR cyclic voltammetry,” *Journal of Materials Chemistry A*, vol. 6, no. 1, pp. 231–243, 2018. [Online]. Available: https://doi.org/10.1039/c7ta07521a

[176] R. L. Sacci, L. W. Gill, E. W. Hagaman, and N. J. Dudney, “Operando NMR and XRD study of chemically synthesized LiC oxidation in a dry room environment,” *Journal of Power Sources*, vol. 287, pp. 253–260, Aug. 2015. [Online]. Available: https://doi.org/10.1016/j.jpowsour.2015.04.035

[177] J. Conard and H. Estrade, “Résonance magnétique nucléaire du lithium interstitiel dans le graphite,” *Materials Science and Engineering*, vol. 31, pp. 173–176, Dec. 1977. [Online]. Available: https://doi.org/10.1016/0025-5416(77)90032-5

[178] D. Guerard and A. Herold, “Intercalation of lithium into graphite and other carbons,” *Carbon*, vol. 13, no. 4, pp. 337–345, Aug. 1975. [Online]. Available: https://doi.org/10.1016/0008-6223(75)90040-8

[179] J. Duan, Y. Zheng, W. Luo, W. Wu, T. Wang, Y. Xie, S. Li, J. Li, and Y. Huang, “Is graphite lithiophobic or lithiophilic?” *National Science Review*, vol. 7, no. 7, pp. 1208–1217, Jan. 2020. [Online]. Available: https://doi.org/10.1093/nsr/nwz222

[180] W. Schülke, A. Berthold, and A. Kaprolat, “Information about the band structure of LiC6 from inelastic synchrotron x-ray scattering,” *Synthetic Metals*, vol. 34, no. 1-3, pp. 423–428, Dec. 1989. [Online]. Available: https://doi.org/10.1016/0379-6779(89)90419-0

[181] V. Nalimova, D. Guérard, M. Lelaurain, and O. Fateev, “X-ray investigation of highly saturated li-graphite intercalation compound,” *Carbon*, vol. 33, no. 2, pp. 177–181, 1995. [Online]. Available: https://doi.org/10.1016/0008-6223(94)00123-h

[182] C. Bindra, V. A. Nalimova, D. E. Sklovsky, W. A. Kamitakahara, and J. E. Fischer, “Statics and dynamics of interlayer interactions in the dense high-pressure graphite compoundLiC2,” *Physical Review B*, vol. 57, no. 9, pp. 5182–5190, Mar. 1998. [Online]. Available: https://doi.org/10.1103/physrevb.57.5182

[183] G. Bondarenko, V. A. Nalimova, O. Fateev, D. Guérard, and K. N. Semenenko, “Vibrational spectra of superdense lithium graphite intercalation compounds,” *Carbon*, vol. 36, pp. 1107–1112, 1998.

[184] A. Schirmer, P. Heitjans, and V. A. Nalimova, “Conduction-electron induced spin-lattice relaxation of 8li in the high-pressure phase LiC2,” *Molecular Crystals and Liquid Crystals Science and Technology. Section A. Molecular Crystals and Liquid Crystals*, vol. 310, no. 1, pp. 291–296, Feb. 1998. [Online]. Available: https://doi.org/10.1080/10587259808045351

[185] D. Guérard and R. Janot, “Structure of the superdense LiC3 compound prepared by ball-milling,” *Journal of Physics and Chemistry of Solids*, vol. 65, no. 2-3, pp. 147–152, Mar. 2004. [Online]. Available: https://doi.org/10.1016/j.jpcs.2003.09.027

[186] R. Setton and J. Conard, “Madelung energy and stability of the compound $\mathrm{li}_7\mathrm{c}_{24}$prepared under pressure,” *Molecular Crystals and Liquid Crystals Science and Technology. Section A. Molecular Crystals and Liquid Crystals*, vol. 244, no. 1, pp. 307–312, Apr. 1994. [Online]. Available: https://doi.org/10.1080/10587259408050122

[187] V. Mordkovich, “Synthesis and XPS investigation of superdense lithium-graphite intercalation compound, LiC2,” *Synthetic Metals*, vol. 80, no. 3, pp. 243–247, Jul. 1996. [Online]. Available: https://doi.org/10.1016/0379-6779(96)80209-8

[188] R. Janot and D. Guerard, “Ball-milling in liquid mediaApplications to the preparation of anodic materials for lithium-ion batteries,” *Progress in Materials Science*, vol. 50, no. 1, pp. 1–92, Jan. 2005. [Online]. Available: https://doi.org/10.1016/s0079-6425(03)00050-1

[189] C. Burmeister, L. Titscher, S. Breitung-Faes, and A. Kwade, “Dry grinding in planetary ball mills: Evaluation of a stressing model,” *Advanced Powder Technology*, vol. 29, no. 1, pp. 191–201, Jan. 2018. [Online]. Available: https://doi.org/10.1016/j.apt.2017.11.001

[190] V. A. Nalimova, “High pressure for synthesis and study of superdense alkali metal - carbon compounds,” *Molecular Crystals and Liquid Crystals Science and Technology. Section A. Molecular Crystals and Liquid Crystals*, vol. 310, no. 1, pp. 5–18, Feb. 1998. [Online]. Available: https://doi.org/10.1080/10587259808045308

[191] J. Conard and P. Lauginie, “Lithium NMR in lithium-carbon solid state compounds,” *TANSO*, vol. 2000, no. 191, pp. 62–70, 2000. [Online]. Available: https://doi.org/10.7209/tanso.2000.62

[192] S. E. Hayes, R. A. Guidotti, W. R. Even, P. J. Hughes, and H. Eckert, “7li solid-state nuclear magnetic resonance as a probe of lithium species in microporous carbon anodes,” *The Journal of Physical Chemistry A*, vol. 107, no. 19, pp. 3866–3876, May 2003. [Online]. Available: https://doi.org/10.1021/jp021772f

[193] R. Tossici, R. Janot, F. Nobili, D. Guèrard, and R. Marassi, “Electrochemical behavior of superdense ‘LiC2’ prepared by ball-milling,” *Electrochimica Acta*, vol. 48, no. 10, pp. 1419–1424, Apr. 2003. [Online]. Available: https://doi.org/10.1016/s0013-4686(03)00019-7

[194] P. Azaïs, L. Duclaux, A.-M. Faugère, and F. Béguin, “Reactive milling of graphite with lithium: Application to lithium batteries,” *Applied Physics Letters*, vol. 81, no. 4, pp. 775–777, Jul. 2002. [Online]. Available: https://doi.org/10.1063/1.1493236

[195] T. M. Paronyan, A. K. Thapa, A. Sherehiy, J. B. Jasinski, and J. S. D. Jangam, “Incommensurate graphene foam as a high capacity lithium intercalation anode,” *Scientific Reports*, vol. 7, no. 1, pp. 2045–2322, Jan. 2017. [Online]. Available: https://doi.org/10.1038/srep39944

[196] V. V. Avdeev, V. A. Nalimova, and K. N. Semenenko, “The alkali metals in graphite matrixes-new aspects of metallic state chemistry,” *High Pressure Research*, vol. 6, no. 1, pp. 11–25, Oct. 1990. [Online]. Available: https://doi.org/10.1080/08957959008203195

[197] Y. F. Reynier, R. Yazami, and B. Fultz, “Thermodynamics of lithium intercalation into graphites and disordered carbons,” *Journal of The Electrochemical Society*, vol. 151, no. 3, pp. A422–A426, 2004. [Online]. Available: https://doi.org/10.1149/1.1646152

[198] Y. Reynier, R. Yazami, and B. Fultz, “XRD evidence of macroscopic composition inhomogeneities in the graphite–lithium electrode,” *Journal of Power Sources*, vol. 165, no. 2, pp. 616–619, Mar. 2007. [Online]. Available: https://doi.org/10.1016/j.jpowsour.2006.10.023

[199] M. Drüe, M. Seyring, A. Kozlov, X. Song, R. Schmid-Fetzer, and M. Rettenmayr, “Thermodynamic stability of li2c2 and LiC6,” *Journal of Alloys and Compounds*, vol. 575, pp. 403–407, Oct. 2013. [Online]. Available: https://doi.org/10.1016/j.jallcom.2013.06.001

[200] Y. Imai and A. Watanabe, “Energetic evaluation of possible stacking structures of li-intercalation in graphite using a first-principle pseudopotential calculation,” *Journal of Alloys and Compounds*, vol. 439, no. 1-2, pp. 258–267, Jul. 2007. [Online]. Available: https://doi.org/10.1016/j.jallcom.2006.08.061

[201] Z. Wang, S. M. Selbach, and T. Grande, “Van der waals density functional study of the energetics of alkali metal intercalation in graphite,” *RSC Adv.*, vol. 4, no. 8, pp. 3973–3983, 2014. [Online]. Available: https://doi.org/10.1039/c3ra47187j

[202] D. C.-H. H. B.-C. J. B.-S. G. Hal-Bon, “Structures and formation energies of lixc6 (x=1-3) and its homologues for lithium rechargeable batteries,” *Bulletin of the Korean Chemical Society,*, vol. 32, no. 6, pp. 2045–2050, 2011. [Online]. Available: http://dx.doi.org/10.5012/bkcs.2011.32.6.2045

[203] G. Kresse and J. Hafner, “Ab initiomolecular dynamics for liquid metals,” *Physical Review B*, vol. 47, no. 1, pp. 558–561, Jan. 1993. [Online]. Available: https://doi.org/10.1103/physrevb.47.558

[204] G. Kresse and D. Joubert, “From ultrasoft pseudopotentials to the projector augmented-wave method,” *Physical Review B*, vol. 59, no. 3, pp. 1758–1775, Jan. 1999. [Online]. Available: https://doi.org/10.1103/physrevb.59.1758

[205] A. Togo and I. Tanaka, “First principles phonon calculations in materials science,” *Scripta Materialia*, vol. 108, pp. 1–5, Nov. 2015. [Online]. Available: https://doi.org/10.1016/j.scriptamat.2015.07.021

[206] M. Chase, *NIST-JANAF Thermochemical Tables, 4th Edition*. American Institute of Physics, -1, 1998-08-01 1998.

[207] B. Hourahine, B. Aradi, V. Blum, F. Bonafé, A. Buccheri, C. Camacho, C. Cevallos, M. Y. Deshaye, T. Dumitrică, A. Dominguez, S. Ehlert, M. Elstner, T. van der Heide, J. Hermann, S. Irle, J. J. Kranz, C. Köhler, T. Kowalczyk, T. Kubař, I. S. Lee, V. Lutsker, R. J. Maurer, S. K. Min, I. Mitchell, C. Negre, T. A. Niehaus, A. M. N. Niklasson, A. J. Page, A. Pecchia, G. Penazzi, M. P. Persson, J. Řezáč, C. G. Sánchez, M. Sternberg, M. Stöhr, F. Stuckenberg, A. Tkatchenko, V. W. z. Yu, and T. Frauenheim, "DFTB+, a software package for efficient approximate density functional theory based atomistic simulations," *The Journal of Chemical Physics*, vol. 152, no. 12, p. 124101, Mar. 2020. [Online]. Available: https://doi.org/10.1063/1.5143190

[208] D. J. Evans and B. L. Holian, "The nose–hoover thermostat," *The Journal of Chemical Physics*, vol. 83, no. 8, pp. 4069–4074, Oct. 1985. [Online]. Available: https://doi.org/10.1063/1.449071

[209] P. Lauginie, H. Estrade-Szwarckopf, and J. Conard, "^{6}li, ^{7}li and ^{8}li-NMR shifts and relaxation rates in LiC$_6$: Evidence of quadrupolar interaction with conduction electrons," *Materials Science Forum*, vol. 91-93, pp. 545–550, Jan. 1992. [Online]. Available: https://doi.org/10.4028/www.scientific.net/msf.91-93.545

[210] H. J. Chang, A. J. Ilott, N. M. Trease, M. Mohammadi, A. Jerschow, and C. P. Grey, "Correlating microstructural lithium metal growth with electrolyte salt depletion in lithium batteries using 7li MRI," *Journal of the American Chemical Society*, vol. 137, no. 48, pp. 15 209–15 216, Nov. 2015. [Online]. Available: https://doi.org/10.1021/jacs.5b09385

[211] N. M. Trease, L. Zhou, H. J. Chang, B. Y. Zhu, and C. P. Grey, "In situ NMR of lithium ion batteries: Bulk susceptibility effects and practical considerations," *Solid State Nuclear Magnetic Resonance*, vol. 42, pp. 62–70, Apr. 2012. [Online]. Available: https://doi.org/10.1016/j.ssnmr.2012.01.004

[212] J. Rogal and K. Reuter, *Ab Initio Atomistic Thermodynamics for Surfaces: A Primer*, ser. AD-a476 575. Defense Technical Information Center, 2006. [Online]. Available: https://books.google.de/books?id=TAy0AQAACAAJ

[213] J. Winter, *Magnetic resonance in metals*. Clarendon Press Oxford, 1971.

[214] J. Wandt, P. Jakes, J. Granwehr, R. A. Eichel, and H. A. Gasteiger, "Quantitative and time-resolved detection of lithium plating on graphite anodes in lithium ion batteries," *Materials Today*, vol. 21, no. 3, pp. 231–240, APR 2018.

[215] C. Sole, N. E. Drewett, and L. J. Hardwick, "Insitu raman study of lithium-ion intercalation into microcrystalline graphite," *Faraday Discuss.*, vol. 172, pp. 223–237, 2014. [Online]. Available: https://doi.org/10.1039/c4fd00079j

[216] R. Bhattacharyya, B. Key, H. Chen, A. S. Best, A. F. Hollenkamp, and C. P. Grey, "In situ NMR observation of the formation of metallic lithium microstructures in lithium batteries," *Nature Materials*, vol. 9, no. 6, pp. 504–510, May 2010. [Online]. Available: https://doi.org/10.1038/nmat2764

[217] G. Roth, K. Lüders, P. Pfluger, and H.-J. Güntherodt, "7li and 133cs NMR parameters in c6li and c8cs intercalated oriented graphites," *Solid State Communications*, vol. 39, no. 3, pp. 423–426, Jul. 1981. [Online]. Available: https://doi.org/10.1016/0038-1098(81)90632-3

[218] J. Garcés, "A probabilistic description of the configurational entropy of mixing," *Entropy*, vol. 16, no. 5, pp. 2850–2868, May 2014. [Online]. Available: https://doi.org/10.3390/e16052850

[219] N. van Kampen, *Stochastic Processes in Physics and Chemistry*. Elsevier, 2007. [Online]. Available: https://doi.org/10.1016/b978-0-444-52965-7.x5000-4

[220] L. Günter and M. Penrose, “Poisson and other discrete distributions,” in *Lectures on the Poisson Process*. Cambridge University Press, 2017, pp. 1–8. [Online]. Available: https://doi.org/10.1017/9781316104477.002

[221] T. J. Frankcombe and S. C. Smith, “Numerical solution methods for large, difficult kinetic master equations,” *Theoretical Chemistry Accounts*, vol. 124, pp. 303–317, 2009.

[222] A. Jansen, “Dynamic monte-carlo simulations of reactions in heterogeneous catalysis,” *Catalysis Today*, vol. 53, no. 2, pp. 259–271, Oct. 1999. [Online]. Available: https://doi.org/10.1016/s0920-5861(99)00120-0

[223] S. Longo, “Monte carlo simulation of charged species kinetics in weakly ionized gases,” *Plasma Sources Science and Technology*, vol. 15, no. 4, pp. S181–S188, Oct. 2006. [Online]. Available: https://doi.org/10.1088/0963-0252/15/4/s04

[224] I. Martin-Bragado, R. Borges, J. P. Balbuena, and M. Jaraiz, “Kinetic monte carlo simulation for semiconductor processing: A review,” *Progress in Materials Science*, vol. 92, pp. 1–32, Mar. 2018. [Online]. Available: https://doi.org/10.1016/j.pmatsci.2017.09.003

[225] R. A. Marcus, “Theoretical relations among rate constants, barriers, and broensted slopes of chemical reactions,” *The Journal of Physical Chemistry*, vol. 72, no. 3, pp. 891–899, Mar. 1968. [Online]. Available: https://doi.org/10.1021/j100849a019

[226] M. G. Evans and M. Polanyi, “Some applications of the transition state method to the calculation of reaction velocities, especially in solution,” *Transactions of the Faraday Society*, vol. 31, p. 875, 1935. [Online]. Available: https://doi.org/10.1039/tf9353100875

[227] P. P. Ewald, “Die berechnung optischer und elektrostatischer gitterpotentiale,” *Annalen der Physik*, vol. 369, no. 3, pp. 253–287, 1921. [Online]. Available: https://doi.org/10.1002/andp.19213690304

[228] H. Li and J.-L. Brédas, “Kinetic monte carlo modeling of charge carriers in organic electronic devices: Suppression of the self-interaction error,” *The Journal of Physical Chemistry Letters*, vol. 8, no. 11, pp. 2507–2512, May 2017. [Online]. Available: https://doi.org/10.1021/acs.jpclett.7b01161

[229] J. Pelleg, “Diffusion in NiAl,” in *Diffusion in the Iron Group L12 and B2 Intermetallic Compounds*. Springer International Publishing, 2017, pp. 237–282. [Online]. Available: https://doi.org/10.1007/978-3-319-39522-7_8

[230] A. Singer, Z. Schuss, and R. S. Eisenberg, “Attenuation of the electric potential and field in disordered systems,” *Journal of Statistical Physics*, vol. 119, no. 5-6, pp. 1397–1418, Mar. 2005. [Online]. Available: https://doi.org/10.1007/s10955-005-3025-1

[231] S. Frank, S. Divinski, U. Södervall, and C. Herzig, “Ni tracer diffusion in the b2-compound NiAl: influence of temperature and composition,” *Acta Materialia*, vol. 49, no. 8, pp. 1399–1411, May 2001. [Online]. Available: https://doi.org/10.1016/s1359-6454(01)00037-4

[232] M. Park, X. Zhang, M. Chung, G. B. Less, and A. M. Sastry, “A review of conduction phenomena in li-ion batteries,” *Journal of Power Sources*, vol. 195, no. 24, pp. 7904–7929, Dec. 2010. [Online]. Available: https://doi.org/10.1016/j.jpowsour.2010.06.060

[233] A. J. Bard and L. R. Faulkner, “Electrochemical methods: Fundamentals and applications,” in *Electrochemical Methods*. Wiley 2nd Edition, 2008.

[234] R. Bessler, U. Duerig, and E. Koren, “The dielectric constant of a bilayer graphene interface,” *Nanoscale Advances*, vol. 1, no. 5, pp. 1702–1706, 2019. [Online]. Available: https://doi.org/10.1039/c8na00350e

[235] D. Chung and X. Xi, “Factors that govern the electric permittivity of carbon materials in the graphite allotrope family,” *Carbon*, vol. 184, pp. 245–252, Oct. 2021. [Online]. Available: https://doi.org/10.1016/j.carbon.2021.08.016

List of publications

1. Revisiting the storage capacity limit of graphite battery anodes: spontaneous lithium overintercalation at ambient pressure

Cristina Grosu, Chiara Panosetti, Steffen Merz, Peter Jakes, Sebastian Matera Rüdiger-A. Eichel, Josef Granwehr, and Christoph Scheurer (submitted, 2022)

2. Investigating diffusion of lithium intercalated in graphite by a combination of charged kinetic Monte Carlo and spin-alignment echo nuclear magnetic resonance

Cristina Grosu, Sandra Döpking, Steffen Merz, Peter Jakes, Chiara Panosetti, Rüdiger-A. Eichel, Christoph Scheurer, Josef Granwehr, and Sebastian Matera (in preparation)

3. DFTB Modeling of Lithium-Intercalated Graphite with Machine-Learned Repulsive Potential

Chiara Panosetti, Simon B. Anniés, **Cristina Grosu**, Stefan Seidlmayer, and Christoph Scheurer

J. Phys. Chem. A, 2021, 125, 2, 691–699

Contribution: This work is partially discussed in this thesis within the framework of the multiscale modeling Lithium-intercalated graphite.

4. Mobile Small Polarons Qualitatively Explain Conductivity in Lithium Titanium Oxide Battery Electrode

Matthias Kick, **Cristina Grosu**, Markus Schuderer, Christoph Scheurer, and Harald Oberhofer

J. Phys. Chem. Lett., 2020, 11, 7, 2535–2540

Contributions: The idea for this project came from Cristina Grosu and Matthias Kick. Matthias Kick was responsible for carrying out the theoretical simulations. Discussion and interpretation of the results was achieved in close collaboration between Cristina Grosu and Matthias Kick. Christoph Scheurer and Harald Oberhofer helped editing the Manuscript. This work is not discussed in this thesis, but was performed during the doctoral research period.

5. On the Origin of Reversible and Irreversible Reactions in $LiNi_xCo_{(1-x)/2}Mn_{(1-x)/2}O_2$

Karin Kleiner, Claire A. Murray, **Cristina Grosu**, Bixian Ying, Martin Winter, Peter Nagel, Stefan Schuppler and Michael Merz

J. Electrochem. Soc., 2021, 168(12), 120533

This work is not discussed in this thesis, but was published during this period.

Acknowledgments / Danksagung

During this journey, there were and are too many people to thank you. First of all, I would like to thank Dr. Chistoph Scheurer and Prof. Josef Granwehr for giving me the chance of playing "random" between theory and experiments and for their patience, being always last minute. On the same line Prof. Rüdiger Eichel and Prof. Karsten Reuter for giving me the opportunity to perform my PhD thesis in their groups. Following, not in terms of priority or importance I will include here Dr.Sebastian Matera, Dr. Chiara Panosetti, Dr. Matthias Kick, Dr. Peter Jakes, Dr. Steffen Merz, Dr. Simone Köcher, Dr. Sandra Döpking.

I am sure I will forget someone if I start writing the names, but from the IT admins, I will just recall again Matthias and David, followed by the first level support. A lot of the people became friends during this journey within the group or not, and definitely will never thank anyone enough in words, those the reason to keep in short here, whereas everyone will get or got already my personal "Thank you". Ruth, deserve a special thank you that made the bureaucracy much easier and not only.